Radboud University Nijmegen

Radboud University

Faculty of Science (FNWI)

Close Limit Approximation for boosted black holes

Analysing gravitational waves at the horizon and far away

Thesis MSc Physics and Astronomy

Author:
Pjotr Koster

Supervisors:
Dr. Béatrice Bonga
Prof. Dr. Badri Krishnan

August 14, 2025

Contents

1 Introduction

General Relativity is the most successful theory of gravitation to date. It describes gravity as the curvature of space-time, as opposed to being a local force [1]. Some of its early predictions are the perihelion precession of Mercury's orbit, the deflection of light by the sun and the gravitational redshift of light [2]. It passed these tests already in the early to mid 20th century [3–5]. Besides these "classical tests" of General Relativity, new experiments have been suggested to test General Relativity in other regions, such as the small scale or in the strong field regime. Examples include researching the gravitational potential at small distances, investigating whether a test particle's orbit around a rotating mass shows small secular precession and inspecting whether Newton's gravitational constant remains constant in all of spacetime [6–11].

The strong field tests form a subset of tests of General Relativity that concerns itself with contexts where the gravitational fields are the strongest. In these contexts, like regions near black holes or binary pulsars, gravitational fields can not be properly approximated using corrections to Newtonian gravity. Examples of strong field tests are the direct observation of a black hole by the Event Horizon Telescope and the detection of gravitation waves [12, 13]. The detection of the Hulse-Taylor binary pulsar in 1974 provided the first experimental evidence of gravitational waves [14]. The orbital decay of this neutron star-pulsar binary showed a loss in energy, which was similar to the predicted energy loss via gravitational radiation [15, 16]. However, it took a while for gravitational waves to be detected directly. The first detection of gravitational waves was in 2015 and the result was published in 2016 by the Laser Interferometer Gravitational-Wave Observatory (LIGO) [17]. Observing gravitational waves is still an active field of research and there are new projects discussed currently, like the Einstein Telescope in Europe and the launching of the Laser Interferometer Space Antenna (LISA) [18–20].

Gravitational waves are temporary disturbances in a gravitational field, manifesting as small ripples in space-time, caused by events such as the movement of massive objects like merging black holes. They carry energy and angular momentum away from the system [21, 22]. A prominent source of gravitational waves are binary systems, such as two neutron starts orbiting each other or two black holes merging [23, 24]. However, supernovae events and early universe formation shortly after the Big Bang also created gravitational waves [25, 26]. Gravitational waves do not interact strongly with matter, since it only interacts with their comparatively small gravitational fields [22]. On the other hand, electromagnetic radiation's path and energy is heavily influenced when it passes through, for example, a gas cloud [27, 28]. This makes it possible for us to analyse objects which are normally not detectable via electromagnetic radiation, such as far away objects or the early universe [29].

A prominent source for gravitational waves is the merging of black holes, which consists of an inspiral, merger and ringdown phase [30, 31]. During the inspiral phase, the two black holes are orbiting each other while they keep getting closer. The merger phase is the stage when the two black holes are in the process of becoming one black hole. The black hole that forms during the merger phase needs to stabilize, which happens during the ringdown phase via a decrease in the asymmetry of the black hole. During all phases, gravitational waves are generated in the neighbourhood of the black holes. Part of the gravitational waves are absorbed by the black hole, and another part is sent out to infinity. As Figure 1 shows, the signal is the strongest during the merger phase [17]. During the ringdown phase, one gets tones that are characteristic of the final black hole and the signal is given by a superposition of dampened oscillations. These modes of the oscillations, which give us information about the final black hole, are called Quasi-Normal Modes (QNMs) [32–34].

1.1 Perturbation theory of black holes

The metric $g_{\mu\nu}$ plays an important role in General Relativity, since it contains the information about the curvature of space-time [35]. The Einstein Field Equations, which are equations describing the curvature of

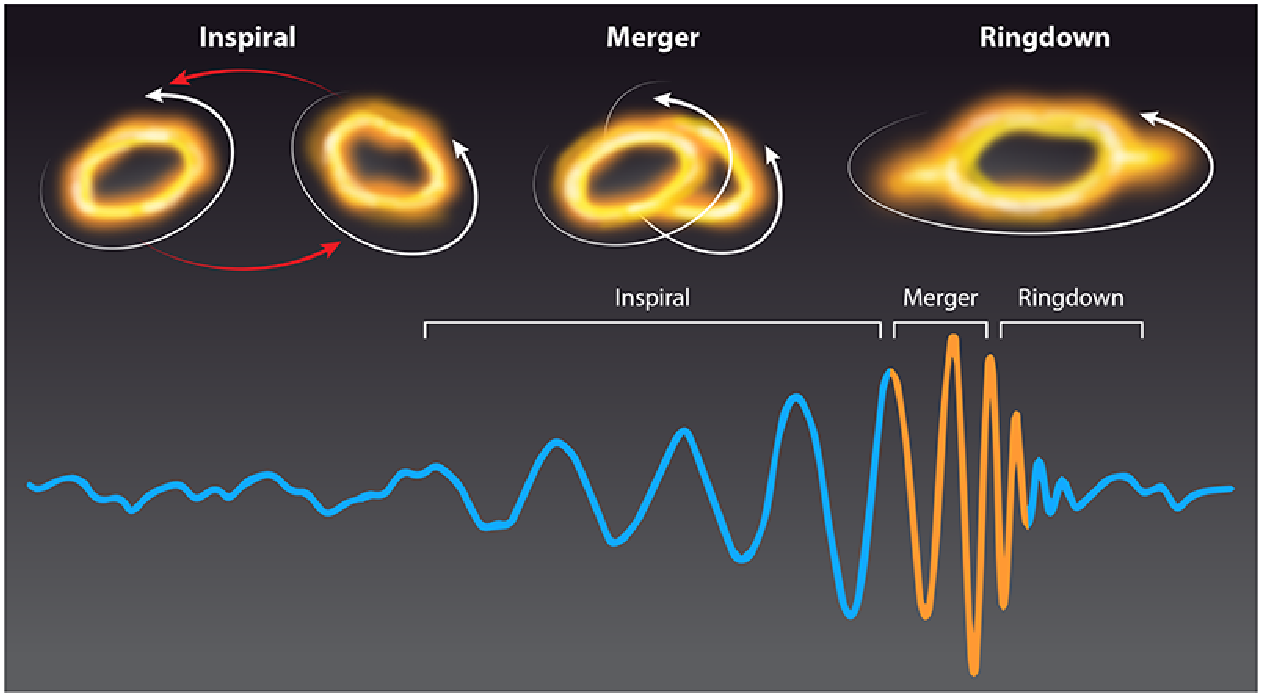

Figure 1: At the top, you can see a depiction of the three phases of a black holes merger. At the bottom, one can see their respective gravitational wave data. The data from the inspiral has an increasing amplitude and frequency. The peak is reached during the merger phase, which is shorter than the inspiral phase. Afterwards, there is a ringdown phase, during which the final black hole comes to an equilibrium. Picture from [17].

space-time as a consequence of matter and energy, therefore contains terms like the Ricci Curvature tensor $R_{\mu\nu}$, which are defined using the metric [2]. A cornerstone of describing gravitational waves is perturbation theory, which applies a small perturbation to the metric, which lead to perturbation terms in for example the Ricci Curvature tensor. These perturbation terms satisfy their own Einstein Field Equations, called the linearized Einstein Field Equations [34].

In the following, we will explain the linearized Einstein Field Equations in more detail. In perturbation theory for black holes, the metric is given by

$$g_{\mu\nu} = {}^{(0)}g_{\mu\nu} + \epsilon\, {}^{(1)}g_{\mu\nu} + \mathcal{O}(\epsilon^2), \tag{1}$$

where ${}^{(0)}g_{\mu\nu}$ is the background metric (such as the Schwarzschild metric), ϵ is a small expansion parameter and ${}^{(1)}g_{\mu\nu}$ the first-order metric perturbation. Using the metric, it is possible to construct the Christoffel symbol, defined by

$$\Gamma^{\rho}_{\mu\nu} = \frac{1}{2} g^{\rho\sigma} \left(\partial_\mu g_{\sigma\nu} + \partial_\nu g_{\sigma\mu} - \partial_\sigma g_{\mu\nu}\right). \tag{2}$$

The expansion of the metric allows for an expansion of the Christoffel symbol. The first order term of the Christoffel symbol $\Gamma^{\rho}_{\mu\nu}$ is

$${}^{(1)}\Gamma^{\rho}{}_{\mu\nu} = \frac{1}{2}\, {}^{(0)}g^{\rho\sigma} \left(\partial_\mu\, {}^{(1)}g_{\sigma\nu} + \partial_\nu\, {}^{(1)}g_{\sigma\mu} - \partial_\sigma\, {}^{(1)}g_{\mu\nu}\right) - \frac{1}{2}\, {}^{(1)}g^{\rho\sigma} \left(\partial_\mu\, {}^{(0)}g_{\sigma\nu} + \partial_\nu\, {}^{(0)}g_{\sigma\mu} - \partial_\sigma\, {}^{(0)}g_{\mu\nu}\right) \tag{3}$$

Since the Christoffel symbol $\Gamma^{\rho}_{\mu\nu}$ is used to define the Riemann curvature tensor $R^{\rho}_{\sigma\mu\nu}$, there is a first order term ${}^{(1)}R^{\rho}{}_{\sigma\mu\nu}$. Through this process, it is also possible to express the Ricci Curvature tensor $R_{\mu\nu}$ and Ricci scalar R perturbatively.
The curvature of space-time is described by the Einstein Field Equations, which is denoted by

$$G_{\mu\nu} + \Lambda g_{\mu\nu} = \kappa T_{\mu\nu}, \tag{4}$$

where Λ is the cosmological constant (which we assume to be zero), $T_{\mu\nu}$ is the stress-energy tensor (which we take to be zero in each component, meaning we consider vacuum solutions) and $G_{\mu\nu}$ is the Einstein Tensor defined by

$$G_{\mu\nu} = R_{\mu\nu} - \frac{1}{2} R g_{\mu\nu}. \tag{5}$$

In equation (5), we have the Ricci Curvature tensor $R_{\mu\nu}$ and Ricci scalar R, which we can define for different orders of perturbation theory, for example $R_{\mu\nu} = {}^{(0)}R_{\mu\nu} + \epsilon\, {}^{(1)}R_{\mu\nu} + \mathcal{O}(\epsilon^2)$. Consequently, we can define the Einstein Tensor perturbatively,

$$G_{\mu\nu} = {}^{(0)}G_{\mu\nu} + \epsilon\, {}^{(1)}G_{\mu\nu} + \mathcal{O}(\epsilon^2), \tag{6}$$

where ${}^{(0)}G_{\mu\nu}$ satisfies the Einstein Equation and ${}^{(1)}G_{\mu\nu}$ satisfies the linearized Einstein Equation

$${}^{(1)}G_{\mu\nu} + \Lambda\, {}^{(1)}g_{\mu\nu} = \kappa\, {}^{(1)}T_{\mu\nu}\,. \tag{7}$$

The Einstein field Equations (4) are a complex set of non-linear equations. The linearized Einstein Field Equations (7) makes the problem more tractable, creating linear equations. The equation becomes more difficult at higher orders, due to the mixing of terms from different orders, making the equations and terms non-linear. To solve equation (7), people have resorted to numerical methods or approximate methods.
Numerical Relativity is very successful at modelling gravitational wave systems [36–38]. There are various different numerical models which describe the inspiral, merger and ringdown phase of two body coalescence. These numerical methods are the most accurate method for constructing waveforms to date and are the benchmark for approximate schemes [39]. However, these numerical method models function a bit like a black box: one sets up the initial data and evolves is using the Einstein Field Equations via code, which does not explain how aspects of the binary system interact and evolve. To get more insight about what happens during a coalescence, we therefore will analyse the problem using approximate methods.
Currently, we have approximate methods for the inspiral phase and ringdown phase. For the inspiral phase, there exist post-Newtonian or post-Minkowskian expansions. The post-Newtonian approximation expands the metric tensor in powers of velocity v/c, with v being much smaller than the speed of light, and the gravitational constant G/c^2 [40, 41]. The post-Minkowskian approximations only expands the metric in the gravitational constant without assuming the velocity is small. The background metric considered in these models is the metric for flat spacetime: the Minkowski metric [42, 43]. For the ringdown phase, the system is described as a perturbed black hole, meaning the background metric is for example the Schwarzschild black hole [44].
The merger phase is hard to analytically describe since there are strong gravitational fields, which means that we expect the full nonlinear aspect of General Relativity to kick in. Consequently, numerical methods are usually used to solve the Einstein equations for this phase of the two body coalescence [45]. Solving the complete wave-form for the two body coalescence therefore requires a combination of approximate methods and numerical solutions. An example of such a scheme is the effective one-body formalism [46, 47]. However, the approximate methods from both the inspiral and ringdown phase have been surprisingly successful to predict signals from what would normally be considered the merger phase [48–50]. This suggests that it would be useful to analyse the early ringdown phase or late inspiral phase, since it would allow us to analyse the merger phase. In this thesis, we will analyse the ringdown phase by using the Close Limit Approximation.

1.2 The Close Limit Approximation

The Close Limit Approximation was proposed by Price and Pullin in 1994 to model the merger phase [51]. The model assumes that two black holes are close enough to each other, such that the separation of the two black holes can be used as an expansion parameter. The black holes are close enough for an apparent horizon to form which encompasses the two black holes and the black holes can be approximated as being one perturbed black hole. The approximation method was necessary due to Numerical Relativity models being constrained by the technology at the time.

Early work focused on the non-rotating or slowly rotating black holes, which merged to become a perturbed Schwarzschild black hole [52–54]. The perturbation theory was first done up to first order and later up to second order [55–58]. Second order perturbation theory was used to verify first-order results and determine the limits of validity of the method. Due to the development of Numerical relativity models, there was a stagnation of work publish on the Close Limit Approximation after the 2000s [59–61].

So far, most analysis of gravitational waves has been regarding QNMs from data far away from the horizon. However, given the mathematical description of QNMs, they can also be found in data from near the horizon. Currently, there is not much research on data extracted from the horizon [62]. It would be of interest to investigate whether similar data can be obtained at the horizon, taking into account the delay. Potential detection of a redshift in the data or difference in the quasi-normal modes could tell us more about the development of the Zerilli function. The purpose of this thesis is to fill in this current gap in research by analysing gravitational waves near the horizon.

In this thesis, we will expand on the work by Nicasio *et al.* [57] by analysing near the horizon and far away, the gravitational waves from the merger of two equal-mass m Schwarzschild black holes with equal momentum P towards each other. We deviate from [57] in both the results and formalism used, by considering the gauge invariant Zerilli function. This thesis also sets the ground for analysing the gravitational waves up to second order by calculating the initial data up to second order.

1.3 Overview of this thesis

This thesis is therefore split into three parts: calculating initial data, evolving the initial data, analysing the results. For a flowchart of this thesis see Figure 2.

Firstly, we need to calculate the initial data for the Zerilli wave function. The Zerilli wave function is expressed in terms that are derived from perturbations of the space-time metric $g_{\mu\nu}$. To ease the calculation, we use the $3+1$ split of spacetime. Calculating the four dimensional space-time metric is now reduced to calculating the perturbations of the extrinsic curvature K_{ab} and the three dimensional spatial metric γ_{ab} of the $t=0$ slice. Calculating these tensors requires us to calculate the conformal factor ϕ. For these calculations we will use perturbation theory in the distance L and momentum P up to second order. These calculations are done in Section 2

Afterwards, we will cast the data in the perturbation formalism by Regge and Wheeler by expanding the spatial metric γ_{ab} and the extrinsic curvature K_{ab} in Legendre Polynomials P^l_m. The coefficients will be calculated up to first order in Section 3, while the calculations for second order can be found in Appendix B.

In Section 4, we will use the calculations of the coefficients to get the initial data for the gauge invariant Zerilli function ψ, its time derivative $\partial_t\psi$ and radial derivative $\partial_r\psi$ at $t=0$.

To get the Zerilli wave function at later times, we need to evolve the initial data using the Zerilli equation. In Section 5, we introduce the mathematical framework behind Partial Differential Equations (PDEs). In Section 6, we will explain the code that numerically evolves the inital data. The foundations of the code are set up by Stamatis Vretinaris and are expanded on by Pjotr Koster. The code uses the method of lines and method of characteristics to reduce the Zerilli function (a PDE) to three ODEs. This set of ODEs is subsequently solved via the fourth order Runge Kutta method using a Julia script.

In Section 7, the robustness and convergence of the code is discussed. We will first set out the theoretical framework for testing the solver and then discuss different toy problems that have been solved using the code.
In Section 8, we will discuss the results from evolving the initial data. We show that the data is highly dependent on the resolution of the data and shows a lack of numerical convergence for the solution. We hypothesize that the problem lies with the initial data, since previous tests of convergence have come up positive. Potential solutions and further extensions of this thesis are discussed in Section 9.

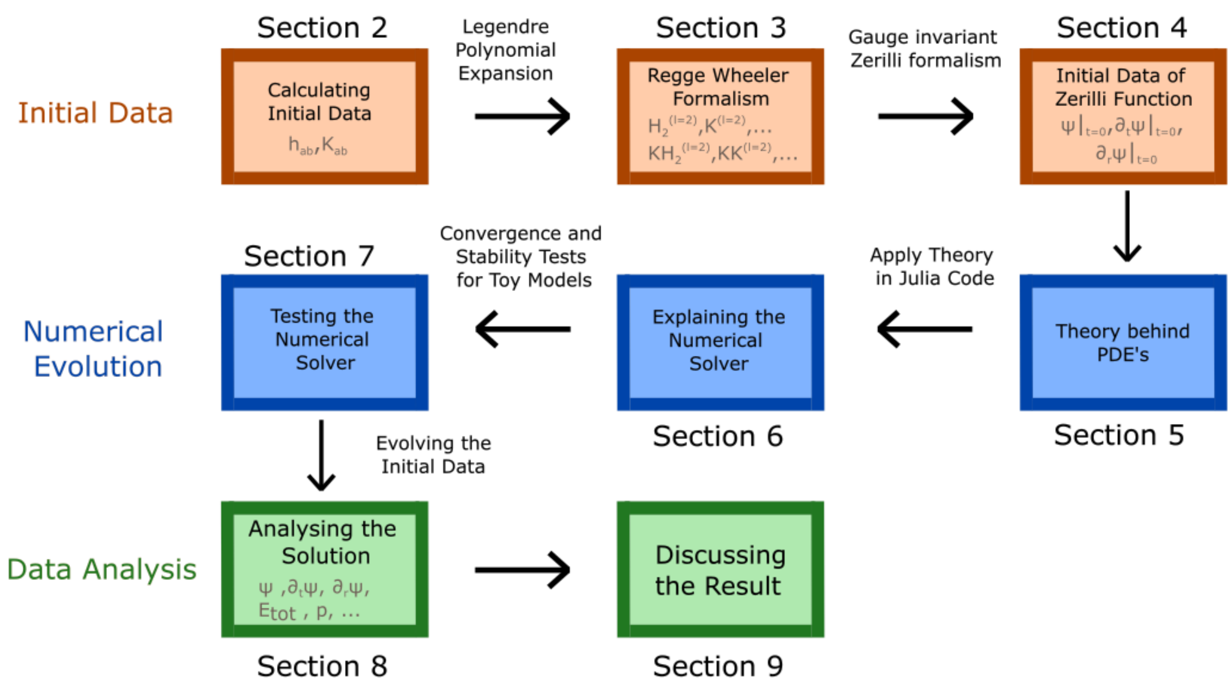

Figure 2: Flowchart showing the breakdown of this thesis. The calculations of the initial data are done in Sections 2-4 and this is part is colourcoded orange in the flowchart. The quantities calculated are denoted in grey. The numerical evolution of the initial data is the second part of the thesis which is done in Sections 5-7. This part is colourcoded blue in the flowchart. The last part of this thesis analyses the numerical solution, which is done in Sections 8-9 and is colourcoded green in the flowchart.

In this thesis, a grasp on the basics of General Relativity and Riemannian Manifolds is assumed. However, some details on the ADM-formalism can be found in the Appendix A and concepts behind gravitational waves in Appendix C.
We conclude with some notational remarks. The Greek indices $(\mu, \nu, \rho, \sigma, \ldots)$ denote objects in four-dimensional space-time, whereas Latin indices $(a, b, c, d, \ldots)$ denote objects on the three-dimensional spatial hypersurface. The perturbative order of a term will be denoted by a superscript in front of the symbol, in order to avoid notational clutter with the indices. We will use natural units, meaning we set $G = c = \hbar = 1$.

2 Initial data

The first step in setting up the close limit approximation is constructing the initial data. This requires specifying a spatial 3-metric γ_{ab} and extrinsic curvature K_{ab} on some spatial hypersurface Σ_t, such that the constraint equations of General Relativity are satisfied (see Appendix A).
We will use the conformal approach (see [63]), so we introduce a conformal transformation ϕ, such that

$$\gamma_{ab} = \phi^4 \hat{\gamma}_{ab}, \tag{8}$$

which relates the spatial metric to some conformally related background metric $\hat{\gamma}_{ab}$. The extrinsic curvature K_{ab} will also be split into is trace K and a trace-free part

$$K_{ab} = \phi^{-2} \hat{A}_{ab} + \frac{1}{3}\gamma_{ab} K, \tag{9}$$

where $\hat{A}_{ab}$ is the conformally rescaled trace-free part of the extrinsic curvature.

2.1 Extrinsic curvature to second order

From casting General Relativity into a Hamiltonian description, we get constraint equations and evolution equations. In the context of two boosted black holes, these constraint equations relate the extrinsic curvature to the "momentum" P, background metric $\hat{\gamma}_{ab}$ and the coordinate "distance" between the centres of the black hole L.[1] We will assume that P and L are small and of the same order ϵ.[2] This allows us to construct the extrinsic curvature tensor $\hat{K}_{ab}$, which we will do up to second order in ϵ^2.[3] After getting an expression for the extrinsic curvature, we can use the remaining constraint equation to relate the conformal factor to the extrinsic curvature, meaning we can calculate the conformal factor up to second order.

2.1.1 Extrinsic curvature and the constraint equations

The constraint equations are given by

$$8\hat{\nabla}^2\phi - \phi\hat{R} - \frac{2}{3}\phi^5 K^2 + \phi^{-7}\hat{A}_{ab}\hat{A}^{ab} = 0; \tag{10}$$

$$\hat{D}_b\hat{A}^{ab} - \frac{2}{3}\phi^6\hat{\gamma}^{ab}\hat{D}_b K = 0, \tag{11}$$

where $\hat{\nabla}^2 = \hat{\gamma}^{ab}\hat{D}_a\hat{D}_b$ is the Laplacian, $\hat{D}_a$ is the covariant derivative and $\hat{R}$ the Ricci scalar associated to the conformal background metric $\hat{\gamma}_{ab}$. Equation (10) is called the Hamiltonian constraint and equation (11) is known as the momentum constraint. Note that $\hat{\gamma}_{ab}$ and K are freely specifiable.
For our calculations, we assume that our original metric γ_{ab} is conformally flat, in the sense that $\hat{\gamma}_{ab} = \hat{f}_{ab}$ where $\hat{f}_{ab}$ is the Euclidean 3-metric. Furthermore, we take a maximal slicing such that $K = 0$. This simplifies the constraint equations (10) and (11) to

$$\hat{\nabla}^2\phi = -\frac{1}{8}\phi^{-7}\hat{A}_{ab}\hat{A}^{ab}; \tag{12}$$

[1] There are quotation marks around "momentum" and "length", since, for example, L is not the proper length, but proportional to it. Our expansion parameter are sufficient, as the focus of this thesis is to show the behaviour of gravitational waves at the horizon and far away and not to get specific numeric results.

[2] Note that P and L are not dimensionless, so technically one should divide by some constant to make them dimensionless. However, since we are using natural units and look at the general behaviour, such details are omitted.

[3] i.e. up to order L^4, P^4, P^2L^2, L^3P and P^3L.

$$\hat{D}_b \hat{A}^{ab} = 0. \tag{13}$$

The momentum constraint (13) has become linear and is decoupled from the Hamiltonian constraint (12). Besides, the Hamiltonian constraint has now become a simple Poisson equation. Therefore, we can formulate initial data by first solving equation (13) for $\hat{A}_{ab}$ and then the Poisson equation in (12) to determine the conformal factor ϕ.
In our case, the solution for a single boosted black hole with centre at coordinate $\mathbf{C}$ and a momentum $\mathbf{P}$ is given by the Bowen-York solution [64]. The conformally rescaled trace-free part of the extrinsic curvature is then given by

$$\hat{A}^{\mathbf{CP}}_{ab} = \frac{3}{2r^2_{\mathbf{C}}} \left[2P_{(a}n_{b)} - (\hat{\gamma}_{ab} - n_a n_b) P^c n_c \right], \tag{14}$$

where $r_{\mathbf{C}} = \|x^i - C^i\|$ is the coordinate distance between the centre of the black hole $\mathbf{C}$ and an arbitrary point $\mathbf{x}$, with respect to the flat metric $\hat{f}_{ab}$. This solution describes a single "boosted" black hole. Since the momentum constraint equation (13) is linear, the superposition of two solutions is still a solution to the constraint equation. Hence, the extrinsic curvature $\hat{K}_{ab}$ in the context of two black holes at positions $\mathbf{C}_1$ and $\mathbf{C}_2$ with momenta $\mathbf{P}_1$ and $\mathbf{P}_2$, is given by

$$\hat{K}_{ab} = \hat{A}^{\mathbf{C}_1\mathbf{P}_1}_{ab} + \hat{A}^{\mathbf{C}_2\mathbf{P}_2}_{ab}. \tag{15}$$

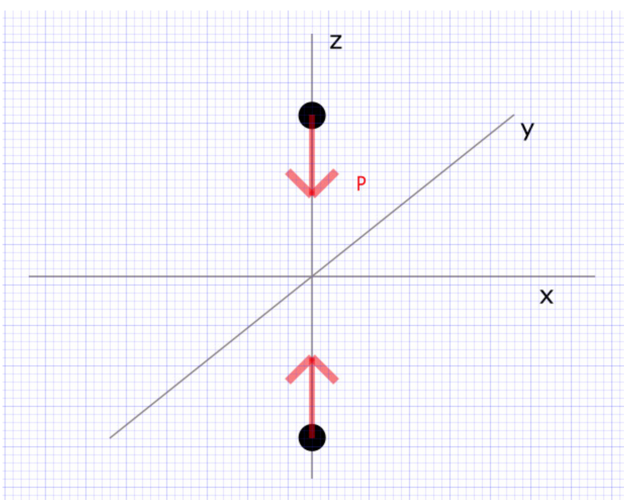

Figure 3: Two equal mass non-spinning black holes on the z axis at equal distance from the origin, with momenta in the direction of each other. The momenta have magnitude P.

2.1.2 Calculation of extrinsic curvature in flat space-time

To calculate the extrinsic curvature in flat space-time, we will use a coordinate system in which the two black holes are positioned on the z axis at $\pm L/2$ as depicted in Figure 3. The two black holes have a momentum of equal magnitude P but opposite direction.
We are interested in the close limit of small initial separation L, which is why we use L as our order parameter. Furthermore, we assume that P is also small and is related to L via $P = \eta L$, where η is some numerical value of order one. Hence, terms containing a factor PL^2, P^2L or L^3 are all of the same order.
Consider equation (15). In our coordinate system, the total extrinsic curvature $\hat{K}^{\text{total}}_{ab}$ is represented in the

basis $\hat{x} = (R, \theta, \phi)$, where R is the coordinate distance to the origin, with respect to $\hat{\gamma}_{ab}$. This implies that $R = \sqrt{x^2 + y^2 + z^2}$. However, each single extrinsic curvature $\hat{A}_{ab}^{\mathbf{C}_1\mathbf{P}_1}$ is expressed in the basis (r_i, θ_i, ϕ), where r_i is the coordinate distance to the centre of the black hole i, see Figure 5. Therefore, in this next part, will describe the Bowen-York solution (14) in coordinates $\hat{x}$.

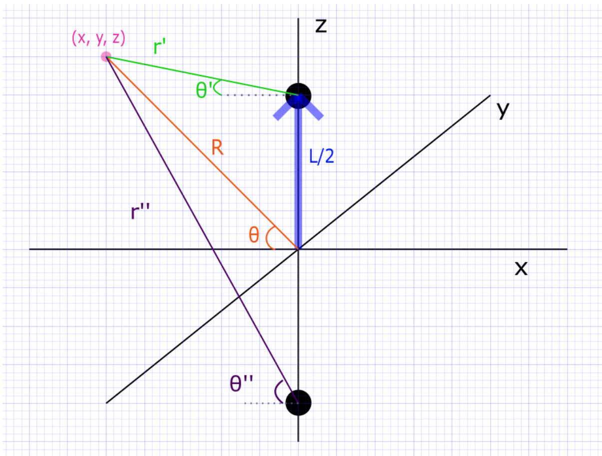

Figure 4: Sketch of the two black holes on a grid with x, y, z axes. The black holes are placed at $\pm L/2$ on the z axis. In pink, a random coordinate is shown at (x, y, z), or equivalently at (R, θ, ϕ). The r', θ' in the figure are the same as the r_1, θ_1 in the text above. The same holds for r'', θ'' and r_2, θ_2

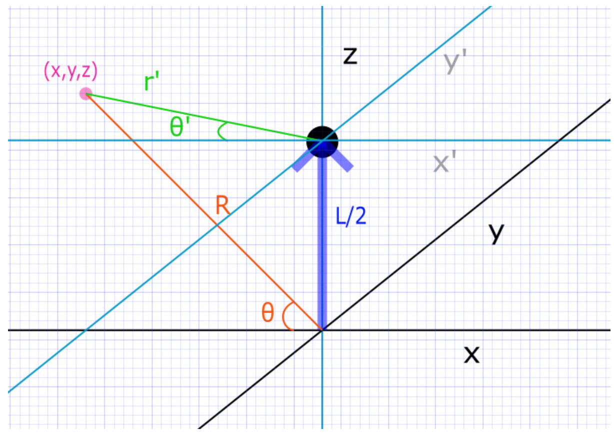

Figure 5: Diagram showing the change of basis. The light blue axes denote the new coordinate system. The axes in black are the same one as in the previous figure, except the z axis. The z axis in the new coordinate system is the same as the one before, which is why it is in blue.

Consider the black hole located at $(x, y, z) = (0, 0, -L/2)$, as seen in Figure 4. Alternatively, we can use a radial coordinate system, which means that the black hole in this coordinate system is at $(R, \theta, \phi) = (L/2, \pi, 0)$. If we perform a coordinate change that shifts the z-coordinate up by $L/2$, the black hole is located in the new coordinate system at $(x', y', z') = (0, 0, 0)$. If we use the radial coordinate system with the origin centred at this new origin, we have that the black hole is located at $(r_1, \theta_1, \phi_1) = (0, 0, 0)$. Using basic geometry and definition of spherical coordinates, we find

$$\begin{aligned} r_1 &= \sqrt{x'^2 + y'^2 + z'^2} = \sqrt{x^2 + y^2 + (z - L/2)^2} \\ &= \sqrt{R^2 + L^2/4 - RL\cos(\theta)} \end{aligned} \tag{16}$$

$$\cos(\theta_1) = \frac{z'}{r_1} = \frac{R\cos(\theta) - L/2}{r_1} \tag{17}$$

$$\phi_1 = \mathrm{sgn}(y') \frac{x'}{\sqrt{x'^2 + y'^2}} = \phi \tag{18}$$

Having defined the coordinates, we can define the relevant vectors in the (r_1, θ_1, ϕ) basis

$$\mathbf{n}_1 = dr_1 = \frac{2R - L\cos(\theta)}{2r_1} dR + \frac{RL\sin(\theta)}{2r_1} d\theta \tag{19}$$

$$\mathbf{P}_1 = -|P|dz' = -Pdz = -|P|\left[\cos(\theta)dR - R\sin(\theta)d\theta\right], \tag{20}$$

where we used that $dz = dz'$. The proof for this claim is

$$\begin{aligned}
dz' &= d(r_1\cos(\theta_1)) = \cos(\theta_1)dr_1 + r_1 d\cos(\theta_1)\\
&= \frac{R\cos(\theta) - L/2}{\sqrt{R^2 + L^2/4 - RL\cos(\theta)}}\left[\left(\frac{2R - L\cos(\theta)}{2\sqrt{\frac{L^2}{4} - LR\cos(\theta) + R^2}}\right)dR + \left(\frac{LR\sin(\theta)}{2\sqrt{\frac{L^2}{4} - LR\cos(\theta) + R^2}}\right)d\theta\right]\\
&+ \sqrt{R^2 + L^2/4 - RL\cos(\theta)}\left[\left(\frac{\cos(\theta)}{\sqrt{\frac{L^2}{4} - LR\cos(\theta) + R^2}} - \frac{(2R - L\cos(\theta))\left(R\cos(\theta) - \frac{L}{2}\right)}{2\left(\frac{L^2}{4} - LR\cos(\theta) + R^2\right)^{3/2}}\right)dR\right.\\
&+ \left.\left(-\frac{LR\sin(\theta)\left(R\cos(\theta) - \frac{L}{2}\right)}{2\left(\frac{L^2}{4} - LR\cos(\theta) + R^2\right)^{3/2}} - \frac{R\sin(\theta)}{\sqrt{\frac{L^2}{4} - LR\cos(\theta) + R^2}}\right)d\theta\right]\\
&= \left[\cos(\theta) - \frac{(2R - L\cos(\theta))\left(R\cos(\theta) - \frac{L}{2}\right)}{2\left(\frac{L^2}{4} - LR\cos(\theta) + R^2\right)} + \frac{(R\cos(\theta) - L/2)(2R - L\cos(\theta))}{2\left(\frac{L^2}{4} - LR\cos(\theta) + R^2\right)}\right]dR\\
&+ \left[\frac{LR\sin(\theta)\left(R\cos(\theta) - \frac{L}{2}\right)}{2\left(\frac{L^2}{4} - LR\cos(\theta) + R^2\right)} - \frac{LR\sin(\theta)\left(R\cos(\theta) - \frac{L}{2}\right)}{2\left(\frac{L^2}{4} - LR\cos(\theta) + R^2\right)} - R\sin(\theta)\right]d\theta\\
&= \cos(\theta)dR - R\sin(\theta)d\theta = dz.
\end{aligned} \tag{21}$$

Now we can create the relevant tensors in the (R, θ, ϕ) basis, namely

$$\begin{aligned}
2P_{(a}n_{b)} &= \frac{-|P|}{r_1}\begin{pmatrix} 2\cos(\theta)\left[R - \frac{L}{2}\cos(\theta)\right] & \frac{L}{2}R\cos(\theta)\sin(\theta) - R\sin(\theta)\left[R - \frac{L}{2}\cos(\theta)\right] & 0\\ \text{Sym} & -LR^2\sin(\theta)^2 & 0\\ 0 & 0 & 0\end{pmatrix}\\
&= \frac{-|P|}{r_1}\begin{pmatrix} 2\cos(\theta)\left[R - \frac{L}{2}\cos(\theta)\right] & R\sin(\theta)\left[\frac{L}{2}\cos(\theta) - R\right] & 0\\ \text{Sym} & -LR^2\sin(\theta)^2 & 0\\ 0 & 0 & 0\end{pmatrix},
\end{aligned} \tag{22}$$

$$n_a n_b = \frac{1}{r_1^2}\begin{pmatrix} \left[R - \frac{L}{2}\cos(\theta)\right]^2 & \frac{L}{2}R\sin(\theta)\left[R - \frac{L}{2}\cos(\theta)\right] & 0\\ \text{Sym} & \frac{L^2}{4}R^2\sin(\theta)^2 & 0\\ 0 & 0 & 0\end{pmatrix}, \tag{23}$$

$$\hat{\gamma}_{ab} = \begin{pmatrix} 1 & 0 & 0\\ 0 & R^2 & 0\\ 0 & 0 & R^2\sin(\theta)^2\end{pmatrix}. \tag{24}$$

Lastly, we get

$$P_{1c}n_1{}^c = \frac{-|P|}{r_1}\left[\cos(\theta)\left(R - \frac{L}{2}\cos(\theta)\right) - \frac{L}{2}\frac{R^2}{R^2}\sin(\theta)^2\right] = \frac{-|P|}{r_1}\left[R\cos(\theta) - L/2\right]. \tag{25}$$

In these equations we have still used r_1, to create an expression that is more insightful. However, it is easy to express r_1 in terms of R and θ by using equation (16).

With these choices, we obtain for equation (14) in (R,θ,ϕ) basis

$$
\hat{A}_{ab}^{\mathbf{C}_1\mathbf{P}_1} = \frac{3|P|}{2r_1^3}\begin{pmatrix} \frac{L\left(3\cos(2\theta)\left(L^2+8R^2\right)+L^2-5LR\cos(3\theta)+24R^2\right)-R\cos(\theta)\left(19L^2+32R^2\right)}{4(L^2-4LR\cos(\theta)+4R^2)} & Symm & 0 \\ \frac{R\sin(\theta)\left(-3L^3\cos(\theta)+5L^2R\cos(2\theta)+9L^2R-20LR^2\cos(\theta)+8R^3\right)}{2(L^2-4LR\cos(\theta)+4R^2)} & 0 & 0 \\ 0 & 0 & 0 \end{pmatrix} + \frac{3|P|}{2r_1^3}
$$
$$
\begin{pmatrix} 0 & 0 & 0 \\ 0 & \frac{R^3\cos(\theta)\left(7L^2+16R^2\right)-\cos(2\theta)\left(3L^3+16LR^3\right)+L^3R+5L^2R^2\cos(3\theta)-8LR^3}{4(L^2-4LR\cos(\theta)+4R^2)} & 0 \\ 0 & 0 & R^2\sin(\theta)^2(R\cos(\theta)-L/2) \end{pmatrix} \tag{26}
$$

We get something similar for $\hat{A}_{ab}^{\mathbf{C}_2\mathbf{P}_2}$. Doing a Taylor expansion in L (note that r_i has an L dependence) around $L=0$ up to fifth order,[4] gives us

$$
\begin{aligned}
\hat{K}_{ab}^{\text{tot}} &= \begin{pmatrix} -\frac{L(6P)\cos(\theta)^2}{R^3} & 0 & 0 \\ 0 & \frac{L(3P)(\cos(2\theta)+3)}{4R} & 0 \\ 0 & 0 & \frac{L\sin(\theta)^2((3P)(3\cos(2\theta)+1))}{4R} \end{pmatrix} \\
&+ \begin{pmatrix} -\frac{L^3(3P)(28\cos(2\theta)+25\cos(4\theta)+11)}{64R^5} & -\frac{L^3\sin(2\theta)((3P)(5\cos(2\theta)+3))}{16R^4} & 0 \\ \text{Sym} & \frac{L^3(3P)(36\cos(2\theta)+15\cos(4\theta)+13)}{128R^3} & 0 \\ 0 & 0 & 0 \end{pmatrix} \\
&+ \begin{pmatrix} 0 & 0 & 0 \\ 0 & 0 & 0 \\ 0 & 0 & \frac{3L^3P\sin(\theta)^2(20\cos(2\theta)+35\cos(4\theta)+9)}{128R^3} \end{pmatrix} + O\left(L^5\right) \\
&= \frac{3PL}{2R^3}\begin{pmatrix} -4\cos(\theta)^2 & 0 & 0 \\ 0 & \frac{R^2(-1+2\cos(\theta)^2+3)}{2} & 0 \\ 0 & 0 & \frac{R^2\sin(\theta)^2}{2}[3(-1+2\cos(\theta)^2)+1] \end{pmatrix} + \frac{3PL^3}{16R^5} \\
&\quad \begin{pmatrix} -\frac{28}{4}[-1+2\cos(\theta)^2] - \frac{25}{4}[1-8\cos(\theta)^2+8\cos(\theta)^4] + \frac{11}{4} & 0 & 0 \\ -2R\sin(\theta)\cos(\theta)\left[5[-1+2\cos(\theta)^2]+3\right] & 0 & 0 \\ 0 & 0 & 0 \end{pmatrix} \\
&+ \frac{3PL^3}{16R^5}\begin{pmatrix} 0 & -2R\sin(\theta)\cos(\theta)\left[5[-1+2\cos(\theta)^2]+3\right] & 0 \\ 0 & \frac{36R^2}{8}[-1+2\cos(\theta)^2] + \frac{15R^2}{8}[1-8\cos(\theta)^2+8\cos(\theta)^4] + \frac{13R^2}{8} & 0 \\ 0 & 0 & 0 \end{pmatrix} + O\left(L^5\right) \\
&+ \frac{3PL^3}{16R^5}\begin{pmatrix} 0 & 0 & 0 \\ 0 & 0 & 0 \\ 0 & 0 & \frac{R^2}{8}\left[1-\cos(\theta)^2\right]\left[20[-1+2\cos(\theta)^2]+35[1-8\cos(\theta)^2+8\cos(\theta)^4]+9\right] \end{pmatrix} + O\left(L^5\right)
\end{aligned}
$$

[4] This only affects the $\hat{K}_{\phi\phi}^{\text{tot}}$ entry, but not the other entries.

$$
\begin{aligned}
&= \frac{3PL}{2R^3}\begin{pmatrix} -4\cos(\theta)^2 & 0 & 0 \\ 0 & R^2\left[\cos(\theta)^2+1\right] & 0 \\ 0 & 0 & R^2\sin(\theta)^2[3\cos(\theta)^2-1] \end{pmatrix} + \frac{3PL^3}{16R^5} \\
&\begin{pmatrix} -\frac{1}{4}\left[8-144\cos(\theta)^2+200\cos(\theta)^4\right] & -2R\sin(\theta)\cos(\theta)\left[-2+10\cos(\theta)^2\right] & 0 \\ \text{Sym} & \frac{R^2}{8}\left[-8-48\cos(\theta)^2+120\cos(\theta)^4\right] & 0 \\ 0 & 0 & 0 \end{pmatrix}, \\
&+ \frac{3PL^3}{16R^5}\begin{pmatrix} 0 & 0 & 0 \\ 0 & 0 & 0 \\ 0 & 0 & \frac{R^2}{8}\left[24-(240+24)\cos(\theta)^2+(280+240)\cos(\theta)^4-280\cos(\theta)^6\right] \end{pmatrix} + O\left(L^5\right) \\
&= \frac{3PL}{2R^3}\begin{pmatrix} -4\cos(\theta)^2 & 0 & 0 \\ 0 & R^2\left[\cos(\theta)^2+1\right] & 0 \\ 0 & 0 & R^2\sin(\theta)^2[3\cos(\theta)^2-1] \end{pmatrix} + \frac{3PL^3}{16R^5} \\
&\begin{pmatrix} -2+36\cos(\theta)^2-50\cos(\theta)^4 & -4R\sin(\theta)\cos(\theta)\left[-1+5\cos(\theta)^2\right] & 0 \\ \text{Sym} & R^2\left[-1-6\cos(\theta)^2+15\cos(\theta)^4\right] & 0 \\ 0 & 0 & R^2\left[3-33\cos(\theta)^2+65\cos(\theta)^4-35\cos(\theta)^6\right] \end{pmatrix},
\end{aligned}
\tag{27}
$$

where we call the $PL \backsim L^2$ term the first order term and $PL^3 \backsim L^4$ the second order term of the extrinsic curvature. Note that the end result for equation (27) is the same as the solution given by [57], except for a minus factor in front of the whole L^3 contribution. The equation above also agrees with the solution Tom van der Steen obtained using Mathematica [65].

2.2 Determining the Conformal Factor

Now that we have expanded $\hat{K}_{ab}$ up to second order, the next step is to determine the conformal factor ϕ by solving the Hamiltonian constraint. In this thesis, we assume that the black holes are of equal mass $m_1 = m_2 = M_{\mathrm{ADM}}/2$, where M_{ADM} is the ADM mass.[5]
In the context of two *stationary* black holes of equal mass, where the extrinsic curvature vanishes, one already has a solution for the conformal factor ϕ_{BL}. This solution was given by Brill and Lindquist [66]

$$
\phi_{\mathrm{BL}} \equiv 1 + \frac{m_1}{2\|\mathbf{R}-\mathbf{R}_1\|} + \frac{m_2}{2\|\mathbf{R}-\mathbf{R}_2\|}, \tag{28}
$$

where $\|\ldots\|$ indicates the coordinate distance with respect to $\hat{f}_{ab}$. From now on, we will set $m_1 = m_2 = m$. Note that ϕ_{BL} is singular at the two points $\mathbf{R} = \mathbf{R}_{1,2}$ and by construction $\hat{\nabla}^2\phi_{\mathrm{BL}} = 0$.
Since we are working with *boosted* black holes, we add a regularising term ϕ_{reg}, such that the conformal factor is given by

$$
\phi = \phi_{\mathrm{reg}} + \phi_{\mathrm{BL}}. \tag{29}
$$

From equation (12), we see that finding the conformal factor ϕ means that we have to solve

$$
\hat{\nabla}^2\phi_{\mathrm{reg}} = -\frac{1}{8}\frac{\hat{K}_{ab}\hat{K}^{ab}}{(\phi_{\mathrm{BL}}+\phi_{\mathrm{reg}})^7} \tag{30}
$$

[5]The definition of m_1 and the relation to M_{ADM} is a bit more subtle than described here. For more context and nuance see [57].

with the boundary conditions that ϕ_{reg} is regular at $\mathbf{R} = \mathbf{R}_{1,2}$ and approaches zero at infinity. We will solve (30) perturbatively for ϕ_{reg} up to second order in L.
Since we are only working to second order for ϕ, we only need to use the term in the extrinsic curvature linear in L in equation (27). Using the fact that the extrinsic curvature at first order and inverse metric are diagonal, we get

$$\begin{aligned}
\hat{K}_{ab}\hat{K}^{ab} &= \hat{K}_{ab}\hat{\gamma}^{ac}\hat{\gamma}^{bd}\hat{K}_{cd} \\
&= \left(\frac{3PL}{2R^3}\right)^2 \left[\left(-4\cos(\theta)^2\right)^2 + \left(\frac{1}{R^2}\right)^2 R^4\left[\cos(\theta)^2+1\right]^2 + \left(\frac{1}{R^2\sin(\theta)^2}\right)^2 R^4\sin(\theta)^4\left[3\cos(\theta)^2-1\right]^2\right] \\
&= \left(\frac{9P^2L^2}{4R^6}\right)^2 \left[16\cos(\theta)^4 + \cos(\theta)^4 + 2\cos(\theta)^2 + 9\cos(\theta)^4 - 6\cos(\theta)^2 + 1\right] \\
&= \frac{117L^2P^2\cos(\theta)^4}{2R^6} - \frac{9L^2P^2\cos^2(\theta)}{R^6} + \frac{9L^2P^2}{2R^6} + O\left(L^3\right) \\
&= \frac{9L^2P^2}{2R^6}\left[1 - 2\cos(\theta)^2 + 13\cos(\theta)^2\right] + O\left(L^3\right).
\end{aligned} \tag{31}$$

Hence, the ansatz for the regularising term is given by

$$\phi_{\text{reg}} = P^2L^{2\,(2)}\phi + O\left(L^3\right) \tag{32}$$

Furthermore, for computational simplicity we make the approximation

$$\phi \approx \phi_{\text{BL}} \approx \frac{2R+M}{2R} = 1 + \frac{M}{2R}, \tag{33}$$

which follows from expanding equation (28) using Legendre polynomials (see Appendix D for details). Combining equations (31) and (33), we find that ${}^{(2)}\phi$ should satisfy the following partial differential equation

$$P^2L^2\hat{\nabla}^{2\,(2)}\phi = -72P^2L^2\frac{R(1-2\cos^2\theta+13\cos^4\theta)}{(2R+M)^7} \equiv {}^{(2)}S, \tag{34}$$

where we impose the boundary conditions that ${}^{(2)}\phi \to 0$ as $R \to \infty$.

2.2.1 Expansion in Legendre polynomials

We simplify the Poisson equation (34) by expanding both the source term ${}^{(2)}S$ and the conformal factor ${}^{(2)}\phi$ in multipoles using Legendre polynomials. The source term takes the form

$${}^{(2)}S = \sum_{l=0}^{\infty} {}^{(2)}S^{(l)}P_l\left[\cos(\theta)\right]. \tag{35}$$

To determine the factors ${}^{(2)}S^{(l)}$ in the multipole expansion (35) is equivalent to solving the following system of equations

$${}^{(2)}S^{(l=0)} - \frac{1}{2}{}^{(2)}S^{(l=2)} + \frac{3}{8}{}^{(2)}S^{(l=4)} = -\frac{72P^2L^2R}{(2R+M)^7}, \tag{36}$$

$$\frac{3}{2}\,{}^{(2)}S^{(l=2)} - \frac{30}{8}\,{}^{(2)}S^{(l=4)} = -\frac{144P^2L^2R}{(2R+M)^7}, \tag{37}$$

$$\frac{35}{8}\,{}^{(2)}S^{(l=4)} = \frac{936P^2L^2R}{(2R+M)^7}. \tag{38}$$

The solution to this system of equations is

$$ {}^{(2)}S^{(l=0)} = -\frac{1056}{5}\frac{P^2L^2R}{(2R+M)^7}, \tag{39a}$$

$$ {}^{(2)}S^{(l=2)} = -\frac{3072}{7}\frac{P^2L^2R}{(2R+M)^7}, \tag{39b}$$

$$ {}^{(2)}S^{(l=4)} = -\frac{7488}{35}\frac{P^2L^2R}{(2R+M)^7}. \tag{39c}$$

The term ${}^{(2)}\phi$ can also be expanded in multipoles as

$$ {}^{(2)}\phi = {}^{(2)}\phi^{(l=0)}P_0\left[\cos(\theta)\right] + {}^{(2)}\phi^{(l=2)}P_2\left[\cos(\theta)\right] + {}^{(2)}\phi^{(l=4)}P_4\left[\cos(\theta)\right]. \tag{40}$$

We can solve equation (30) by solving for each multipole separately, since the Legendre polynomials are eigenfunctions of the Laplacian (see Appendix D). Hence, for each l the following equation must be satisfied

$$P^2L^2\hat{\nabla}^2\left({}^{(2)}\phi^{(l)}P_l\left[\cos(\theta)\right]\right) = {}^{(2)}S^{(l)}P_l\left[\cos(\theta)\right]. \tag{41}$$

Writing out the Laplacian for the flat background metric $\hat{f}_{ab}$ in spherical coordinates (R,θ,φ), we get

$$\begin{aligned} \frac{P_l\left[\cos(\theta)\right]}{R}\frac{\partial}{\partial R}\left(R^2\frac{\partial {}^{(2)}\phi^{(l)}}{\partial R}\right) + \frac{{}^{(2)}\phi^{(l)}}{R^2\sin\theta}\frac{\partial}{\partial\theta}\left(\sin\theta\frac{\partial P_l\left[\cos(\theta)\right]}{\partial\theta}\right) \\ + \frac{{}^{(2)}\phi^{(l)}}{R^2\sin^2\theta}\frac{\partial^2 P_l\left[\cos(\theta)\right]}{\partial\varphi^2} = \frac{{}^{(2)}S^{(l)}P_l\left[\cos(\theta)\right]}{P^2L^2}. \end{aligned} \tag{42}$$

Multiplying this equation by ${}^{(2)}\phi^{(l)}P_l\left[\cos(\theta)\right]$ and dividing it by R^2, we obtain

$$\frac{1}{{}^{(2)}\phi^{(l)}}\frac{\partial}{\partial R}\left(R^2\frac{\partial {}^{(2)}\phi^{(l)}}{\partial R}\right) + \underbrace{\frac{1}{P_l\sin\theta}\frac{\partial}{\partial\theta}\left(\sin\theta\frac{\partial P_l}{\partial\theta}\right) + \frac{1}{P_l\sin^2\theta}\frac{\partial^2 P_l}{\partial\varphi^2}}_{-l(l+1)} = R^2\frac{{}^{(2)}S^{(l)}}{P^2L^2\,{}^{(2)}\phi^{(l)}}. \tag{43}$$

Here, we use the fact that the angular part of the Laplace equation equals $-l(l+1)$. Therefore, the radial part results in a Riedel Equation for each multipole

$$\frac{\partial}{\partial R}\left(R^2\frac{\partial {}^{(2)}\phi^{(l=0)}}{\partial R}\right) = -\frac{1056}{5}\frac{R^3}{(2R+M)^7}, \tag{44a}$$

$$\frac{\partial}{\partial R}\left(R^2\frac{\partial {}^{(2)}\phi^{(l=2)}}{\partial R}\right) - 6\,{}^{(2)}\phi^{(l=2)} = -\frac{3072}{7}\frac{R^3}{(2R+M)^7}, \tag{44b}$$

$$\frac{\partial}{\partial R}\left(R^2\frac{\partial {}^{(2)}\phi^{(l=4)}}{\partial R}\right) - 20\,{}^{(2)}\phi^{(l=4)} = -\frac{7488}{35}\frac{R^3}{(2R+M)^7}. \tag{44c}$$

These ordinary differential equations were solved using Mathematica and the results are

$$\phi^{(2)(l=0)} = -\frac{11}{50}\frac{(8RM + 20R^2 + M^2)}{(2R+M)^5 R} \;+\; \frac{q_0}{R}, \tag{45a}$$

$$\phi^{(2)(l=2)} = -\frac{8}{35}\frac{(M^4 + 10M^3R + 40M^2R^2 + 80MR^3 + 80R^4)}{(2R+M)^5 R^3} \;+\; \frac{q_2}{R^3}. \tag{45b}$$

Note that the boundary condition that ϕ_{reg} should approach zero as $R \to \infty$ is satisfied by both solutions (45a) and (45b). The constants q_0 and q_2 are homogenous solutions to equation (30), which implies that their value is determined by the boundary condition on ϕ_{reg}. In this context, the condition is that ϕ_{reg} needs to be regular for $R < L$. Their values, as determined in [57], are

$$q_0 = \frac{0.219}{M^3}, \tag{46a}$$

$$q_2 = \frac{0.224}{M}. \tag{46b}$$

We therefore have up to $l = 2$ and up to first order in P and L

$$\begin{aligned}\phi_{\text{reg}} = P^2L^2\Bigg[&P_0\left[\cos(\theta)\right]\left(-\frac{11}{50}\frac{(8RM + 20R^2 + M^2)}{(2R+M)^5 R} \;+\; \frac{0.219}{M^3R}\right) + P_2\left[\cos(\theta)\right]\\ &\left(-\frac{8}{35}\frac{(M^4 + 10M^3R + 40M^2R^2 + 80MR^3 + 80R^4)}{(2R+M)^5R^3} \;+\; \frac{0.224}{MR^3}\right)\Bigg] + O\left(L^3\right).\end{aligned} \tag{47}$$

3 Polynomial expansions

Having calculated the initial data for γ_{ab} and K_{ab}, we will express the perturbations using the Regge-Wheeler notation.
In this thesis, we are considering a Schwarzschild background, which is static and spherically symmetric. This means we can separate the spherical components (θ, ϕ) from the (t, r) components using tensorial spherical harmonics. Using the spherical symmetry of our system, we can ignore the ϕ component and use a sum of Legendre Polynomials of the form $P_\ell\left[\cos(\theta)\right]$ to describe the system. This notation means we disregard the factor $\sqrt{(2l-1)/4\pi}$ from $Y^{lm}(\theta, \phi)$ [67].
The perturbations can be categorized in two kinds: even and odd parity perturbations. Under parity transformations on the two sphere, even parity modes change with the sign $(-1)^l$, while odd parity modes transform with the sign $(-1)^{l+1}$. In this section, we will discuss only even parity perturbations, since our system is symmetric under parity transformation.

3.1 Schwarzschild metric perturbations

Consider the four dimensional Schwarzschild metric. The perturbations of the metric can be descibed using the notation introduced by Regge and Wheeler[67]

$$g_{tt} = \left(1 - \frac{2M}{r}\right) \sum_\ell H_0^{(\ell)}(r,t) P_\ell\left[\cos(\theta)\right] \tag{48a}$$

$$g_{tr} = \sum_\ell H_1^{(\ell)}(r,t) P_\ell\left[\cos(\theta)\right] \tag{48b}$$

$$g_{t\theta} = \sum_\ell h_0^{(\ell)}(r,t)(\partial/\partial\theta) P_\ell\left[\cos(\theta)\right] \tag{48c}$$

$$g_{r\theta} = \sum_\ell h_1^{(\ell)}(r,t)(\partial/\partial\theta) P_\ell\left[\cos(\theta)\right] \tag{48d}$$

$$g_{rr} = (1 - 2M/r)^{-1} \sum_\ell H_2^{(\ell)}(r,t) P_\ell\left[\cos(\theta)\right] \tag{48e}$$

$$g_{\theta\theta} = r^2 \sum_\ell \left[K^{(\ell)}(r,t) + G^{(\ell)}(r,t)(\partial^2/\partial\theta^2)\right] P_\ell\left[\cos(\theta)\right] \tag{48f}$$

$$g_{\phi\phi} = r^2 \sin^2\theta \sum_\ell \left[K^{(\ell)}(r,t) + G^{(\ell)}(r,t)\cot\theta(\partial/\partial\theta)\right] P_\ell\left[\cos(\theta)\right]. \tag{48g}$$

Since we are working with the ADM formalism, we will work the spatial metric γ_{ab}, meaning that we only consider equations (48d) - (48g) in this Section.
The spatial metric is given by

$$\hat{\gamma}_{ab} = \phi^4 \hat{f}_{ab}, \tag{49}$$

where the hat signals that the metric is in flat space-time and

$$\hat{f}_{ab} = \begin{pmatrix} 1 & 0 & 0 \\ 0 & R^2 & 0 \\ 0 & 0 & R^2\sin(\theta)^2 \end{pmatrix}, \tag{50}$$

in the (R, θ, ϕ) basis, where R is the isotropic radial coordinate of a Schwarzschild spacetime [68].
Note however that the metric in equation (48) is expressed using the usual Schwarzschild radius r as a basis.

These two radial coordinates are related by

$$R = \frac{(\sqrt{r} + \sqrt{r-2M})^2}{4} \Longleftrightarrow r = \frac{(R + \frac{M}{2})^2}{R}, \tag{51}$$

which implies that

$$\frac{dR}{dr} = \frac{R}{r} \frac{1}{\sqrt{1 - \frac{2M}{r}}}. \tag{52}$$

This means that we can express the spatial metric in Schwarzschild coordinates as

$$\gamma_{ab} = \frac{\partial \hat{x}^i}{\partial x^a} \frac{\partial \hat{x}^j}{\partial x^b} \hat{\gamma}_{ij} = \frac{R^2}{r^2} \phi^4 \begin{pmatrix} \frac{1}{1-\frac{2M}{r}} & 0 & 0 \\ 0 & r^2 & 0 \\ 0 & 0 & r^2 \sin(\theta)^2 \end{pmatrix}. \tag{53}$$

3.1.1 Expanding the conformal factor

Calculating ϕ^4 completely by hand is cumbersome. Thererfore, we will use the fact that the Legendre Polynomials form an orthogonal basis, such that dealing with the cross-terms from the expression becomes less cumbersome.
In Section 2.2.1, we expanded ϕ_{reg} into Legendre Polynomials. We therefore only need to do the same for the Brill Lindquist conformal factor. Using the definition of the Legendre Polynomials (see Appendix D), we get

$$\begin{aligned} \phi_{\text{BL}} &= 1 + \frac{m}{2\|\mathbf{R} - \mathbf{R}_1\|} + \frac{m}{2\|\mathbf{R} - \mathbf{R}_2\|} \\ &= 1 + \frac{m}{2\sqrt{R^2 + L^2/4 + RL\cos(\theta)}} + \frac{m}{2\sqrt{R^2 + L^2/4 - RL\cos(\theta)}} \\ &= \left(1 + \frac{M}{2R}\right) P_0[\cos(\theta)] + \frac{ML^2}{8R^3} P_2[\cos(\theta)] + \frac{ML^4}{32R^5} P_4[\cos(\theta)] + O(L^6). \end{aligned} \tag{54}$$

Looking at Appendix D, it is clear that we get a pre-factor $m/R = M/2R$ and $u = \pm\frac{L}{2R}$. The latter explains why there is no Legendre Polynomials of odd order and why the factor $1/2$ disappears in equation (54).
Combing equations (54) and (47), the conformal factor can expanded as

$$\begin{aligned} \phi &= \phi_{\text{reg}} + \phi_{\text{BL}} \\ &= 1 + P^2 L^2 \, {}^{(2)}\phi + \frac{m}{2\|\mathbf{R} - \mathbf{R}_1\|} + \frac{m}{2\|\mathbf{R} - \mathbf{R}_2\|} + O(L^4) \\ &= \left(1 + \frac{M}{2R}\right) + \frac{ML^2}{8R^3} P_2[\cos(\theta)] + P^2 L^2 \, {}^{(2)}\phi + \frac{ML^4}{32R^5} P_4[\cos(\theta)] + O(L^5) \end{aligned} \tag{55}$$

In further sections, only the first order Zerilli equation is used. We therefore only consider calculations up to L^2, P^2 or PL in this section. For calculations up to second order, see Appendix B.1.
Using the fact that the metric will be expanded in Legendre Polynomials, the only relevant terms of ϕ^4 are

$$4\left(1 + \frac{M}{2R}\right)^3 \frac{ML^2}{8R^3} P_2[\cos(\theta)] + \left(1 + \frac{M}{2R}\right)^4. \tag{56}$$

In equation (56), the extra coefficients in front of the terms are because multiple crossterms contribute to the same term.
Just like in [52], we use the approximation

$$\phi^2 \approx \phi^2_{\mathrm{Mis}} \approx \phi^2_{\mathrm{Schw}} = \left(1+\frac{M}{2R}\right)^2 = \frac{\left(R+\frac{M}{2}\right)^2}{R^2} = \frac{\frac{\left(R+\frac{M}{2}\right)^2}{R}}{R} = \frac{r}{R} == \frac{1}{\sqrt{1-2M/r}}\frac{\mathrm{d}r}{\mathrm{d}R}. \tag{57}$$

Using equation (57), we see that $\frac{R}{r} \approx \left(1+\frac{M}{2R}\right)^{-2}$. It therefore follows that

$$\begin{aligned}\left(\phi^4\frac{R^2}{r^2}\right)^{(l=2)} &\approx \left[4\left(1+\frac{M}{2R}\right)^{-1}\frac{ML^2}{8R^3}P_2\left[\cos(\theta)\right]+1\right]^{(l=2)} \\ &= \left(1+\frac{M}{2R}\right)^{-1}\frac{ML^2}{2R^3}.\end{aligned} \tag{58}$$

3.1.2 Conclusion

We therefore conclude that

$$H_2^{(l=2)} = K^{(l=2)} = \frac{16ML^2}{\sqrt{r}(\sqrt{r}+\sqrt{r-2M})^5}, \tag{59}$$

which is the same first order term as [57].

3.2 Perturbation coefficients of the extrinsic curvature

Let us now consider the extrinsic curvature K_{ab}. Similar to Section 3.1.1, we are considering a spherically symmetric tensor, which means that we can use the Regge-Wheeler notation for the perturbations

$$K_{rr} = \left(1-\frac{2M}{r}\right)^{-1}\sum_l KH_2^{(l)}(r,t)P_l[\cos(\theta)] \tag{60a}$$

$$K_{r\theta} = \sum_l Kh_1^{(l)}(r,t)\partial_\theta P_l[\cos(\theta)] \tag{60b}$$

$$K_{\theta\theta} = r^2\sum_l\left[KK^{(l)}(r,t)+KG^{(l)}(r,t){\partial_\theta}^2\right]P_l[\cos(\theta)] \tag{60c}$$

$$K_{\phi\phi} = r^2\sin(\theta)^2\sum_l\left[KK^{(l)}(r,t)+KG^{(l)}(r,t)\cot(\theta)\partial_\theta\right]P_l[\cos(\theta)]. \tag{60d}$$

3.2.1 Extrinsic curvature in non-flat space-time

There is no explicit calculation of the extrinsic curvature in [57], so this section is based on [52] which is referenced in [57].
In this section, we are going to work towards the extrinsic curvature K^{tot}_{ab} related to the basis $x^a = (r,\theta,\phi)$, where r and R are related by equation (51). Note that $K^{\mathrm{tot}}_{ab} = \phi^{-2}\hat{K}^{\mathrm{tot}}_{ab}$, where ϕ is the conformal factor. The approximation of ϕ is the same as highlighted in equation (57), namely

$$\phi^2 \approx \left(1+\frac{M}{2R}\right)^2 = \frac{r}{R} = \frac{1}{\sqrt{1-2M/r}}\frac{\mathrm{d}r}{\mathrm{d}R}. \tag{61}$$

Combining the conformal relation and the coordinate transformation, we get

$$K_{ab}^{\text{tot}} = \frac{R}{r}\frac{\partial \hat{x}^i}{\partial x^a}\frac{\partial \hat{x}^j}{\partial x^b}\hat{K}_{ij}^{\text{tot}}. \tag{62}$$

Note that R is only dependent on r and that the angles remain the same. This implies that

$$K_{ab}^{\text{tot}} = \frac{3PL}{2R^2 r}\begin{pmatrix} -4\cos(\theta)^2\left(\frac{\mathrm{d}R}{\mathrm{d}r}\right)^2 & 0 & 0 \\ 0 & R^2\left[\cos(\theta)^2+1\right] & 0 \\ 0 & 0 & R^2\sin(\theta)^2[3\cos(\theta)^2-1] \end{pmatrix} - \frac{3PL^3}{16R^4 r}$$
$$\begin{pmatrix} \left(\frac{\mathrm{d}R}{\mathrm{d}r}\right)^2[2-36\cos(\theta)^2+50\cos(\theta)^4] & 4R\frac{\mathrm{d}R}{\mathrm{d}r}\sin(\theta)\cos(\theta)[-1+5\cos(\theta)^2] & 0 \\ \text{Sym} & R^2[1+6\cos(\theta)^2-15\cos(\theta)^4] & 0 \\ 0 & 0 & R^2[-1+33\cos(\theta)^2-65\cos(\theta)^4+35\cos(\theta)^6] \end{pmatrix}$$
$$= \frac{3PL}{2r^3}\begin{pmatrix} \frac{-4\cos(\theta)^2}{\left(1-\frac{2M}{r}\right)} & 0 & 0 \\ 0 & r^2\left[\cos(\theta)^2+1\right] & 0 \\ 0 & 0 & r^2\sin(\theta)^2[3\cos(\theta)^2-1] \end{pmatrix} - \frac{3PL^3}{\left(\sqrt{r-2M}+\sqrt{r}\right)^4 r}$$
$$\begin{pmatrix} \frac{2\left(25\cos(\theta)^4-18\cos(\theta)^2+1\right)}{r^2\left(1-\frac{2M}{r}\right)} & \frac{4\sin(\theta)\cos(\theta)\left(5\cos(\theta)^2-1\right)}{\sqrt{1-\frac{2M}{r}}\,r} & 0 \\ \text{Sym} & \left(-15\cos(\theta)^4+6\cos(\theta)^2+1\right) & 0 \\ 0 & 0 & \left(35\cos^6(\theta)-65\cos(\theta)^4+33\cos(\theta)^2-3\right) \end{pmatrix}, \tag{63}$$

where we used that $dR/dr = R/\sqrt{r(r-2M)}$.
Looking at equation (63) we see that the first order agrees with the paper [57]. However we are unable to compare second order results, as they don't give any explicit form for the second order term. From now on, we shall refer to K_{ab}^{tot} as K_{ab}.

3.2.2 Expansion of extrinsic curvature

In this section, the leading order term of K_{ab} will be expanded, i.e. the term proportional to PL term in equation (63). The expansion of the second order term is calculated in Appendix B.3.
First, let us consider the K_{rr} component. We need to find $KH_2^{(0)}(r,t)$ and $KH_2^{(2)}(r,t)$ such that

$$KH_2^{(l=0)}(r,t) + KH_2^{(l=2)}(r,t)\frac{1}{2}\left[3\cos^2(\theta)-1\right] = \frac{-6PL}{r^3}\cos(\theta)^2, \tag{64}$$

which implies

$$KH_2^{(l=2)}(r,t) = \frac{-4PL}{r^3} \tag{65}$$

$$KH_2^{(l=0)}(r,t) = \frac{1}{2}KH_2^{(l=2)} = \frac{-2PL}{r^3}. \tag{66}$$

Now, consider the $K_{\theta\theta}$ and $K_{\phi\phi}$ terms. We need to find $KK^{(l=0)}(r,t)$, $KK^{(l=2)}(r,t)$ and $KG_2^{(l=2)}(r,t)$ such that

$$KK^{(0)}(r,t) + KK^{(l=2)}(r,t)\frac{1}{2}\left[3\cos^2(\theta)-1\right] + KG^{(l=2)}(r,t)3\left[1-2\cos^2(\theta)\right] = \frac{-3PL}{2r^3}\left[\cos(\theta)^2+1\right] \tag{67}$$

$$KK^{(l=0)}(r,t) + KK^{(l=2)}(r,t)\frac{1}{2}\left[3\cos^2(\theta) - 1\right] - KG^{(l=2)}(r,t)3\cos^2(\theta) = \frac{-3PL}{2r^3}\left[3\cos(\theta)^2 - 1\right]. \quad (68)$$

By substracting the two lines from eachother, $KG_2^{(l=2)}(r,t)$ can be deteremined

$$\begin{aligned} KG^{(l=2)}(r,t)3\left[1 - 2\cos^2(\theta)\right] + KG^{(l=2)}(r,t)3\cos^2(\theta) &= \frac{3PL}{2r^3}\left[\cos(\theta)^2 + 1\right] - \frac{3PL}{2r^3}\left[3\cos(\theta)^2 - 1\right] \\ KG^{(l=2)}(r,t)\left[3 - 3\cos(\theta)^2\right] &= -\frac{3PL}{2r^3}\left[2\cos(\theta)^2 - 2\right] \\ KG^{(l=2)}(r,t) &= \frac{PL}{r^3}, \end{aligned} \quad (69)$$

which is the same as in [57].
Filling in equation (69) into equation (67), we get

$$\begin{aligned} KK^{(l=0)}(r,t) + KK^{(l=2)}(r,t)\frac{1}{2}\left[3\cos^2(\theta) - 1\right] + \frac{3PL}{r^3}\left[1 - 2\cos^2(\theta)\right] &= \frac{3PL}{2r^3}\left[\cos(\theta)^2 + 1\right] \\ KK^{(l=0)}(r,t) + KK^{(l=2)}(r,t)\frac{1}{2}\left[3\cos^2(\theta) - 1\right] &= \frac{3PL}{2r^3}\left[5\cos(\theta)^2 - 1\right], \end{aligned} \quad (70)$$

which means

$$KK^{(l=2)}(r,t) = \frac{5PL}{r^3} \quad (71)$$

$$KK^{(l=0)}(r,t) = \frac{1}{5}KK_2^{(l=0)} = \frac{PL}{r^3}. \quad (72)$$

3.2.3 Conclusion

We therefore conclude that

$$KH_2^{(l=0)}(r,t) = \frac{-2PL}{r^3} \quad (73a)$$

$$KH_2^{(l=2)}(r,t) = \frac{-4PL}{r^3} \quad (73b)$$

$$KG^{(l=0)}(r,t) = 0 \quad (73c)$$

$$KG^{(l=2)}(r,t) = \frac{PL}{r^3} \quad (73d)$$

$$KK^{(l=0)}(r,t) = \frac{PL}{r^3} \quad (73e)$$

$$KK^{(l=2)}(r,t) = \frac{5PL}{r^3} \quad (73f)$$

$$Kh_1^{(l=0)} = Kh_1^{(l=2)} = 0. \quad (73g)$$

These results agree with [56], but differ by a factor -1.

4 Casting the initial data

There are many different Zerilli equations and functions that follow from the Einstein Field Equations (see Appendix 3.1). In this thesis, we will work with the gauge invariant formalism based on the paper by Poisson and Martel [69] and by Martel's PhD thesis [70].[6] In this section, we will introduce the formalism and calculate the initial data for the Zerilli wave function ψ and its derivatives.

4.1 Notation

Before we introduce the Zerilli equation, it is useful to introduce some new notation.
The Zerilli equation gets an easier form, if we use the Tortoise coordinate r_*

$$\begin{aligned} r_* &:= r + 2M \log\left[\frac{r}{2M} - 1\right] \\ \frac{d}{dr_*} &= \frac{\Delta}{r^2}\frac{d}{dr} \end{aligned} \tag{74}$$

Expressing r as a function of r_* is determined by

$$\begin{aligned} e^{r_*} &= e^{r+2M\log\left[\frac{r}{2M}-1\right]} = e^r e^{\log\left[\left(\frac{r}{2M}-1\right)^{2M}\right]} = e^r\left(\frac{r}{2M}-1\right)^{2M} \\ \implies & e^{\frac{r_*}{2M}-1} = e^{\frac{r}{2M}-1}\left(\frac{r}{2M}-1\right) \\ \implies & \left(\frac{r}{2M}-1\right) = W_0\left(e^{\frac{r_*}{2M}-1}\right) \\ \implies & r = 2M\left(1 + W_0\left(e^{\frac{r_*}{2M}-1}\right)\right), \end{aligned} \tag{75}$$

where W_0 is the principle Lambert-W function. Note that both r and r_* are real and $r > 2M$. This implies $\frac{r}{2M} - 1 \geq 0$, which is why we take the principle Lambert function W_0 and not any other W_k.
The following identities will be useful when changing coordinates

$$\frac{\partial r_*}{\partial r} = \frac{r}{r-2M} = \frac{1}{1-\frac{2M}{r}} \implies \frac{\partial r}{\partial r_*} = 1 - \frac{2M}{r} \tag{76}$$

$$\frac{\partial^2 r}{\partial r_*^2} = \left(1-\frac{2M}{r}\right)\frac{\partial}{\partial r}\left(\frac{\partial r}{\partial r_*}\right) = \left(1-\frac{2M}{r}\right)\frac{\partial}{\partial r}\left(1-\frac{2M}{r}\right) = -\left(1-\frac{2M}{r}\right)\frac{2M}{r^2}. \tag{77}$$

Lastly, we define

$$\Lambda := (l-1)(l+2) + \frac{6M}{r} \tag{78}$$

$$\mu := (l-1)(l+2) \tag{79}$$

This is different from the convention used by Chandrasekhar [34], Martel [70] and Nicasio et et al. [56], which use

$$\Lambda_{\mathrm{Mart}} = \frac{1}{2}\Lambda \tag{80}$$

$$\mu_{\mathrm{Ch}}^2 = 2n_{\mathrm{Ch}} = \mu = 2\lambda_{\mathrm{Nic}} = 2\lambda_{\mathrm{Mart}}. \tag{81}$$

.

[6] Here we do not mean gauge fixed but actually gauge invariant

4.2 Zerilli equation and function

The Zerilli equation given by Poisson and Martel is

$$\begin{aligned} &-\frac{\partial^2\psi}{\partial t^2}+\left(1-\frac{2M}{r}\right)^2\frac{\partial^2\psi}{\partial r^2}-\left(1-\frac{2M}{r}\right)\frac{2M}{r^2}\frac{\partial\psi}{\partial r}-V(r)\psi. \\ &=-\frac{\partial^2\psi}{\partial t^2}+\frac{\partial^2\psi}{\partial r_*^2}-V(r)\psi=0 \end{aligned} \tag{82}$$

with r_* being the tortoise coordinate (74) and

$$\begin{aligned} V(r)&=\frac{\left(1-\frac{2M}{r}\right)}{\left((l-1)(l+2)-\frac{6M}{r}\right)^2}\left\{(l-1)^2(l-2)^2\left[\frac{(l-1)(l-2)+2}{r^2}+\frac{6M}{r^3}\right]+\frac{36M^2}{r^4}\left[(l-1)(l-2)+\frac{2M}{r}\right]\right\} \\ &=\frac{\left(1-\frac{2M}{r}\right)}{\Lambda^2}\left\{\mu^2\left[\frac{\mu+2}{r^2}+\frac{6M}{r^3}\right]+\frac{36M^2}{r^4}\left[\mu+\frac{2M}{r}\right]\right\}. \end{aligned} \tag{83}$$

In equation (82) we use that

$$\frac{\partial^2\psi}{\partial r_*^2}=\frac{\partial}{\partial r_*}\left(\frac{\partial r}{\partial r_*}\frac{\partial\psi}{\partial r}\right)=\frac{\partial^2 r}{\partial r_*^2}\frac{\partial\psi}{\partial r}+\frac{\partial r}{\partial r_*}\frac{\partial r}{\partial r_*}\frac{\partial}{\partial r}\frac{\partial\psi}{\partial r}=\frac{\partial^2 r}{\partial r_*^2}\frac{\partial\psi}{\partial r}+\left(\frac{\partial r}{\partial r_*}\right)^2\frac{\partial^2\psi}{\partial r^2}, \tag{84}$$

as well as equations (76) and (77).

The gauge invariant Zerilli function ψ is defined using gauge invariant quantities. These gauge invariant quantities are expressed using the metric perturbations given in Section 3, namely

$$\begin{aligned} \tilde{H}_2&=H_2-2\nabla_r h_1+4\nabla_r r\nabla_r G+r^2\nabla_r\nabla_r G \\ &=H_2-2\partial_r h_1+4\partial_r G+r^2\left(\partial_r\partial_r G-\Gamma^a_{rr}\partial_a G\right), \end{aligned} \tag{85}$$

$$\tilde{K}=K+\frac{1}{2}l(l+1)G-\frac{2}{r}h_1+r\partial_r G \tag{86}$$

where we omitted the l index. In the Regge Wheeler gauge the gauge invariant quantities are the same as the metric perturbations, $\tilde{K}=K$ and $\tilde{H}_2=H_2$, because $h_1=0=G$.

The gauge invariant Zerilli function is defined as

$$\psi=\frac{2r}{l(l+1)}\left\{\tilde{K}+\frac{2}{\Lambda}\left[\left(1-\frac{2M}{r}\right)^2\tilde{H}_2-r\left(1-\frac{2M}{r}\right)\partial_r\tilde{K}\right]\right\}. \tag{87}$$

The above definitions differ from the terms in the formalism given by Gleiser et al. The above potential in equation (83) has a different form than the one given by Gleiser et al. [56] Both forms also differ from the one originally given by Zerilli [71] which they consequently use when creating their second order formalism [72]. As a consequence, each paper also has a different Zerilli function. For this reason, we opt to go for the gauge invariant form.

4.3 Initial data for the Zerilli Function

Having introduced the Zerilli function in equation (87), we can calculate its initial value at $t=0$. After which, we can use the Zerilli equation (82) to evolve the Zerilli function to later times.

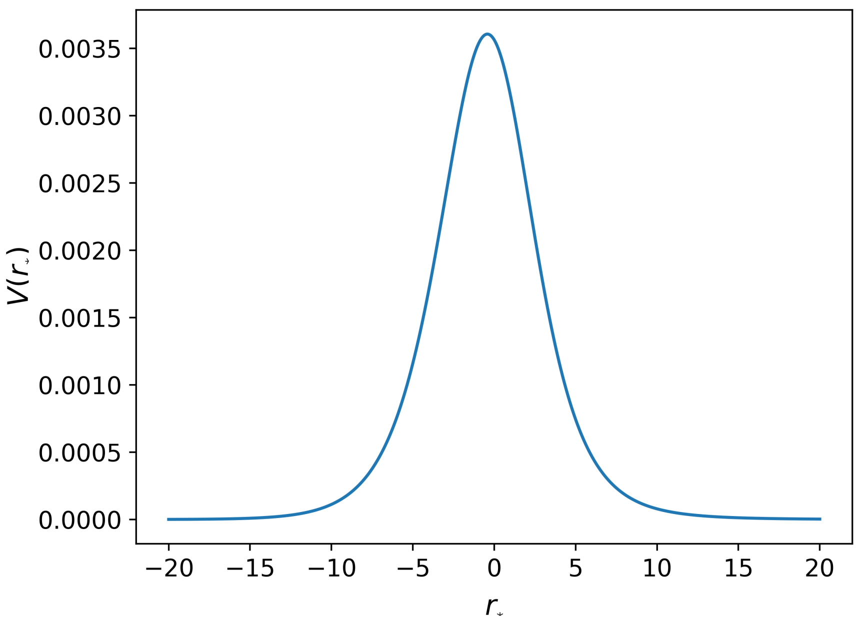

Figure 6: Potential from equation (83) with $M = 1$ and $l = 2$ plotted against r_*. The maximum of the potential is at $r_* = 0$.

It is easy to calculate the Zerilli function at $t = 0$, as this only involves filling in equation (87) with the coefficients of the metric calculated in Section 4. Calculating $\partial_r\psi$ can . These calculations can be done explicitely, but the results are not insightfull. Besides, to make the numerical solver more generically applicable, we have opted to code the initial data of ψ as a function of the coefficients which can adapted in the solver. We therefore forego explicitely calculating the initial data for ψ and $\partial_t\psi$ in this section and instead refer to Appendix E.

Calculating the time derivative of the Zerilli function is more involved. We will use the following relation between the i-th order perturbations of the spatial metric and extrinsic curvature as explained in Section A.5

$$
\begin{aligned}
{}^{(i)}K_{ab} &= \frac{1}{2N}\left(\partial_t\, {}^{(i)}\gamma_{ab} - D_a\, {}^{(i)}N_b - D_b\, {}^{(i)}N_a\right) \\
&= \frac{1}{2}\frac{1}{\sqrt{1-\frac{2M}{r}}}\left(\frac{\partial}{\partial t}\, {}^{(i)}\gamma_{ab}\right),
\end{aligned} \tag{88}
$$

where $\mathbf{n}$ is the unit normal vector field, γ_{ab} is the spatial metric on ${}^{(3)}\Sigma_t$, N is the lapse function, N_a are components of the shift vector and D the covariant derivative defined on the original timeslice ${}^{(3)}\Sigma_0$. In equation (88) we use the fact that there is zero perturbative shift for each l-mode [65]. The first order perturbative lapse function is technically not zero for the $l = 0$ mode, but since all other metric coefficients with $l = 0$ in equation (88) are zero, this term does not contribute. Other $l-$modes for the lapse function are zero at first order.

Taking the time-derivative of the Zerilli function as defined in equation (87) gives us

$$
\partial_t\psi = \frac{2r}{l(l+1)}\left\{\partial_t\tilde{K} + \frac{2}{\Lambda}\left[\left(1-\frac{2M}{r}\right)^2\partial_t\tilde{H}_2 - r\left(1-\frac{2M}{r}\right)\partial_t\partial_r\tilde{K}\right]\right\}. \tag{89}
$$

Using equation (88) we get

$$
\begin{aligned}
\partial_t\tilde{K} &= \partial_t K + \frac{1}{2}l(l+1)\partial_t G - \frac{2}{r}\partial_t h_1 + r\partial_t\partial_r G \\
&= 2\sqrt{1-\frac{2M}{r}}KK + l(l+1)\sqrt{1-\frac{2M}{r}}KG - \frac{4}{r}\sqrt{1-\frac{2M}{r}}Kh_1 + r\partial_r\left(\sqrt{1-\frac{2M}{r}}KG\right) \\
&= 2\sqrt{1-\frac{2M}{r}}KK + \left[l(l+1)\sqrt{1-\frac{2M}{r}} + \frac{M}{\sqrt{1-\frac{2M}{r}}\,r}\right]KG - \frac{4}{r}\sqrt{1-\frac{2M}{r}}Kh_1 + r\sqrt{1-\frac{2M}{r}}\partial_r KG \\
&= \sqrt{1-\frac{2M}{r}}\left[2KK + \left(l(l+1) + \frac{M}{r-2M}\right)KG - \frac{4}{r}Kh_1 + r\partial_r KG\right]
\end{aligned}
\tag{90}
$$

and

$$
\begin{aligned}
\partial_t\tilde{H}_2 &= \partial_t H_2 - 2\partial_r\partial_t h_1 + 4\partial_r\partial_t G + r^2\left(\partial_r\partial_r\partial_t G - \Gamma^a_{rr}\partial_a\partial_t G\right) \\
&= \sqrt{1-\frac{2M}{r}}KH_2 + \frac{M}{\sqrt{1-\frac{2M}{r}}\,r}\left[-2Kh_1 + 4KG\right] - 2\sqrt{1-\frac{2M}{r}}\partial_r Kh_1 + 4\sqrt{1-\frac{2M}{r}}\partial_r KG \\
&+ r^2\left[\frac{M\,(2r-3M)}{\left(1-\frac{2M}{r}\right)^{\frac{3}{2}}r^4}KG + 2\frac{M}{\sqrt{1-\frac{2M}{r}}\,r}\partial_r KG + \sqrt{1-\frac{2M}{r}}\partial_r\partial_r KG\right] \\
&- r^2\frac{-M}{(1-\frac{2M}{r})r^2}\left[\frac{M}{\sqrt{1-\frac{2M}{r}}\,r}KG + \sqrt{1-\frac{2M}{r}}\partial_r KG\right] \\
&= \sqrt{1-\frac{2M}{r}}\Bigg[KH_2 - 2\partial_r Kh_1 + 4\partial_r KG + r^2\partial_r\partial_r KG + \frac{M}{1-\frac{2M}{r}}\partial_r KG \\
&+ \frac{M}{r-2M}\left(-2Kh_1 + 4KG + 2r^2\partial_r KG + \frac{M}{1-\frac{2M}{r}}KG\right) + \frac{Mr^2\,(2r-3M)}{(r-2M)^4}KG\Bigg],
\end{aligned}
\tag{91}
$$

where we used that none of the Christoffel symbols have a t-dependence and that $\Gamma^t_{rr} = 0$. We can fill in equations (90) and (91) into equation (89) to get the full expression of $\partial_t\psi$ at $t = 0$. However, the explicit form would be long, messy and not informative. We therefore forego writing it here.

5 Ordinary and Partial Differential Equations

The Zerilli equation is a second order Partial Differential Equation (PDE) that we will numerically solve for the Zerilli function $\psi(r,t)$. To understand the numerical solver, it is necessary to understand some concepts from Ordinary Differential Equations (ODE), as well as PDEs. We will reduce the second order PDE to a three first order ODEs using the method of lines and method of characteristics. We then solve the ODEs using the Runge Kutta method.
We begin by introducing the notation for ODEs and the concept of convergence and consistency. The Runge-Kutta method is then presented, which will be used to get numerical approximations for the Zerilli function at later times. Subsequently, we extend the notation to PDEs and outline the reduction of PDEs to ODEs via the method of lines and the method of characteristics. We conclude by applying these methods to the Zerilli equation.

5.1 Ordinary Differential Equations

Let us consider a set of n functions $\{u_i(t)\}$ on the interval $[0,T]$ that satisfies a set of ODEs

$$\frac{du_i(t)}{dt} = u_i'(t) = f_i\left(t, u_1(t), ..., u_n(t)\right) = f_i\left(t, \vec{u}(t)\right) \tag{92}$$

for $t \in [0,T]$. Assume that the equations satisfy the initial data

$$u_i(0) = u_{i,0}. \tag{93}$$

According to Picard's theorem, there is a unique solution to the problem on the time domain $[0,T]$, if the vector of functions $f = (f_i) : [0,T] \times \mathbb{R}^n \to \mathbb{R}^n$ is continuous and satisfies the Lipschitz condition with respect to $L \in \mathbb{R}$

$$\|f(t,\vec{v}) - f(t,\vec{\tilde{v}})\| \leq L\|\vec{v} - \vec{\tilde{v}}\| \qquad \forall t \in [0,T] \quad \forall \vec{v}, \vec{v} \in \mathbb{R}. \tag{94}$$

We divide the time-domain $[0,T]$ into a finite amount N of steps with size τ. We define $t_n := n\tau \in [0,T]$ to be the nth timestamp. We will use numerical approximations to get values of the functions u_i at the different timestamps. The approximation of u_i at timestamp t_n will be denoted by $u_{i,n}$.
Consider a method, which gives us approximations for the functions $u_i(t)$ at all the time steps between 0 and T. The **local (truncation) error** d_n is the error the method introduces when going from the $(n-1)$th time step to the nth time step. It is therefore defined as the difference between the exact solution $u_i(t_n)$ and the approximation obtained by applying one step of the method to the exact value at t_{n-1}. To clarify this concept, suppose that the method gives a numerical approximation $u_{i,n}$ based on the previous approximation $u_{i,n-1}$ in the following way

$$u_{i,n} = u_{i,n-1} + \tau\Psi(t_{n-1}, u_{i,n-1}). \tag{95}$$

The local error d_n is then defined by

$$d_n = \frac{1}{\tau}\left(u_i(t_n) - u_i(t_{n-1})\right) - \Psi(t_{n-1}, u_i(t_{n-1})). \tag{96}$$

The local error is therefore the difference between the actual solution $u_i(t_n)$ and the numerical approximation $u_{i,n}$ one gets from using the approximation method which uses the actual solution $u_i(t_{n-1})$ as input. The method is **consistent of order p** if for all approximations of u_i the local error satisfies $d_n = O(\tau^p)$ as $\tau \to 0$

uniformly for t_n.
Consider the same context as above, we can define the **global error** e_n as

$$e_n = u_i(t_n) - u_{i,n}, \tag{97}$$

which means that the global error is the difference between the actual solution and the approximation given by the method. The method is called **convergent of order p** if for each timestamp t_n the global error $e_n = O(\tau^p)$ for $\tau \to 0$ [73].

5.1.1 Runge-Kutta method

The Runge-Kutta method is a family of methods that solves ODEs of the form of equations (92) and (93), using intermediate approximations.
Let us consider the numerical approximation of the function u_i. Between each approximation $u_{i,n-1}$ and $u_{i,n}$, we will use s intermediate approximations $v_{n,j}$ of the form

$$v_{n,i} = u_{n-1} + \tau \sum_{j=1}^{s} a_{ij} f\left(t_{n-1} + c_j\tau, v_{n-1,j}\right) \tag{98}$$

$$u_n = u_{n-1} + \tau \sum_{j=1}^{s} b_j f\left(t_{n-1} + c_j\tau, v_{n,j}\right). \tag{99}$$

The coefficients b_i are called weights, c_i are nodes and a_{ij} is related to c_j by

$$c_i = \sum_{j=1}^{s} a_{ij}. \tag{100}$$

The method is called **explicit** if $j \geq i \implies a_{ij} = 0$ and **implicit** if that is not the case. If the method is explicit, each stage k_i only depends on the previous stages. If the method is implicit, some stages k_i depend on themselves or other stages that have not yet been calculated. This means that one needs to solve equations that are often non-linear in order to get k_i.
To obtain an RK-method with a specific consistency or convergence order, specific condition on b_i, c_i and a_{ij} must be satisfied. A discussion of the specific conditions is outside the scope of this thesis. We will specifically use the RK4 method, also called the classic Runge-Kutta method. This method has a consistency of order 4 and a convergence of order 4.
Take unknown function $u(t)$, which satisfies the conditions of equations (92) and (93). We define the intermediate approximations via [7]

$$k_1 = f(t_n, u_n), \tag{101a}$$

$$k_2 = f\left(t_n + \frac{\tau}{2}, u_n + \tau\frac{k_1}{2}\right), \tag{101b}$$

$$k_3 = f\left(t_n + \frac{\tau}{2}, u_n + \tau\frac{k_2}{2}\right), \tag{101c}$$

[7] In our application, we are considering ODEs of the form $f(u(t))$ (an autonomous system) and not $f(t, u(t))$ (a non-autonomous system), since we don't have a specific time-dependence. However, this does not change the approximations beyond being able to ignore the t-component in the function. Any convergence and consistency conditions placed on c_i are still satisfied via conditions placed on a_{ij} via equation (100).

$$k_4 = f(t_n + \tau, u_n + \tau k_3)\,. \tag{101d}$$

Here, k_1 is the approximation of the slope of $u(t)$ at t_n. The values k_2 and k_3 are the slopes at $t_n + \tau/2$ which uses k_1 and k_2, respectively, to get the approximation for $u(t_n + \tau/2)$. The value of k_4 is the slope at the t_{n+1}, which uses the approximation of $u(t_{n+1})$ that is based on k_3.
The approximation for $u(t_{n+1})$ is given by

$$u_{n+1} = u_n + \frac{\tau}{6}\left(k_1 + 2k_2 + 2k_3 + k_4\right). \tag{102}$$

5.2 Partial Differential Equations

We wish to apply the Runge-Kutta method to PDEs, since we can find methods with consistency and convergence of order p in this class of methods. To apply the RK4 method to our PDE, we will use the method of lines and method of characteristics, which transforms the PDE into initial-value problems for systems of ODEs [74, 75]. Before we can explain these methods, we will need discuss the characterisation of PDEs.

5.2.1 Categorization

Suppose there is a set of n functions $u = (u_i)$ that are dependent on one time coordinate t and k spatial coordinates x_j, such that $u_i : [0, T] \times \mathbb{R}^k \to \mathbb{R}$. We only consider second order PDEs, which means that the highest order partial derivatives are of second order. A second order PDE is called **linear**, if it is linear in all of its derivatives and the coefficients are only dependent on the coordinates, e.g. it is of the form

$$\sum_{ij} A_{ij}(t, \vec{x})\partial_i\partial_j u + \sum_i B_i(t, \vec{x})\partial_i u + C(t, \vec{x})u = D(t, \vec{x}). \tag{103}$$

A PDE is called **semi-linear** if the highest derivatives are of linear form and have coefficients which only depend on the coordinates. This means that the lower derivatives can have an arbitrary form, e.g. the equation can be written as

$$\sum_{ij} A_{ij}(t, \vec{x})\partial_i\partial_j u + F(t, \vec{x}, \partial_i u) = D(t, \vec{x}). \tag{104}$$

A PDE is **quasi-linear** if the highest order derivatives are of linear form and the coefficients are dependent on the unknown function, its lower derivatives and potentially coordinates, e.g.

$$\sum_{ij} A_{ij}(t, \vec{x}, \partial_l u, u)\partial_i\partial_j u + F(t, \vec{x}, \partial_i u) = D(t, \vec{x}). \tag{105}$$

A PDE that has none of the linearity properties highlighted above, is called **fully nonlinear**.
Suppose we have a set of n functions $u = (u_i)$ that are dependent on one time coordinate t and k spatial coordinates x_j, such that $u_i : [0, T] \times \mathbb{R}^k \to \mathbb{R}$. Assume that they satisfy a second order linear partial differential equation on the domain $[0, T] \times_i [0, X_i]$ of the form (103). The equation is called **homogeneous** if in equation (103) we have $D(t, \vec{x}) = 0$ and **non-homogeneous** or **inhomogeneous** if this is not the case. A partial differential equation is called **elliptic** if the matrix A with matrix elements A_{ij} is positive or negative definite, which means that the eigenvalues are non-zero and have the same sign. A PDE is **parabolic** when matrix A is semi-definite. In the context of second order PDEs, this means that exactly one eigenvalue of A is zero. A PDE is called **hyperbolic** if A has only non-zero eigenvalues such that all but

one have the same sign.
Looking at equation (82), we can see that for the Zerilli equation in coordinates t, r_* we have

$$A = \begin{pmatrix} -1 & 0 \\ 0 & 1 - \frac{2M}{r} \end{pmatrix}, \qquad \vec{B} = \begin{pmatrix} 0 \\ 0 \end{pmatrix}, \qquad C(t, r_*) = V(r_*), \qquad D(t, r_*) = 0. \tag{106}$$

As we can see from (106), the Zerilli equation (82) is a homogenous hyperbolic second order linear partial differential equation.

5.2.2 Method of lines

The method of lines reduces the second order PDE to a second order ODE by keeping the t-dimension continuous, while discretizing the spatial dimensions. This is done by replacing the spatial derivatives at the boundary with algebraic approximations, such that spatial derivatives are not given by spatial independent variables [76].
Let us consider a set of n functions $u = (u_i)$ that are dependent on both t and k spatial coordinates x_j, such that $u_i : [0, T] \times \mathbb{R}^k \to \mathbb{R}$. Assume that they satisfy a partial differential equation on the domain $[0, T] \times_i [0, X_i]$ of the form (103). Suppose r is the k'th spatial coordinate with the domain $[0, R]$ which is partioned into m equal steps Δr. The partial derivative of u with respect to r at time t, spatial coordinates $x_1, ..., x_{k-1}, i\Delta r$ can be approximated by

$$\begin{aligned} \frac{\partial u(t, x_1, ..., x_{k-1}, i\Delta r)}{\partial r} &= \frac{u(t, x_1, ..., x_{k-1}, i\Delta r)) - u(t, x_1, ..., x_{k-1}, (i-1)\Delta r)}{\Delta r} + O(\Delta r) \\ &= \frac{u_{k,i}(t, x_1, ..., x_{k-1}) - u_{k,i-1}(t, x_1, ..., x_{k-1})}{\Delta r} + O(\Delta r) \\ &= \frac{u_{k,i} - u_{k,i-1}}{\Delta r} + O(\Delta r), \end{aligned} \tag{107}$$

where k subscript indicates here which coordinate we are considering and the i subscript which place in the grid we are comparing. This method is called the **finite difference** method [77]. The second order derivative with respect to r at time t, spatial coordinates $x_1, ..., x_{k-1}, i\Delta r$ can be approximated by

$$\frac{\partial^2 u(t, x_1, ..., x_{k-1}, i\Delta r)}{\partial r^2} = \frac{u_{k,i+1} - 2u_{k,i} + u_{k,i-1}}{\Delta r^2} + O\left(\Delta r^2\right), \tag{108}$$

which is only defined for internal grid points of the interval, e.g. for $0 < i < m$.
To approximate the time derivative in the same way, it is necesaary to take a time step τ that is small enough. If the time step is too large, the calculations become unstable in the sense that the difference $u_{k,i}((j+1)\tau, \vec{x}) - u_{k,i}(j\tau, \vec{x})$ grows and becomes unbounded. We therefore introduce a constant which relate the step in the time domain τ with the step in the spatial domain Δx_k. This is called the **Courant-Friedricks-Lewy** number c_{CFL} (in the code denoted by cfl) [78, 79].
To highlight this, consider a simple one-dimensional wave equation for the function $u(t, x)$ of the form

$$\frac{\partial u}{\partial t} = w \frac{\partial u(x, t)}{\partial x}, \tag{109}$$

where w denotes the velocity in the x direction. After discretization one has at the internal points $t = i\tau, x = j\Delta x$

$$\frac{u\left((i+1)\tau, j\Delta x\right) - u(i\tau, j\Delta x)}{\tau} = w \frac{u\left(i\tau, j\Delta x\right) - u\left(i\tau, (j-1)\Delta x\right)}{\Delta x} \tag{110}$$

which implies

$$
\begin{aligned}
u\left((i+1)\tau\right) &= u\left(i\tau\right) + \tau w \frac{u\left(i\tau, j\Delta x\right) - u\left(i\tau, (j-1)\Delta x\right)}{\Delta x}, \\
&= u\left(i\tau\right) + c_{\mathrm{CFL}}\left[u\left(i\tau, j\Delta x\right) - u\left(i\tau, (j-1)\Delta x\right)\right] \\
&= \left[1 + c_{\mathrm{CFL}}\right] u\left(i\tau, j\Delta x\right) - c_{\mathrm{CFL}} u\left(i\tau, (j-1)\Delta x\right),
\end{aligned}
\tag{111}
$$

where the c_{CFL} constant has been implicitly defined as $w\frac{\tau}{\Delta x}$.
This Courant-Friedricks-Lewy number needs to be chosen well, as a CFL number that is larger than a specific critical value leads to the method to be unstable. This critical value is dependent on the system and has no general formula. In practice, the CFL number is fixed before the grid for the spatial dimensions is chosen. After the discretization for the spatial grid has been created, the time steps τ are varied to keep the CFL number constant. Increasing the accuracy of the method, e.g. picking a smaller step in the spatial domain Δx_k, means that one needs to introduce a smaller step in the temporal domain τ [80].

5.2.3 Method of characteristics

The method of characteristics is a way to reduce a set of PDEs to a set of ODEs or to reduce higher order PDEs to a set of lower order ODEs.
The principle behind this method is constructing a characteristic curves, along whichthePDE becomes a set of ODEs. Consider a function $u(\mathbf{x}) : \mathbb{R}^n \to \mathbb{R}$ which satisfies on $\Omega \subset \mathbb{R}^n$ a general homogenous first order PDE of the form

$$F(x_1, ..., x_n, u, \partial_1 u, ..., \partial_n u) = 0. \tag{112}$$

Suppose $\Gamma \subset \mathbb{R}^n$ is a submanifold of Ω parametrized by $(\gamma_1(\mathbf{r}), ..., \gamma_n(\mathbf{r}))$, where $\gamma_i : I \subset \mathbb{R}^{n-1} \to \mathbb{R}$ and $\mathbf{r} = (r_1, ..., r_{n-1}) \in \mathbb{R}^{n-1}$. The boundary condition for $u(\mathbf{x})$ is given by

$$u\big|_{\Gamma} = \phi. \tag{113}$$

Assume $u(\mathbf{x}) \in C^2(\Omega)$ is a solution of the PDE (112). Let $\mathbf{x}(s) : I \subset \mathbb{R} \to \mathbb{R}^n$ be a curve along which $u(\mathbf{x})$ solves the PDE (112), with initial condition $u(\mathbf{x}^0) = u_0 = \phi$ where $\mathbf{x}(0) = \mathbf{x}^0 = (x_1^0, ..., x_n^0) \in \Gamma$. We define $z(s) = u(\mathbf{x}(s)) : I \to \mathbb{R}$. Assume that all curves are twice differentiable.
We can create a curve $\mathbf{p} = (p_1(s), ..., p_n(s)) = (\partial_1 u(\mathbf{x}(s)), ..., \partial_n u(\mathbf{x}(s)))$ in $\mathbb{R}^n$ and $(\mathbf{x}(s), z(s), \mathbf{p}(s))$ in $\mathbb{R}^{2n+1}$, where $\partial_i = \dfrac{\partial}{\partial x_i}$. Note that by definition, we have $p_i(s) \in C^1(I)$. Taking a total derivative of equation (112) with respect to x_i gives us

$$\frac{dF}{dx_i} = \sum_j \frac{\partial F}{\partial p_j}\frac{\partial p_j}{\partial x_i} + \frac{\partial F}{\partial u}\frac{\partial u}{\partial x_i} + \partial_i F = 0. \tag{114}$$

Note that $\dfrac{\partial p_j}{\partial x_i} = \partial_i p_j = \partial_i \partial_j u$. If we place on x_i the condition

$$\frac{dx_i(s)}{ds} = \frac{\partial F(\mathbf{x}, z, \mathbf{p})}{\partial p_i}, \tag{115}$$

we can formulate equation (114) as an ODE for $p_i(s)$, namely

$$\sum_j \frac{\partial F}{\partial p_j}\frac{\partial p_j}{\partial x_i} = \sum_j \frac{dx_j(s)}{ds}(\partial_j \partial_i u) = \frac{dp_i}{ds} = -\frac{\partial F}{\partial u}\partial_i u - \partial_i F. \tag{116}$$

In equation (116) we have used the chain rule for p_i, given by

$$\frac{dp_i}{ds} = \frac{d(\partial_i u(x_j(s))}{ds} = \sum_j \frac{\partial(\partial_i u(x_j(s)))}{\partial x_j(s)} \frac{\partial x_j(s)}{\partial s} = \sum_j \frac{dx_i(s)}{ds}(\partial_j \partial_i u). \tag{117}$$

Lastly, we need to get an ODE for $u(s)$

$$\frac{dz}{ds} = \sum_j \frac{\partial u(x(s))}{\partial x_j} \frac{\partial x_j}{\partial s} = \sum_j p_j \frac{\partial F}{\partial p_j}. \tag{118}$$

In conclusion, we have turned the general homogenous PDE of equation (103) into a family of ODEs

$$\frac{dx_i}{ds} = \frac{\partial F(\mathbf{x}, u, \mathbf{p})}{\partial p_i}, \tag{119a}$$

$$\frac{dp_i}{ds} = -\frac{\partial F(\mathbf{x}, u, \mathbf{p})}{\partial u} \partial_i u - \partial_i F(\mathbf{x}, u, \mathbf{p}), \tag{119b}$$

$$\frac{dz}{ds} = \sum_j p_j \frac{\partial F(\mathbf{x}, u, \mathbf{p})}{\partial p_j}, \tag{119c}$$

which are called the **characteristic equations** [81–83].
So far we have not discussed the kind of surface Γ can be, nor what the initial conditions are for the ODEs (119). The initial conditions for $x_i(s)$ are $x_i(0) = x_i^0$ and for $z(s)$ they are $z(0) = \phi$. The condition for $p_i(0) = p_i^0$ are

$$F(\mathbf{x}^0, u_0, \mathbf{p}^0) = 0, \tag{120a}$$

$$\frac{d\phi(\mathbf{r})}{dr_i} = \sum_j p_j^0 \frac{\partial \gamma_j}{\partial r_i}, \tag{120b}$$

where $\mathbf{r}$ is such that $\gamma(\mathbf{r}) \in \Gamma$ and $i = 1, ..., n-1$ [81, 82, 84].
Finding functions $p_j(s)$ that satisfy (120) might not always be possible, nor are solutions always unique. However, if one has found (local) functions satisfying equations (120), the solution is unique. There are also conditions on the initial data which will guarantee a unique (local) solution. For example, if Γ is a coordinate hypersurface, e.g. $(x_1, ..., x_{n-1}) \in \Gamma$ if and only if $\mathbf{x} = (x_1, ..., x_{n-1}, a)$ is in $\Omega \subset \mathbb{R}^n$ for a value of a, then $\frac{\partial F(\mathbf{x}^0, u_0, \mathbf{p}^0)}{\partial p_n} \neq 0$ is sufficient condition for $\mathbf{p}$ to be unique. In the case where the hypersurface is two-dimensional, e.g. $\Gamma = (\gamma_1(r), \gamma_2(r))$, the condition

$$\left. \left(\frac{\partial F(\gamma_1, \gamma_2, \phi, p_1, p_2)}{\partial p_1}, \frac{\partial F(\gamma_1, \gamma_2, \phi, p_1, p_2)}{\partial p_2} \right) \right|_{s=r} \cdot (-\gamma_2, \gamma_1)\big|_{s=r} \neq 0 \tag{121}$$

is sufficient. In the latter case, we call the boundary data $(\Gamma, \phi, \psi_1, \psi_2)$ **noncharacteristic**. This condition can be generalized to $\nabla_{\mathbf{p}} F(\Gamma(\mathbf{r}), \phi, \mathbf{p}^0) \cdot N(\Gamma(\mathbf{r}))$, where $N(\Gamma(\mathbf{r}))$ is the normal vector to Γ [81, 82, 84].

It is theoretically possible to extend this framework to create a further reduction of the PDE. However, creating such a system of equations becomes significantly more complex than is needed for this thesis. See [85] for an example of such a higher order reduction.

5.2.4 Application to Zerilli Function

Having laid out the mathematical foundations of the method of lines and method of characteristics, we will now apply them to the Zerilli equation.
Let us first consider the Zerilli equation (82) in the context of the method of lines. At some time t and some $r_{*,j} = j\Delta r_*$, the Zerilli equation will become[8]

$$\frac{\partial^2 \psi}{\partial t^2} = \frac{\psi_{j+1}(t) - 2\psi_j(t) + \psi_{j-1}(t)}{\Delta r_*^2} + V(r_{*,j})\psi_j(t). \tag{122}$$

Using the finite difference method for the time derivative, we can rewrite equation (122) at $(t_i = i\tau, r_j)$ as

$$\frac{\psi_j(t_{i+1}) - 2\psi_j(t_i) + \psi_j(t_{i-1})}{\tau^2} = \frac{\psi_{j+1}(t_i) - 2\psi_j(t_i) + \psi_{j-1}(t_i)}{\Delta r_*^2} + V(r_j)\psi_j(t_i) \tag{123}$$

which implies

$$\psi_j(t_{i+1}) = 2\psi_j(t_i) - \psi_j(t_{i-1}) + \tau^2 \left[\frac{\psi_{j+1}(t_i) - 2\psi_j(t_i) + \psi_{j-1}(t_i)}{\Delta r_*^2} + V(r_j)\psi_j(t_i)\right]. \tag{124}$$

In this case the expression of ψ at the next time step is only dependent on the solution of previous time-steps. In the application of the method of lines we only consider ψ and do not track the derivatives. This could lead to inaccuracies at, for example, the boundary. To provide a more stable method we therefore apply the method of characteristicss. Including the derivatives of ψ also makes it possible for us to analyse and track quantities such as the total energy of the system.
Using the notation of Section 5.2.3, we have $u = \psi(r_*, t)$, $p_1 = \partial_{r_*}\psi$ and $p_2 = \partial_t \psi$. Using index notation similar as above and assume that we have the values of $p_1(r_*, t), p_2(r_*, t), u(r_*, t)$ on a specific time-slice $t = t_i$ we can define

$$\left.\frac{\partial p_1(r_*, t)}{\partial r_*}\right|_{r_*=r_{*,j}, t=t_i} = \frac{p_1(r_{*,j-1}, t_i) - p_1(r_{*,j+1}, t_i)}{2\Delta r_*} \tag{125a}$$

$$\left.\frac{\partial p_2(r_*, t)}{\partial r_*}\right|_{r_*=r_{*,j}, t=t_i} = \frac{p_2(r_{*,j-1}, t_i) - p_2(r_{*,j+1}, t_i)}{2\Delta r_*}. \tag{125b}$$

$$\left.\frac{\partial u(r_*, t)}{\partial r_*}\right|_{r_*=r_{*,j}, t=t_i} = \frac{u(r_{*,j-1}, t_i) - u(r_{*,j+1}, t_i)}{2\Delta r_*}, \tag{125c}$$

where we assume r_j is in the interior of the spatial domain $[r_{*,\min}, r_{*,\max}]$. If $r_{*,j} = r_{*,\min}$, we have that $p_1(r_{*,j-1}, t_i) \to p_1(r_{*,\min}, t_i)$ and $2\Delta r_* \to \Delta r_*$. The cases go analogously for $p_2(r_*, t)$ and $u(r_*, t)$, as well as for $r_{*,j} = r_{*,\max}$.
For the time-derivatives, we have

$$\left.\frac{\partial p_1(r_*, t)}{\partial t}\right|_{r_*=r_{*,j}, t=t_i} = \left.\frac{\partial p_2(r_*, t)}{\partial r_*}\right|_{r_*=r_{*,j}, t=t_i} \tag{126a}$$

$$\left.\frac{\partial p_2(r_*, t)}{\partial t}\right|_{r_*=r_{*,j}, t=t_i} = \left.\frac{\partial p_1(r_*, t)}{\partial r_*}\right|_{r_*=r_{*,j}, t=t_i} - V(r_{*,j})u(r_{*,j}, t) \tag{126b}$$

[8] Compared to Section 5.2.2, we omit the 1, in the subscript, since we only have one spatial dimension

$$\left.\frac{\partial u(r_*,t)}{\partial t}\right|_{r_*=r_{*,j},t=t_i} = p_2(r_{*,j},t_i), \tag{126c}$$

where we use, respectively, the definitions of p_i, the Zerilli equation and the fact that $u(r_*,t)$ is continuous and smooth in both variables.
Combining both methods, we get

$$p_2(r_{*,j},t_{i+1}) = p_2(r_{*,j},t_i) + \frac{c_{\mathrm{CFL}}}{2}\left[p_1(r_{*,j+1},t_i) - p_1(r_{*,j-1},t_i)\right] + \tau V(r_{*,j})u(r_{*,j},t_i), \tag{127a}$$

$$p_1(r_{*,j},t_{i+1}) = p_1(r_{*,j},t_i) + \frac{c_{\mathrm{CFL}}}{2}\left[p_2(r_{*,j+1},t_i) - p_2(r_{*,j-1},t_i)\right], \tag{127b}$$

$$u(r_{*,j},t_{i+1}) = u(r_{*,j},t_i) + c_{\mathrm{CFL}}\Delta r_* p_2(r_{*,j},t_i)(t_i), \tag{127c}$$

where the Courant-Friendricks-Lewy number is given by $c_{\mathrm{CFL}} = \frac{\tau}{\Delta r_*}$.

6 The code

The code that evolves the Zerilli function using the Zerilli equation is made in the coding language Julia. The foundations of the code have been made by Stamatis Vretinaris and have been extended on by Pjotr Koster. Details about the mathematical background of partial differential equations and details about the code can be found in Section 5. Tests of the code can be found in Section 7.

6.1 Implementing initial data

The initial data used for the Zerilli equation can be found in the file *InitialData.jl*. Since we use the method of characteristics, we work with the functions

$$\Phi_{\text{code}} = \psi \tag{128}$$

$$\Pi_{\text{code}} = \partial_t \Phi_{\text{code}} = \partial_t \psi \tag{129}$$

$$\Psi_{\text{code}} = \partial_{r_*} \Phi_{\text{code}} = \partial_r \psi \tag{130}$$

From now on, we omit the "code" from the subscripts.
This means that the Zerilli equation (82) becomes

$$-\frac{\partial \Pi}{\partial t} + \frac{\partial \Psi}{\partial r_*} - V(r)\Phi = 0. \tag{131}$$

In the code, we have opted for writing down the general forms of the initial data for Φ and Π, equations (87) and (89), respectively. This means that we have created separate functions for the metric coefficients. The functions for the initial data $\Phi(t, r, M, P, L, l)$ and $\Pi(t, r, M, P, L, l)$ are also dependent on the $l-$mode, so that the code can be used in other contexts. For $\Psi(t, r, M, P, L, l)$, we use the ForwardDiff package to safe computation time, meaning $\Psi(t, r) = \text{ForwardDiff.derivative}(r_1 \to \Phi(t, r_1, M, P, L, l), r)$. Using these functions, we create vectors of n_{cells} length with Float64 entries. These are combined into a matrix we call *statevector*, using the function *hcat()*.

6.2 The rhs! function

Since we use the method of characteristics and method of lines, the code needs to solve three first order Ordinary Differential equations. This is done using the Runge Kutta method, for which we need to program a function that approximates the time-derivative of the functions Φ, Π and Ψ at a time t_j and space $r_{*,i} = r_{*,\text{min}} + i\Delta r_*$. This is done by the rhs! function in the *ODE.jl* file.
The function rhs!(du :: $\mathit{AbstractArray}\{<: \mathit{Real}\}, U$ :: $\mathit{AbstractArray}\{<: \mathit{Real}\}$, params, t :: Real) outputs the different time-derivatives of the functions (128) -(130) at a specific time t in the abstract array du. The matrix U contains the arrays of Φ, Π and Ψ at a specific time t. From *params*, it uses the information about the number of (spatial) cells, the spacing, the mass, boundary type and the spatial domain. The t is not explicitly used, but will be used in the RK4 function. The real input is therefore from U and *params*. The parts in aquamarine are there to make sure that the input is correct, for example : *Real* ensures that the initial data is real and not complex.

6.2.1 Approximating spatial derivatives

Calculating the time-derivatives requires an approximation for the spatial derivatives at each spatial point, for which we use the finite difference method.

For each interior point $r_{*,i} = r_{*,\min} + i\Delta r_*$, we take

$$\partial_r \Phi(t_j, r_{*,i}) = dr\Phi = (\Phi[i+1] - \Phi[i-1])/2h \tag{132a}$$
$$\partial_r \Pi(t_j, r_{*,i}) = dr\Pi = (\Pi[i+1] - \Pi[i-1])/2h \tag{132b}$$
$$\partial_r \Psi(t_j, r_{*,i}) = dr\Psi = (\Psi[i+1] - \Psi[i-1])/2h, \tag{132c}$$

where the second equal sign shows how it is denoted in the code[9] and $h = \Delta r_*$.
For the boundaries in the spatial domain, one takes $i-1 \to 1$ and $i+1 \to 2$ with $2h \to h$, or $i-1 \to N-1$ and $i+1 \to N$ with $2h \to h$.[10] This implies that the approximations of the derivatives at the spatial boundaries are of first order, while the approximations are of the second order at the interior.

6.2.2 Approximating time derivatives

The time-derivatives for Φ, Π and Ψ are approximated via the definition of the characteristic functions, the Zerilli equation, and the radiative boundary and smoothness condition of the Zerilli function, respectively.
At the interior of the domain, the time derivatives of the functions (128) -(130) are given by

$$\partial_t \Phi(t_j, r_{*,i}) = dt\Phi[i] = \Pi[i] \tag{133a}$$
$$\partial_t \Pi(t_j, r_{*,i}) = dt\Pi[i] = dr\Psi - V(r_{*,i}, M)\Phi[i] \tag{133b}$$
$$\partial_t \Psi(t_j, r_{*,i}) = dt\Psi[i] = dr\Pi[i], \tag{133c}$$

where again the second equal sign shows how it is denoted in the code.[11] Equation (133a) follows from the definition of Π and therefore also holds at the spatial boundary points. Equation (133b) follows from the Zerilli equation. Equation (133c) follows from the fact that the Zerilli equation should be continuous and smooth in both variables, such that $\partial_t \partial_{r_*} \psi = \partial_{r_*} \partial_t \psi$.

Let us now consider the boundaries of our spatial domain. Solving a partial differential equation requires you to give boundary conditions at the beginning and end of your domain. The code allows for two boundary conditions, radiative or reflective.
In the case of the radiative boundary condition, we define the characteristic variables at the spatial boundary points

$$a = dr\Phi + dr\Psi \tag{134a}$$
$$b = dr\Phi - dr\Psi, \tag{134b}$$

where a from equation (134a) is called the out-coming characteristic variable and b from equation (134b) is called the in-coming characteristic variable. For radiative boundary condition at the last spatial point $r_{*,N}$, one sets $b \mapsto 0$, while at the first spatial point $r_{*,0}$, one sets $a \mapsto 0$. Afterwards, the primitive variables are defined as

$$dr\Phi = (a+b)/2 \tag{135a}$$
$$dr\Psi = (a-b)/2, \tag{135b}$$

which follow trivially from equations (134). The time-derivatives for Π and Ψ are then given by

$$dt\Pi[i] = dr\Psi \tag{136a}$$

[9] In the code, we calculate all of the above and below equation for each i, which is why the index i is nor included in f.e. $dr\Phi$.
[10] In the code we take $N1 = N - 1$ and uses *end* instead of N. For legibility, we have opted to try and stay consistent with the notation from Section 5.
[11] In this context, there is an i index, because the output are three different arrays bundled together.

$$dt\Psi[i] = dr\Pi. \tag{136b}$$

In the context of reflexive boundary conditions, one does not require characteristic variables to define the time-derivative at the spatial boundaries

$$dt\Pi[i] = 0 \tag{137a}$$
$$dt\Psi[i] = dr\Pi. \tag{137b}$$

After all the time-derivates are calculated, the arrays $dt\Phi, dt\Pi$ and $dt\Psi$ are bundled together into the matrix du using the *hcat()* function.

6.3 The RK4 function

Having found a way to approximate the time derivatives for each characteristic function, we need to create a function that solves the equations. We will use the Runge-Kutta method of fourth order.
In the code, solving the three Ordinary Differential Equations is done by the function $RK4(rhs! :: F, dt :: Real, \text{reg1}, \text{reg2}, \text{reg3}, \text{reg4}, params, t :: Real, indices :: CartesianIndices)$, which can be found in the *Integrator.jl* file. Here rhs! is the function as described in Section 6.2; dt is the time step;[12] reg$i$ are four different abstract arrays which will be used to make different (intermediate) approximations of the functions Φ, Π and Ψ, and $params$ and t are both used as input for $rhs!$.
The abstract array reg1 is used as input U in $rhs!$, meaning that it contains the information of Φ, Π, Ψ for a specific time. The abstract array reg4 is used as input du in $rhs!$, meaning that it contains the approximation for the time derivatives of Φ, Π, Ψ at a specific time. The other abstract arrays reg3 and reg2 are used as templates for different intermediate approximations. These approximations happen in four steps, each step is started by $rhs!(\text{reg4}, \text{reg1}, params, t)$.
In the first step, we take

$$\text{reg3}^1[i] = dt * \text{reg4}^1[i] = k_1, \tag{138a}$$
$$\text{reg2}^1[i] = \text{reg3}^1[i] = k_1. \tag{138b}$$

where i is a spatial index and the index 1 denotes which step it is defined in.[13] Using the notation of Section 5.1.1, we have $\text{reg3}^1[i] = k_1$, since $rhs!(\text{reg4}, \text{reg1}, params, t) = f(r_{*.i}, y_0)$ and $dt = h$.
In the second step, we have gotten a new approximation of the time derivatives in reg4^1 from inputting reg1^1 into $rhs!$. Similarly to before, we take

$$\text{reg3}^2[i] = dt * \text{reg4}^2[i] = k_2, \tag{139a}$$
$$\text{reg1}^2[i] = \text{reg1}^1[i] + (\text{reg3}^2[i] - \text{reg2}^1[i])/2 = y_0 + k_1/2 + (k_2 - k_1)/2 = y_0 + k_2/2. \tag{139b}$$

As we see from equation (139b), we have defined reg2^1 not to approximate the function, but rather to get the right input.
After implementing $rhs!$ again, we define

$$\text{reg3}^3[i] = dt * \text{reg4}^3[i] - \text{reg3}^2[i]/2 = dt * \left(\text{reg4}^3[i] - \text{reg4}^2[i]/2\right) = k_3 - k_2/2, \tag{140a}$$
$$\text{reg1}^3[i] = \text{reg1}^2[i] + \text{reg3}^3[i] = y_0 + k_2/2 + (k_3 - k_2/2) = y_0 + k3, \tag{140b}$$
$$\text{reg2}^3[i] = \text{reg2}^1[i]/6 - \text{reg3}^3[i] = k_1/6 - k_3 + k_2/2. \tag{140c}$$

[12] In the formulas about the theory behind solving differential equations, we also call this τ.
[13] These indices are not used in the code, but will be used here to show the chronology of the definitions and create more clarity.

After applying $rhs!$ for the last time, we take

$$\text{reg3}^4[i] = dt * \text{reg4}^4[i] + \text{reg3}^3[i] + \text{reg3}^3[i] = k_4 + 2 * (k_3 - k_2/2) = k_4 + 2k_3 - k_2, \tag{141a}$$

$$\text{reg1}^4[i] = \text{reg1}^3[i] + \text{reg2}^3[i] + \text{reg3}^4[i]/6 = y_0 + k_1/6 + k_4/6 + k_3/3 + k_2/3, \tag{141b}$$

where $\text{reg1}^4[i]$ from equation (141b) is the final approximation and coincides with the final approximation of the RK4 method, as seen in equation (102).

6.4 Running the code

The previously discussed functions are used to do the mathematical "dirty-work". There are other functions in the code that are used to create files with the solutions. For example, there is a function that creates the right path so the files get created in the right folder. These functions can be found in the *Integrator.jl* file, and we shall not discuss them in detail. Instead, we shall shortly discuss the *run_zerilli* function.
The run_zerilli function in the *Run.jl* file runs the code that produces the solution to the ODEs. The function run_zerilli($domain :: Vector, ncells :: Integer, tf :: Real, cfl :: Real, l :: Integer, M :: Real = 1.0, P :: Real = 1.0, L :: Real = 1; boundary\_type :: Symbol =: radiative, folder = "", save\_every = 1$) has as input *domain* the spatial domain for each time-slice, *ncells* the number of equally separated spatial points in the domain, tf the final time, cfl the Courant-Friedricks-Lewy number, l the multipole of the Zerilli function and potential, M the mass of the black holes, P the momentum of the black holes, L the distance separating the two black holes, *boundary_type* the boundary condition at the borders of the spatial domain, $folder$ the specific name added to the foldername and $safe\_every$ which determines if the solutions for all time slices gets saved (for example, if the value is two, only each second solution gets saved into the folder). When the words in aquamarine are followed by an equal sign and another symbol, the input is taken to be the symbol after the equal sign when no manual input was given.
The output of the function is a folder with an hf5 file for each time slice. Each hf5 file of the ith time slice contains the solution for Φ, Π and Ψ as well as the number of the file i. The function also outputs a text file which contains the meta data of the file, such as the input of *run_zerilli* function, the domain in r_*, the size of the steps dr_* and dt, other parameters needed for the initial data and the function for $dt\Pi[i]$ in the $rhs!$ function.
The initial data for Φ, Π and Ψ used for the run are therefore not inputs for the *run_zerilli* function. The functions are imported from the *InitialData.jl*-file and are part of the *run_zerilli* function. The *run_zerilli* function also creates a list called *params*, which contains information about the inputs that are also shown in the meta data file. As previous sections highlighted, this list is used for different functions in the code.

7 Validating the code

To verify the numerical solver, we have performed multiple tests to ensure the correctness of the solutions. These testst include checking the implementation of the coordinate transformation from r to $r_\star$, the ability for the code to solve other simpler or Schrödinger-like equations and confirming that the numerical convergence of the solution is of order $p = 2$.

7.1 Theoreritcal framework for validating the code

To verify the accracy of the data and the numerical solver, we need to check the convergence of the data. We use a finite step method to approximate the derivative of functions at later time. As shown in the *rhs*! function from Section 6, we have at the spatial boundaries (e.g. $r_* = r_{*,\min}$ and $r_* = r_{*,\max}$) approximations of the order $p = 1$. At the interior of the spatial domain, we have approximations of the order $p = 2$. At later times, lower order errors from the spatial boundaries propogates to the interior. When considering the numerical convergence of the solutions to the initial value problem, this error propogation must be taken into account.

7.1.1 Error functions

To check the order of convergence, we use the **Richard extrapolation**. Given a domain of the form $[r_{*,\min}, r_{*,\max}]$, we can cut the domain up into n_{cells}, leading to a resolution of $h = \frac{r_{*,\max}-r_{*,\min}}{n_{\text{cells}}}$. Suppose that $\psi_h(t, r_*)$ is the approximation of ψ at t, r_* with resolution h, if the approximation is of order p, we have

$$\psi_h(t, r_*) = \psi(r_*, t) + c_p h^p + c_{p+1} h^{p+1} + O\left(h^{p+1}\right) \tag{142}$$

$$\implies \psi_h(r_*, t) - \psi(t, r_*) = c_p h^p + c_{p+1} h^{p+1} + O\left(h^{p+1}\right), \tag{143}$$

where c_p is a constant and $\psi(r_*, t)$ is the analytical solution. If one would take a smaller resolution, say $h/2$, it is clear that equation (142) becomes

$$\psi_{h/2}(t, r_*) = \psi(r_*, t) + c_p \left(\frac{h}{2}\right)^p + c_{p+1} \left(\frac{h}{2}\right)^{p+1} + O\left(h^{p+1}\right) \tag{144}$$

Using equations (143) and (144), we can define "error functions"

$$\psi_h(t, r_*) - \psi_{h/2}(t, r_*) = c_p \left[h^p + \left(\frac{h}{2}\right)^p\right] + c_{p+1} \left[h^{p+1} + \left(\frac{h}{2}\right)^{p+1}\right] + O\left(h^{p+1}\right) \tag{145}$$

$$\psi_{h/2}(r_*, t) - \psi_{h/4}(t, r_*) = c_p \left[\left(\frac{h}{2}\right)^p + \left(\frac{h}{4}\right)^p\right] + c_{p+1} \left[\left(\frac{h}{2}\right)^{p+1} + \left(\frac{h}{4}\right)^{p+1}\right] + O\left(h^{p+1}\right), \tag{146}$$

where we call equation (145) the first error function and equation (146) the second error function. Using these error functions (145) and (146), the order of convergence can be determined for the code via

$$\begin{aligned}\frac{\psi_h(t, r_*) - \psi_{h/2}(t, r_*)}{\psi_{h/2}(t, r_*) - \psi_{h/4}(t, r_*)} &= \frac{c_p h^p - c_p \left(\frac{h}{2}\right)^p + O\left(h^{p+1}\right)}{c_p \left(\frac{h}{2}\right)^p - c_p \left(\frac{h}{4}\right)^p + O\left(h^{p+1}\right)} \\ &= \frac{1 - \left(\frac{1}{2}\right)^p + O(h)}{\left(\frac{1}{2}\right)^p - \left(\frac{1}{4}\right)^p + O(h)} = \frac{4^p - 2^p + O(h)}{2^p - 1 + O(h)} = \frac{2^p(2^p - 1) + O(h)}{2^p - 1 + O(h)} = 2^p + O(h).\end{aligned} \tag{147}$$

One therefore can find the order of convergence by

$$p = \log_2 \left[\frac{\psi_h(t, r_*) - \psi_{h/2}(t, r_*)}{\psi_{h/2}(t, r_*) - \psi_{h/4}(t, r_*)} \right]. \tag{148}$$

When creating data-sets, we can calculate the order of convergence at each point. However, it will be more useful to consider the L_2-norm of the datasets. This means that for a timeslice at t, we consider

$$\|\psi_h(t, r_*) - \psi_{h/2}(t, r_*)\| = \sqrt{\sum_{i=0}^{n_{\text{cells}}} \left|\psi_h(t, r_{*,i}) - \psi_{h/2}(t, r_{*,i})\right|^2}, \tag{149}$$

where $r_{*,i} = r_{*,\min} + ih$. Equation (149) can be used to give us an averaged order of convergence.

7.1.2 Total energy of the system

Analysing the total energy of the system is a robust way to check whether the method is numerically stable. In the case of radiative boundary conditions, the expactation is that the total energy of the system remains constant or monotonically decreases. The energy is expected to monotonically decrease when the pulse starts to leave the spatial domain.

The energy of a system described by a function $\phi(t, r)$ is given by

$$E = \int_{r_{*,\min}}^{r_{*,\max}} dr_* \left(\partial_t \phi(t, r_*)\right)^2 + \left(\partial_{r_*} \phi(t, r_*)\right)^2 + V(r_*)\phi(t, r_*)^2, \tag{150}$$

where $[r_{*,\min}, r_{*,\max}]$ is the spatial domain, $\phi(t, r_*)$ is the function of the system and $V(r_*)$ is the potential of the system.

7.2 Code for validation

As we have seen in Section 7.1, there are multiple ways to check the validness the code. In this section, we will discuss how we have implemented the theory to our datasets.

Firstly, the evolution of the total energy of the system can be checked by creating a function that takes as input the data, potential and an nd-array r of the spatial domain. The function is of the form

$$E_{code} = \frac{\Pi[0]^2 + \Psi[0]^2 + V(r[0])\Phi[0]^2 + \Pi[n]^2 + \Psi[n]^2 + V(r[-1])\Phi[n]^2}{2} + \sum_{i=1}^{n-1} \Pi[i]^2 + \Psi[i]^2 + V(r[i])\Phi[i]^2, \tag{151}$$

where n is the resolution of the data and r is an ndarray of the spatial domain consisting of n total equidistant steps. The factor $1/2$ for the boundary points in equation (151) comes from the fact that the approximations here are of first order, whereas they are of second order inside the domain. Using this function, it is possible to plot the energy as function of time and analyse its behaviour. This test is what we call the **energy check**.

Secondly, it is possible to check the convergence by consider the ratio between the two norms of the error functions

$$\frac{\|\psi_h(t, r_*) - \psi_{h/2}(t, r_*)\|}{\|\psi_{h/2}(t, r_*) - \psi_{h/4}(t, r_*)\|} = \frac{\sqrt{\sum_{i=0}^{n_{\text{cells}}} \left|c_{p,i} \left[h^p + \left(\frac{h}{2}\right)^p\right]\right|^2}}{\sqrt{\sum_{i=0}^{n_{\text{cells}}} \left|c_{p,i} \left[\left(\frac{h}{2}\right)^p + \left(\frac{h}{4}\right)^p\right]\right|^2}}. \tag{152}$$

If the code is convergent up to a specific time, the fraction remains constant for that period of time. Afterwards, the difference between the aggregated errors for different resolutions becomes too large. Consequently, this method gives us a rough picture when the convergence stops. We call this the **fraction check**.
It is important to chose the right Courant-Friedricks-Lewy number and resolutions for the spatial domain, otherwise the fraction check is invalid. Consider equations (145) and (146) that were used in equation (152). Naturally, the difference between approximations $\psi_h, \psi_{h/2}$ and $\psi_{h/4}$ should be considered at the same points in time and space. This implies that for a specific value for t, we should consider each fourth point of the array for $\psi_{h/4}$ and each second point of the array for $\psi_{h/2}$, because the array for $\psi_{h/4}$ contans four times more points than the array for ψ_h. Similarly, we should take each second point of the array for $\psi_{h/2}$. However, one needs to take into the account that simply multiplying the index over which one iterates might not give the same points, since the code first divides up the grid and needs to round off. Therefore, one needs to pick the c_{CFL}, the spatial domain, n_{cells} and the time domain wisely. For this reason, we have chosen to take $c_{CFL} = 0.25$ and values of n_{cells} that are multiples of 100 or multiples of the length of the domain. For example, when the domain is $[-20, 20]$, we might consider $n_{\text{cells}} = 40, 80, 160$.
To get more information about the order of convergence at a specific time-slice, one can apply the L_2-norms of the error functions. Looking at the definition of the error functions (145) and (146), the two norms of the error functions should align if one errorfunction is rescaled with 2^p

$$\begin{aligned}
\|2^p(\psi_{h/2}(t,r_*) - \psi_{h/4}(t,r_*))\| &= \sqrt{\sum_{i=0}^{n_{\text{cells}}} \left|2^p(\psi_{h/2}(t,r_{*,i}) - \psi_{h/4}(t,r_{*,i}))\right|^2} \\
&= \sqrt{\sum_{i=0}^{n_{\text{cells}}} \left|2^p \left(c_{p,i}\left[\left(\frac{h}{2}\right)^p + \left(\frac{h}{4}\right)^p\right]\right)\right|^2} \\
&= \sqrt{\sum_{i=0}^{n_{\text{cells}}} \left|c_{p,i}\left[h^p + \left(\frac{h}{2}\right)^p\right]\right|^2} = \|\psi_h(t,r_*) - \psi_{h/2}(t,r_*)\|.
\end{aligned} \tag{153}$$

To check the convergence at a specific time-slice, we plot the norm of the first error function and a rescaled version of the second error function with different values of p. In the beginning, one should have $p = 2$ which then slowly becomes smaller as the errors at the boundary propagate into the interior of the spatial domain. This test is called the **errors scaling check**.
After considering where the aggregated errors start to differ, we fix t and analyse the errors pointwise. This can either be done by analysing the fraction from equation (147) or the rescaled versions of the error functions (145) and (146). This will tell us where in the spatial domain the problems from convergence come from. For example, say that for successive time slices one sees that the order of convergence drops on the left side of the spatial domain and this dropping slowly extends into the interior. The problem of convergence is then a consequence of using different order approximations at the boundary. However, if the problem of convergence comes from the place where the potential becomes non-zero, the problem is more likely to be caused by interactions with the potential. These tests we call the **pointwise convergence check**.
If the analytical solution to the PDE or ODE is known, it is possible to check whether the numerical solution aligns with the analytical solution. In the convergence checks, it is possible to use the difference between the analytical and numerical solutions $\psi_{\text{anal}}(t,r_*) - \psi_h(t,r_*)$ and $\psi_{\text{anal}}(t,r_*) - \psi_{h/2}(t,r_*)$ instead of the difference between numerical solutions with different resolutions from equations (145) and (146). These tests form the **analytical comparison check**.
Lastly, it is possible to consider the convergence of the data at specific spatial points. Examples include places near the spatial boundaries that can represent places near or far away from the horizon. As we

want to analyse the data for quasi-normal modes at the horizon and far away, it is important to know the convergence behaviour of the data at these points. The checks at these points consist of plotting, as a function of time, the fraction from equation (147) or rescaled versions of the error functions (145) and (146). These checks are called the **horizon** and **far away checks**.

7.3 Results from checks

This section will contain the results of some of the tests that have been performed on varying toy models. We will not go into detail about the exact details, they can be found in teh Jupyter Notebook in `https://github.com/PiortKosret/MasterThesisFinal.git`.

Before we can discuss the results, we will clarify the toy models we have considered. If a toy model uses exponential initial data, the values for the wave function is given by

$$\psi(t,r) = \left(e^{r-r_0} + e^{r_0-r}\right)\left(e^{t} + e^{-t}\right), \tag{154}$$

where the initial data in constructed by taking the respective derivatives and setting $t = 0$. Similarly, a Gaussian wave pulse is a function of the form

$$\psi(t,r) = e^{(r-r_0-t)^2/\sigma^2}, \tag{155}$$

where r_0 is the place of the peak and σ determines the spread of the pulse.

A simple wave equation is a PDE without a potential

$$\frac{\partial^2\psi}{\partial r^2} = \frac{\partial^2\psi}{\partial t^2}. \tag{156}$$

If the toy model has a potential, the PDE that is solved for is of the form

$$\frac{\partial^2\psi}{\partial r^2} - \frac{\partial^2\psi}{\partial t^2} - V(r)\psi = 0. \tag{157}$$

The gauge invariant potential refers to the potential from equation (83), which will be used to evolve the Zerilli function. The Pöschl-Teller potential refers to the potential from equation (160).

Implementing a coordinate change $r_* = f(r)$ means here that insted of r we solve for the tortoise coordinate r_* from equation (74). This means that the input of the spatial domain in defined for r_* and the PDE is solved for r_*. The PDE has the form

$$\frac{\partial^2\psi}{\partial r_*^2} - \frac{\partial^2\psi}{\partial t^2} - V\left(f^{-1}(r_*)\right)\psi = 0, \tag{158}$$

where $f^{-1}(r_*)$ is the inverse of the coordinate change. The potential and functions for the initial data $\psi|_{t=0}$ are still defined in r, since we calculated the initial data for the Zerilli function the same way. Therefore, to get the correct initial data which is used to solve equation (158), we make use of the inverse coordinate change.

The time-independent Pöschl-Teller equation is

$$-\frac{1}{2}\partial_r^2\psi(r) - V(r)\psi(r) = E\psi(r), \tag{159}$$

where the potential is given by

$$V(r) = \frac{\lambda(\lambda+1)}{2}\,\mathrm{sech}^2(r). \tag{160}$$

The solution to equation (159) therefore is

$$\psi(r) = P^{\mu}_{\lambda}\left[\tanh(r)\right], \tag{161}$$

where $E = \frac{-\mu^2}{2}$, with $\mu = 1, ..., \lambda$. The related time-dependent equation is given by

$$\begin{aligned} 0 &= -\frac{1}{2}\psi_2(t)\partial_r^2\psi_1(r) - V(r)\psi_1(r)\psi_2(t) + \psi_1(r)\partial_t^2\psi_2(t) \\ &= -\frac{1}{2}\psi_2(t)\partial_x^2\psi_1(r) - V(r)\psi_1(r)\psi_2(t) + \omega^2\psi_1(r)\psi_2(t) \\ &= \left[-\frac{1}{2}\partial_r^2\psi_1(r) - V(r)\psi_1(r) - E\psi_1(r)\right]\psi_2(t) = 0 \end{aligned} \tag{162}$$

Below is a list of a selection of the performed tests and their results. In all of the test it is assumed that at the spatial boundary radiative boundary hold. The data, code and plots can be found in `https://github.com/PiortKosret/MasterThesisFinal.git`.

Figure 7: Comparison of numerical and analytical solutions for Φ and Π that satisfy the simple wave equation with exponential initial data. The data is plotted as a function of r on the domain $[-20, 20]$. The timestamps related to the data is colour coded and flagged in the legend. The input for the solver is $c_{\mathrm{CFL}} = 0.3$, $n = 500$ and $r_0 = 5$.

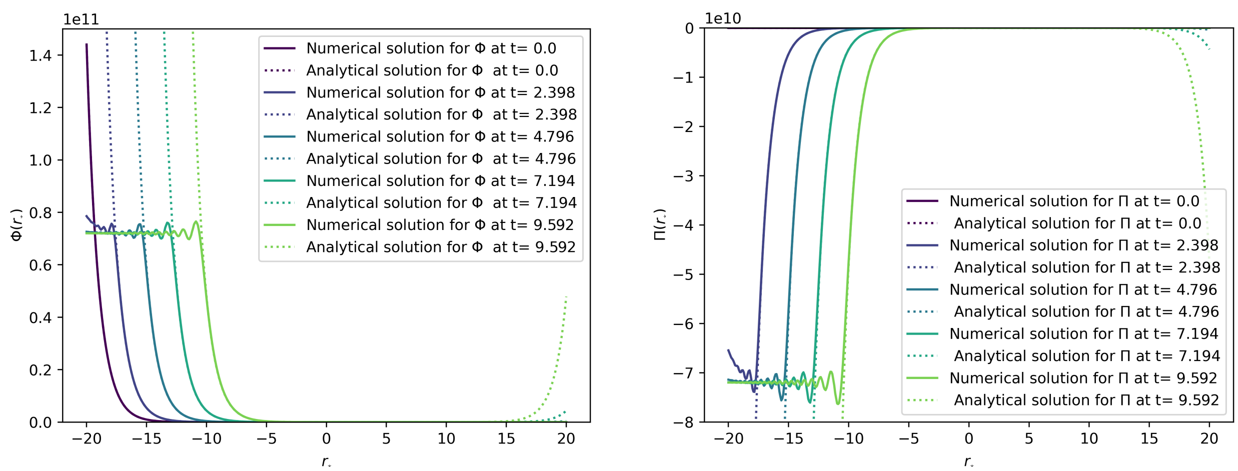

(a) Plot showing the numerical and analytical solution for Φ.

(b) Plot showing the numerical and analytical solution for Π.

- **Checking numerical solution for the simple wave equation with exponential initial data:** The data was solved in the domain $[-20, 20]$ with $n_{\mathrm{cells}} = 500$, $c_{\mathrm{CFL}} = 0.3$ and $r_0 = 5$. The numerical solutions for Φ, Π and Ψ overall fit the analytical solution. The only place where there is a discrepancy is near the left boundary point in the spatial domain, as one can see in Figure 7. This is because the initial data does not go to 0 at the boundaries. Note however that the numerical solution does not diverge at the boundary, but instead stays constant. This shows that the divergence we saw in Section

8 is not from the fact that the boundary value is non-zero, but rather something specific to the initial data.

- **Replicating data from other papers:** We were unable to recreate the same plots from [86] and [57]. After this attempt, other convergence/ solutions checks led us to change some code, particularly in the *InitialData.jl* file. With the updated code, the corresponding data could be generated and compared to the reference plots. However, due to time constraints, this has not been done yet.

- **Check numerical solution to time-independent Pöschl-Teller equation:** The data was solved on the domain $[-5, 5]$, with $n_{\text{cells}} = 500$, $c_{\text{CFL}} = 0.3$, $T = 10$ for $\lambda = 2$ with $\mu = 1, 2$. The numerical solution for Φ was consistent with the analytical solution. The solution also solved the equation (159).

- **Check numerical solution to time-dependent Pöschl-Teller equation:** The data was solved for the domains $[-1, 1], [-3, 3][-5, 5]$ in x, with $n_{\text{cells}} = 500$, $c_{\text{CFL}} = 0.3$, $T = 10$ for $\lambda = 2$ with $\mu = 1, 2$. The numerical solution agrees with the initial data and solves equation (162). The plot shows convergence of $p = 2$, which decreases over time with speeds depending on the spatial domains. When the domain is larger, the boundary values are closer to zero leading to a slower decrease of convergence, since the deviance from the required boundary conditions becomes smaller.

- **Convergence check for the simple wave equation and Gaussian pulse**: successfully passed the fraction check, errors scaling check and pointwise convergence check when comparing numerical data. When comparing to the analytical result, the data also passes the fraction check and errors scaling check. Problems with convergence are due to the pulse leaving the domain to the right, which lead to difference in errors at the right end of the domain. The energy check was unsuccessful, since the energy decreases non-monotonically. Convergence check at the horizon shows that the order of convergence starts at $p = 2$ which decreases quickly, because the error of the left boundary reaches the point near the horizon quickly. At far away, the order of convergence starts at $p = 1$ and later on start to increase in value. This result is counterintuitive, but can be written up to the pulse leaving the domain at later times, leading to error functions having higher values and differences.

- **Convergence check for the simple wave equation and Gaussian pulse with coordinate transformation**: successfully passed the fraction check, errors scaling check and pointwise convergence check. Problems with convergence are due to the pulse leaving the domain to the right, which lead to difference in errors at the right end of the domain. This happens earlier than in the previous check, because the spatial domain in r is smaller than before due to the coordinate change. The energy check was unsuccessful, since the energy both increases and decreases non-monotonically. The behaviour near the horizon and far away is similar to the previous test.

- **Convergence check for the wave equation with gauge invariant potential and Gaussian pulse**: successfully passed the errors scaling check and pointwise convergence check. Problems with convergence are due to a small difference in the error functions at $t = 0.25$ at the right end of the spatial boundary, which propagates to the left into the interior of the spatial domain. The energy test failed, since the energy does not monotonically decrease. At the horizon, the convergence is of order 2, which changes only very little. Far away, the convergence is of order 1, which might be a consequence of the asymmetry of the potential when expressed in r.

- **Convergence check for the wave equation with gauge invariant potential, Gaussian pulse and coordinate change**: successfully passed the errors scaling check and pointwise convergence check. Problems with convergence are due to a small difference in the error functions in the beginning at the right end of the spatial boundary, which propagates to the left into the interior of the spatial domain.

The energy test failed, since the energy does not monotonically decrease. The behaviour at the boundary and far away is similar to the previous test.

- **Convergence check for the wave equation with Pöschl-Teller potential and Gaussian pulse**: this convergent test was successful when the potential had the opposite sign of the potential from equation (160). If the potential had the same sign as in equation (160), the code diverges and passes no testx. The following checks are done for the potential with the opposite sign of equation (160). We created datasets where the potential had different scaling factors, meaning we multiply the potential by $1/n_{\text{scaling}}$. The larger the value for n_{scaling}, the smaller the potential. If n_{scaling} increases, the amplitude of the wave after it passes the potential increases. The smaller the value of n_{scaling}, the more the pulse reflects. When doing the fraction check and error scaling check, the convergence order starts at 2 and falls of quicker the higher the value of n_{scaling} is taken, see Figure 8 and 9. Performing the pointwise convergence check shows that the errors come from the interaction between the data and the potential. The energy test failed, since the value of the energy increases and decreases.

- **Convergence check for solving the Zerilli equation with initial data from Section 3**: Besides the results found in Section 8, the fraction shows a roughly consistent order of convergence until $t = 120$. Pointwise error checks at $t = 20$ show that problems with convergence follows from large difference between the numerical solutions in the beginning of the spatial domain, around $r_* = [0, 10]$, as well as larger differences between the numerical solutions after the wave reached the potential peak, around $r_* = [50, 70]$.

- **Convergence check for solving Zerilli equation with flipped sign of the potential and initial data from Section 3**: [14] Basic plotting of the data shows a divergence when Φ reaches the potential. Errors scaling check shows there is no convergence, even at early times. The norm of the errors grows exponential over time. Pointwise convergence checks show error plots similar to the ones in Section 8 at early times. The ratio test also shows consistent order of convergence until $t = 70$, but the ratio decreases for Φ and Π (which is unexpected, as this would mean that p would increase after $t = 70$) while increases for Ψ (which is expected). Pointwise convergence check around $t = 70$ shows that the main problem with convergence is no longer the left boundary point, but rather the interaction between Φ and the potential at around $r_* = 0$. The energy check fails, as it exponentially grows. Horizon and far away check both show an exponential decrease of Φ at late times.

[14] The reason for including this test is that previous tests showed that sometimes, having a different sign for the potential leads to a large divergence of the data when it reaches the potential. To see whether the effects came from the potential having the wrong sign, we checked the case where the potential from equation (83) had a minus sign.

Figure 8: Plot showing the errors scaling check for the wave equation with Pöschl-Teller potential and Gaussian pulse. The scaling factor is $n_{\mathrm{sc}} = 1$.The data is plotted as a function of t on the domain $[0, 50]$. The timestamps related to the data is colour coded and flagged in the legend. The input for the solver is $c_{\mathrm{CFL}} = 0.25$, $n = 80$, $r_0 = -15, sigma = 6$ and the domain in r is $[-40, 40]$.

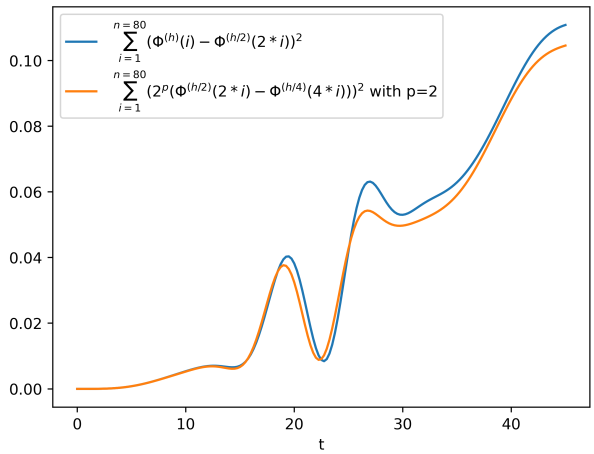

(a) Plot showing the errors scaling check for Φ s a function of t on the domain $[0, 50]$.

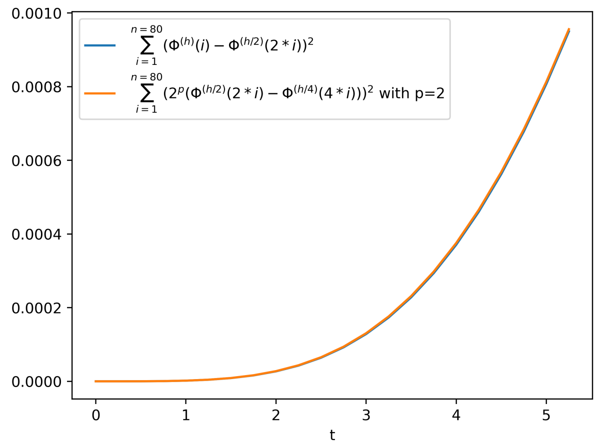

(b) Similar plot to Figure 8a, but now zoomed into the domain $t = [0, 15]$.

Figure 9: Similar plot to Figure 9a, but now with scaling factor $n_{\mathrm{sc}} = 20$.

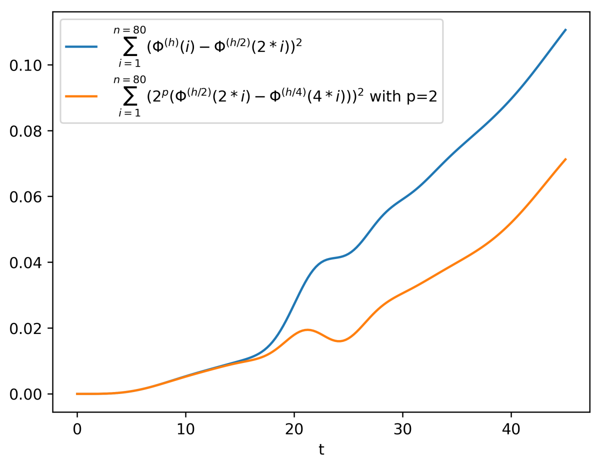

(a) Plot showing the errors scaling check for Φ s a function of t on the domain $[0, 50]$.

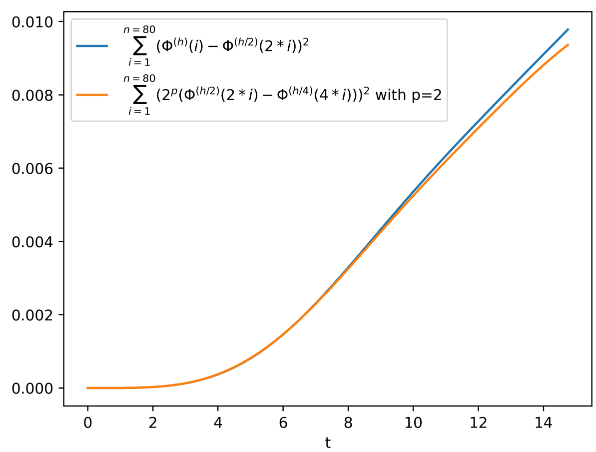

(b) Similar plot to Figure 7a, but now zoomed into the domain $t = [0, 15]$.

8 Results

The main objective of this thesis is to evolve the initial data for $t = 0$ by using the code and the Zerilli function. A part of the signal will propagate into the black hole, while the remainder of the signal will propagate to infinity. This study aims to compare the data, in particularly the quasi-normal modes, near the horizon and far away. The analysis of the data, such as the checking of convergence and the total energy, are performed using python and can be found in the Jupyter Notebook in `https://github.com/PiortKosret/MasterThesisFinal.git`. The analysis of quasi-normal modes is done in the Wolfram Mathematica file.
The initial data and numerical implementation described above did not produce physically meaningful results. Several modifications, such as changing the spatial domain considered, changing the sign of the potential and heavily increasing the resolution, have not yielded any improvements. From the tests in Section 7, it follows that the numerical solver is working well enough. In this section, we will explain what our input is, analyse the numerical solution, present convergence and stability tests, and give a conjecture on the cause of the issues. See Figure 10 for a flowchart for checking the results.
In the sections below, we use quantities such as r_* and t in plots that are not dimensionless. However, since we set $M = 1$, renormalising does not change the plots or analysis below. The factors of M can be inserted back by checking the dimensions of the quantities.

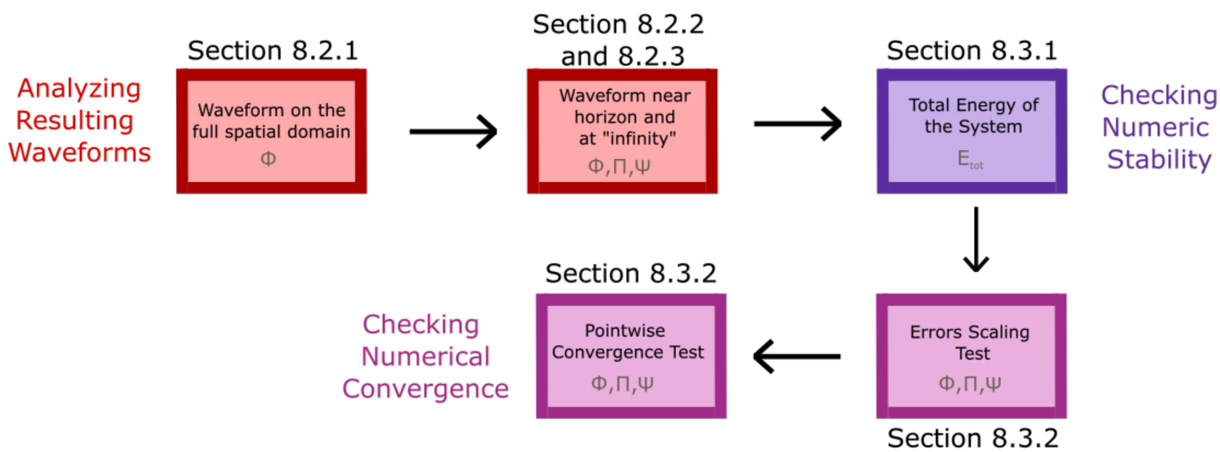

Figure 10: Flowchart showing the breakdown of this section. The first step consists of analysing the numerical solution for Φ on the whole spatial domain, and Φ, Π and Ψ near the horizon and far away from the horizon. This step is colourcoded red in the flowchart. The second step consists of checking the numeric stability of the solution by plotting the total energy of the system and is colourcoded purple. The last step consists of checking numerical convergence of Φ, Π and Ψ, and is colcourded pink.

8.1 Input

The initial data are functions called $InitialPsiValues, dtInitialPsiValues$ and $drInitialPsiValues$ for Φ, Π and Ψ, respectively. They can be found in the *InitidalData.jl* file. The black holes parameters are $M = 1, P = 1, L = 1, l = 2$ throughout this section. The spatial domain is $[-70, 130]$ in r_*, which is approximately equivalent to $[2.00, 121.81]$ in r. It is not possible to take values more negative than -75 in

r_*, because the code can not handle values so close to the horizon.[15] Since there is a unit propagation speed for Φ, Π and Ψ, the final time is taken to be 305 to ensure sufficient time for a pulse near the horizon to propagate to the end of the spatial domain. The Courant–Friedrichs–Lewy is set to $c_{\text{CFL}} = 0.25$ in order to get time-steps dt that can be written as terminating decimals, e.g. $dt = 0.25$. Simulations were performed for the set of resolutions $\{n = 100, n = 200, n = 400, n = 800, n = 1000\}$. The first four resolutions are used to analyse the convergence of the code, while the last resolution is taken to show the general behaviour of the solution. These simulations have, respectively, spatial steps dr of size $\{2, 1, 0.5, 0.25, 0.2\}$ and time-steps dt of $\{0.5, 0.25, 0.125, 0.0675, 0.05\}$.

8.2 Results

In this Section, we will first discuss how the initial data evolves over time by looking at plots which show the data Φ, Π and Ψ at different times. Afterwards, we discuss the data near the horizon and at asymptotic distances.

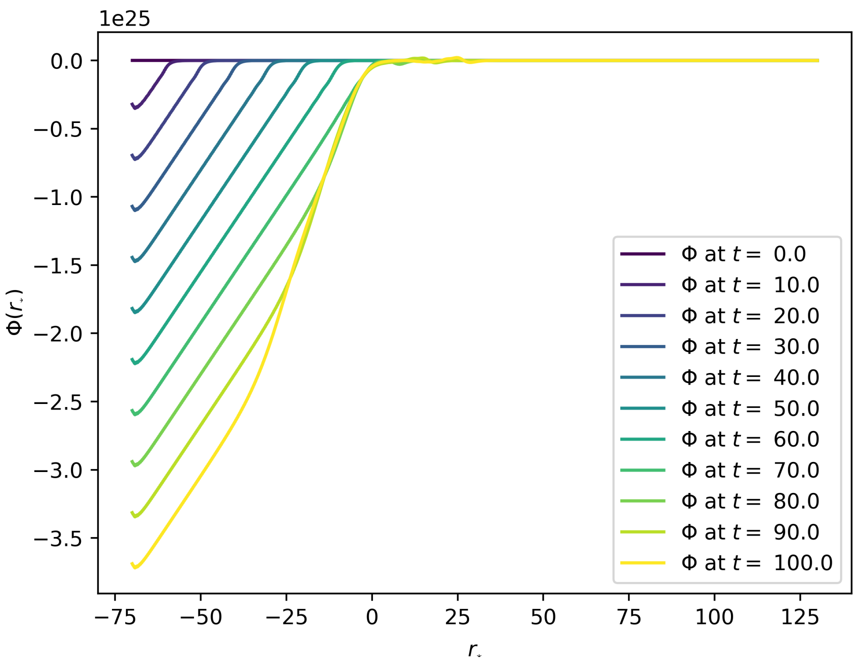

Figure 11: Plot showing the data for Φ from equation (87) with initial data from Section 3.2.3. The data shown goes up to $t = 100$ and is plotted as a function of r_*. The times related to the data are colour coded and marked in the legend. The resolution is $n = 1000$.

8.2.1 Overall features of the data

To discuss the overall feature that Φ displays over time, we analyse the data with the resolution $n = 1000$. Figures 11 and 12 show that Φ diverges near the horizon, becoming increasingly negative until around $t = 140$, after which the data stays at around $-5 * 10^{25}$ near the horizon. The data reaches the global minimum near $r_* = -70$, after which it linearly increases to 0, until around $t = 70$. At $t = 70$ the incline at approximately $r_* = -10$ gets a kink after which the data for Φ shows a greater incline. As t increases, the location of the

[15] One of the safety precautions taken in the code is to assert that $r > 2M$ in the *rhs!* function. Taking values smaller than -75 means that the code rounds the value of r down to $2M$, leading to an error.

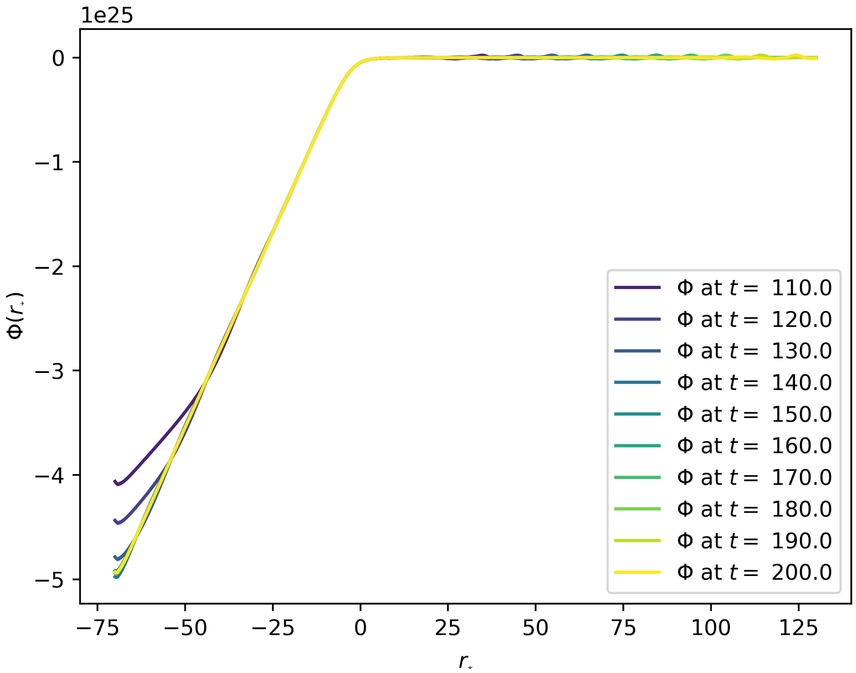

Figure 12: Plot showing the data for Φ from equation (87) with initial data from Section 3.2.3. The data shown are between $t = 100$ and $t = 200$ and is plotted as a function of r_*. The times related to the data are colour coded and marked in the legend.

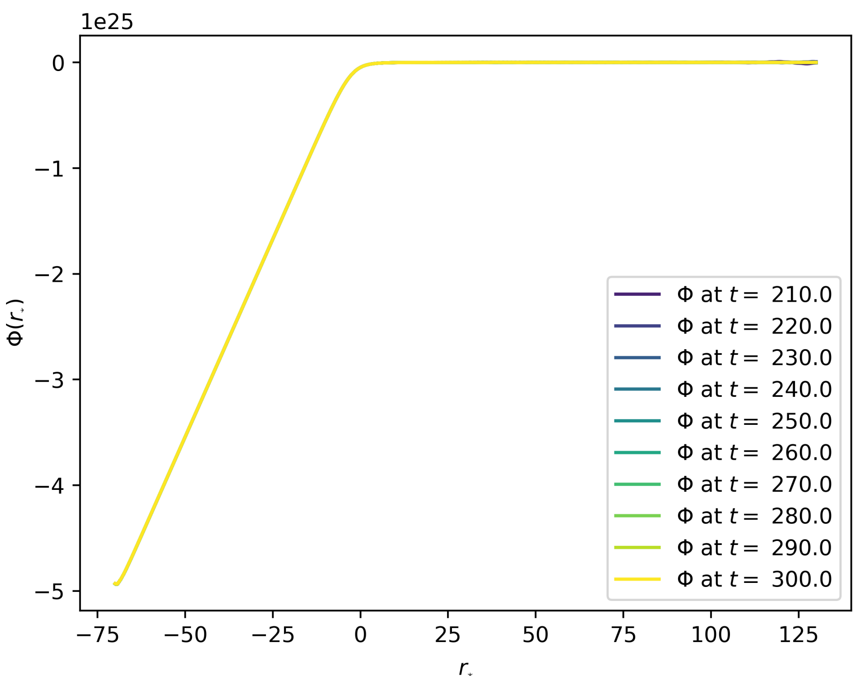

Figure 13: Plot showing the data for Φ from equation (87) with initial data from Section 3.2.3. The data shown is between $t = 200$ and $t = 300$ and is plotted as a function of r_*. The times related to the data are colour coded and marked in the legend.

kink shifts to more negative values of r_*. After $t = 140$, the kink has reached the left boundary. After $t = 140$ the overall chape of the data at the beginning of the spatial domain stays the same, as shown in Figures 12 and 13.

Figure 11 shows that the propagation of the function changes significantly at around $r_* = 0$, which is where the potential has its peak, as can be seen in Figure 6. The data for Φ after this point does not seem to change on the same level as before. From Figure 11 we see that at around $t = 70$, the form of the function changes when it reaches around $r_* = -10$, which is near where the potential starts to become non-negative. The creation of the kink may be attributed to an interaction of the data with the potential: the potential causes a reflection of the data. However, it should be noted that the potential is much smaller than the data, as Figure 6 shows: the peak of potential is of the order 10^{-3}.

Looking at Figures 12 and 13, we see that Φ does not stay constant after it reaches $r_* = 0$, as there are small bumps visible. This behaviour of Φ is more clearly illustrated in Figures 14 and 15. The data exhibits pulse-like behaviour fom $r_* = 0$ to the end of the spatial domain $r_* = 130$. At a fixed spatial coordinate, the data exihibits dampened oscillatory behaviour, which is consistent with data containing quasi-normal modes. However, as we will see in Section 8.2.3, this oscillatory behaviour is heavily dependent on the resolution of the data.

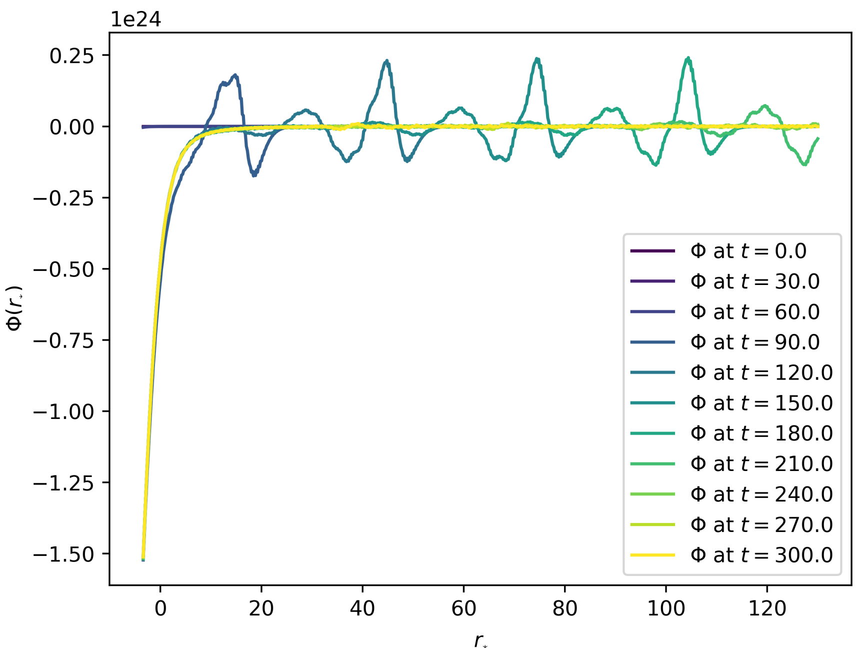

Figure 14: Plot showing the data for Φ from equation (87) with initial data from Section 3.2.3. The data is plotted as a function of r_* and is limited to the domain $[0, 130]$. The times related to the data are colour coded and marked in the legend.

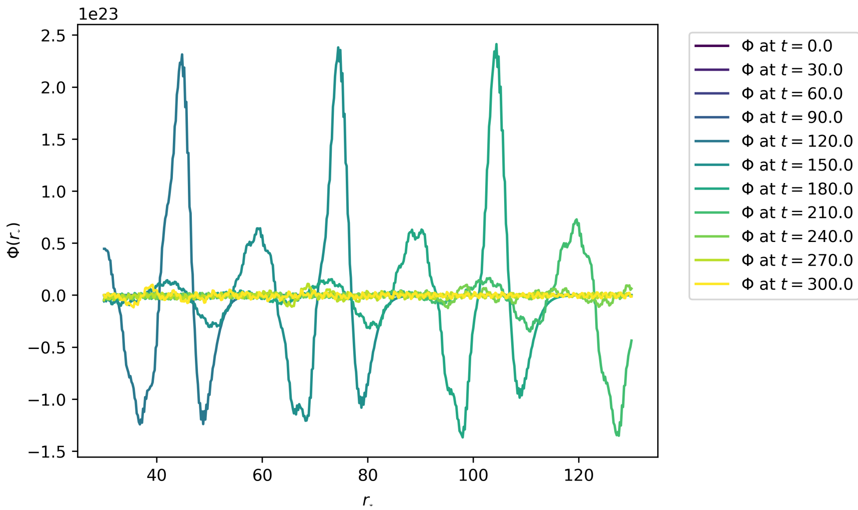

Figure 15: Plot showing the data for Φ from equation (87) with initial data from Section 3.2.3. The data is plotted as a function of r_* and is limited to the domain $[40, 130]$. The times related to the data are colour coded and marked in the legend.

Figure 16: Plots showing the data for Φ from equation (87) with initial data from Section 3.2.3 with different resolutions. The data is plotted as a function of r_* and is limited to the domain $[-70, 50]$. The resolutions related to the data are colour coded and marked in the legend.

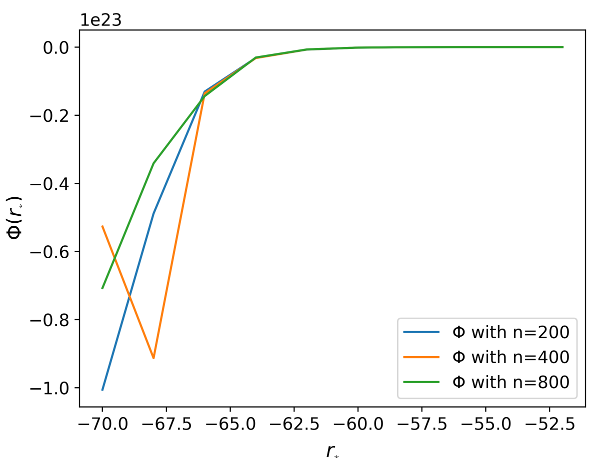

(a) Plot showing the data for Φ with different resolutions at $t = 0.5$.

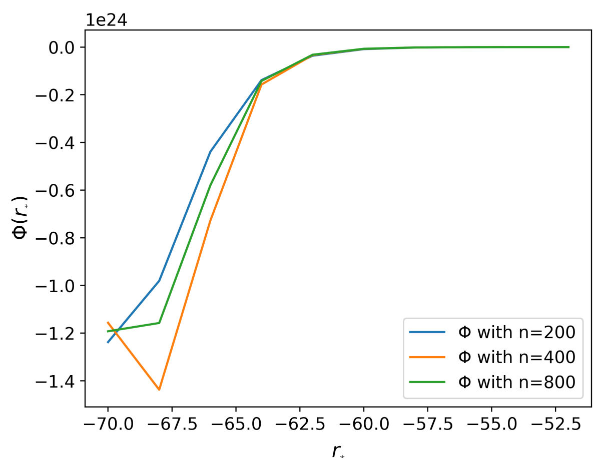

(b) Plot showing the data for Φ with different resolutions at $t = 4.0$. Note that the order of magnitude of the y-axis has increased by a factor of 10.

8.2.2 Near the horizon

In this section, we analyse the data near the horizon at the domain $[-70, -50]$ in r_* and at the point $r_* = -62$ (or equivalently $r = 2.0000000000000253$).
The results on the domain $[-70, -50]$ are strongly dependent on the resolution of the data, because the

approximation of the spatial derivative is at first order here. Due to the large magnitudes of Φ, the difference between the values of Φ for different resolutions are large at early times. The values do agree more at points further in the spatial domain, as shown in Figure 16a and 16b. At early times, the error caused by the difference between the orders of the approximation (first order at the boundary and second order in the interior), has not yet reached these further points. The spatial coordinate where the different data for Φ agrees more, increases over time. From the Jupyter Notebook file, one can see that this propagation at early times is linear and happens with speed 1.
To analyse the behaviour near the left boundary, we focus on the fourth spatial grid when the resolution is $n = 800$, which is equivalent to $r_* = -62$. As displayed in Figure 17, the values of Φ decreases linearly until around $-5 * 10^{25}$. This happens until $t = 140$, when the global minimum is reached. The values for Φ slightly increase until a local maximum is reached at approximately $t = 150$. Afterwards, the values decrease slightly and stay approximately on the domain $[160, 305]$. The overall form of the data is independent of the resolution, as shown in the Jupyter Notebook. The values for Π and Ψ are smaller than Φ, but still large, since they are of the order 10^{23}.

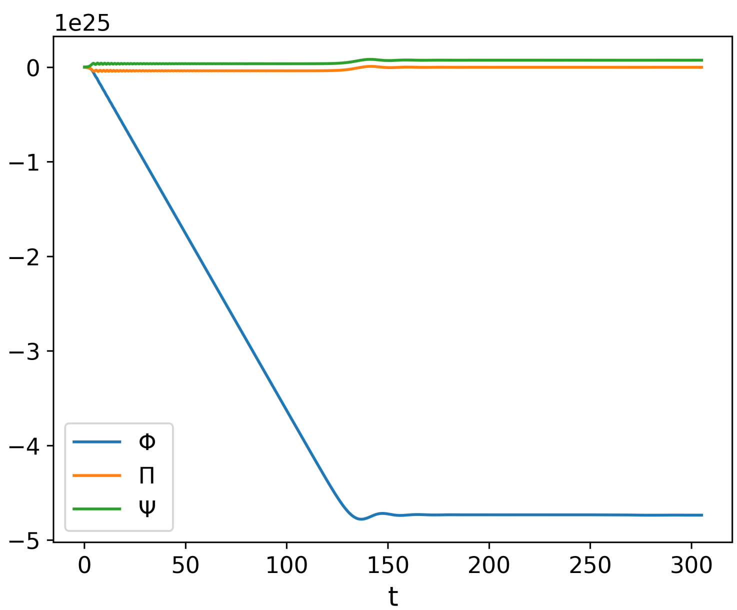

Figure 17: Plot showing the data for Φ from equation (87), Π from equation (89) and Ψ from equation (130) as a function of t at $r_* = -62$. The different datasets are colour coded and marked in the legend. The resolution is $n = 800$.

The behaviour of Π and Ψ is more clearly visible in Figures 18a and 18b. The values for Ψ increase until $t = 10$, after which the data exhibits dampened oscillatory behaviour with small amplitudes until $t = 110$. Afterwards, the data increases again until $t = 140$. This gets followed by oscillatory dampened behaviour until $t = 305$. The overall form of Π is approximately the same as the overall form of Ψ. However, in the first part, the data for Π decreases instead of increases. The characteristics of the oscillatory behaviour of the data, such as the frequency, amplitude, and damping, are dependent on the resolution. As illustrated in Figures 18a and 18b, if the data has a higher resolution, the frequency is larger and the domain of the behaviour is longer. This shows that this behaviour is not a characteristic of the solution, but rather an artefact of the code or initial data. The oscillatory behaviour of Π and Ψ does influence the shape of Φ on a smaller level by making the decrease less linear and more oscillatory, as shown in Figures 19a and 19b. However, it does not change the overall shape, as seen in Figure 17.

Figure 18: Plots showing the data for Π from equation (89) and Ψ from equation (130) near the horizon at $r_* = -62$ as a function of t on the domain $[0, 300]$. The different functions are colour coded and marked in the legend.

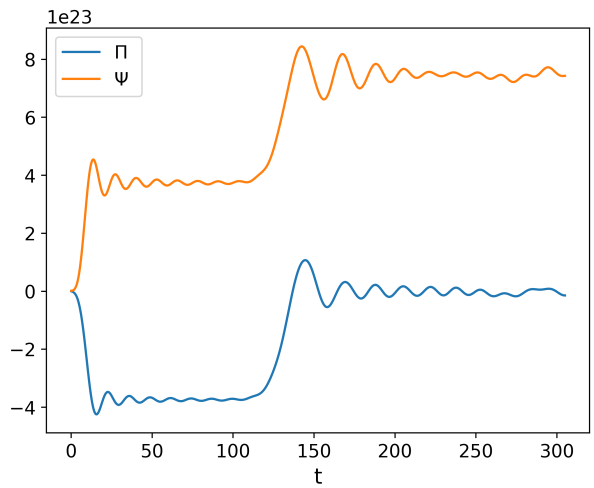

(a) Plot showing the data for Π and Ψ with resolution $n = 100$.

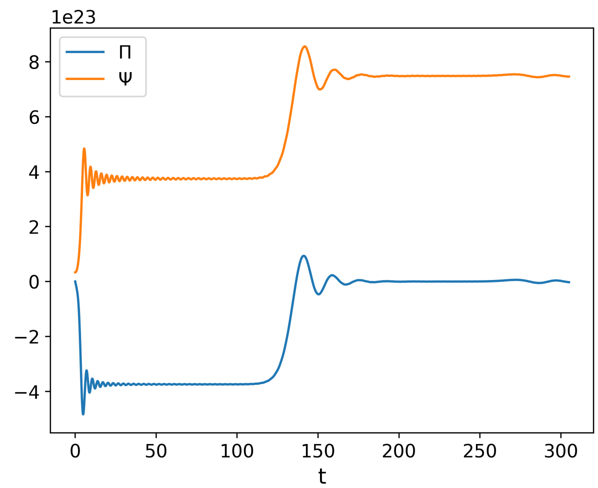

(b) Plot showing the data for Π and Ψ with resolution $n = 400$.

When we focus on specific parts of the time-domain, such as $[0, 10]$ in Figures 19a and 19b, and $[200, 300]$ in Figures 20a and 20b, we see that the results of Φ are strongly dependent on the resolution. Changes in the data include whether the function shows oscillatory behaviour, to what extent these are dampened, whether the function overall increases or decreases, the smoothness of the function and more. The overall shape of the function is also dependent on the resolution: Figure 19a shows that Φ decreases exponentially at the end if $n = 100$, while Figure 19b shows that Φ decreases while showing oscillatory behaviour if $n = 400$. This shows that there is clearly no convergence. Looking at Figures 18a and 18b, we can see that this behaviour at late times is mostly determined by the values of Ψ, since they are a lot larger than the values for Π in this part of the late domain.

Figure 19: Plots showing the data for Φ from equation (87), Π from equation (89) and Ψ from equation (130) at $r_* = -62$ as a function of t on the domain $[0, 10]$. The different functions are colour coded and marked in the legend.

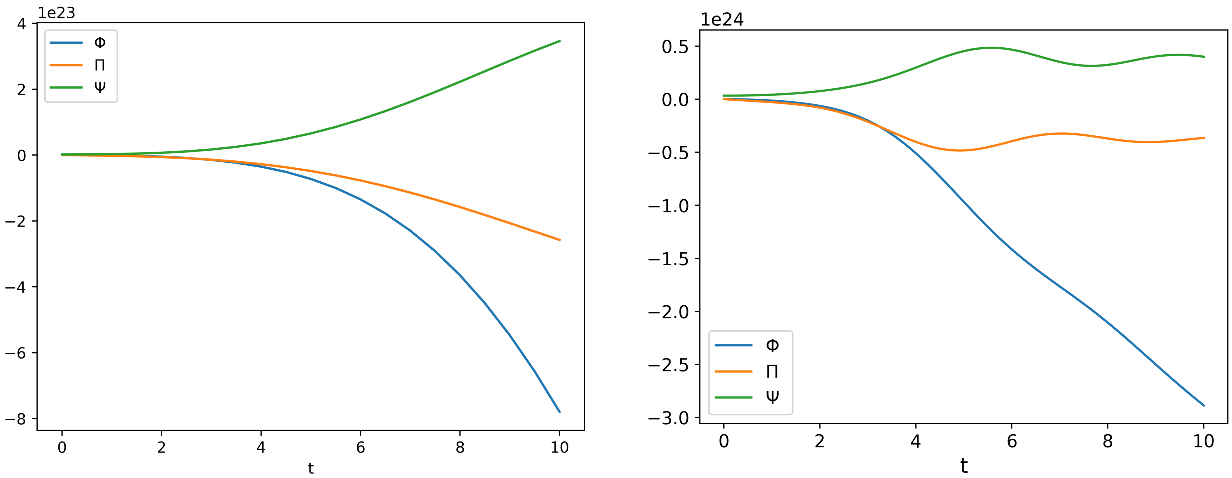

(a) Plot showing the data for Φ , Π and Ψ with resolution $n = 100$.

(b) Plot showing the data for Φ , Π and Ψ with resolution $n = 400$.

Figure 20: Plots showing the data for Φ from equation (87) near the horizon at $r_* = -62$ as a function of t on the domain $[200, 300]$.

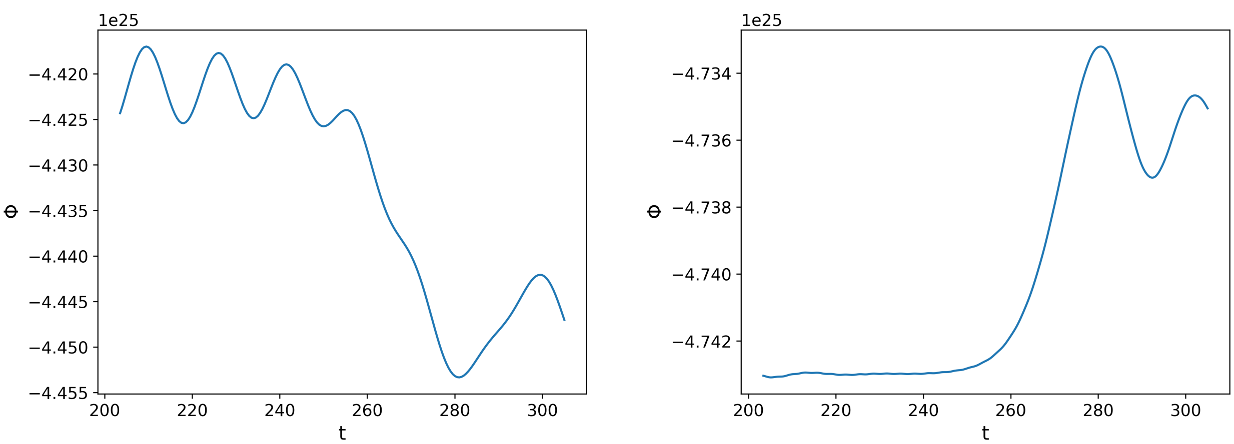

(a) Plot showing the data for Φ with resolution $n = 100$.

(b) Plot showing the data for Φ with resolution $n = 400$.

8.2.3 Far away

We now examine the overall form, and the behaviour at early and late time of the data near the end of the spatial domain. The point we are considering is $r_* = 124$, which is approximately equivalent to $r = 115.92$.

Figure 21: Plots showing the data for Φ from equation (87), Π from equation (89) and Ψ from equation (130) with different resolutions at $r_* = 124$ as a function of t on the domain $[0, 300]$. The different datasets are colour coded and marked in the legend.

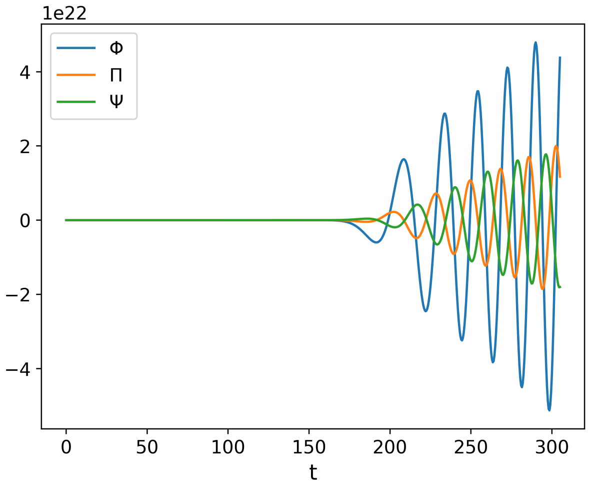

(a) Plot showing the data for Φ , Π and Ψ with resolution $n = 100$.

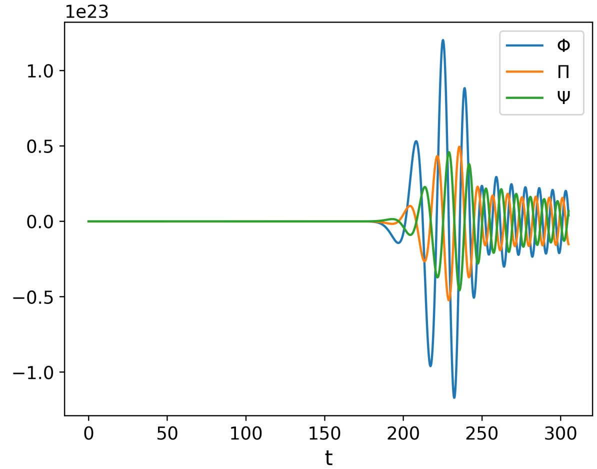

(b) Plot showing the data for Φ , Π and Ψ with resolution $n = 200$.

Figure 22: Similar plots to Figure 21.

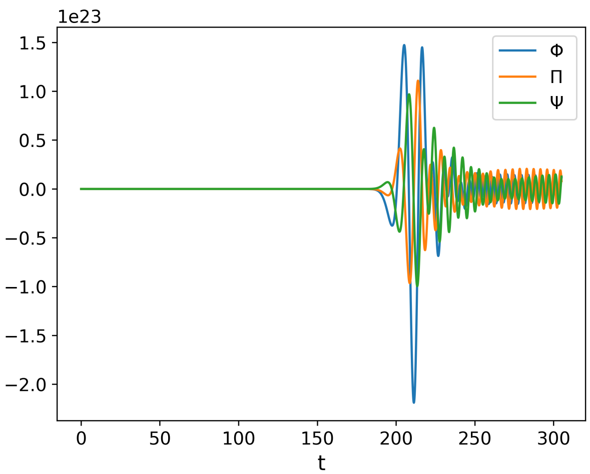

(a) Plot showing the data for Φ , Π and Ψ with resolution $n = 400$.

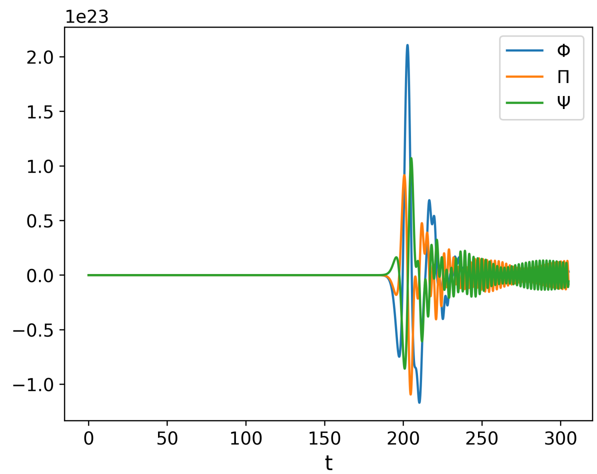

(b) Plot showing the data for Φ , Π and Ψ with resolution $n = 800$.

Figures 21 and 22 suggest that overall the function remains constant for the first part of the time domain, independent of the resolution. Depending on the resolution, Φ remains constant until $t = 170$ or $t = 190$, as shown in Figures 21a, 21b, 22a and 22b. Regardless of the resolution, the values for Φ are large, being of the order of 10^{23}.
At later times, the data for Φ shows different behaviour depending on the resolution. For the resolution $n = 100$, the data shows a oscillatory behaviour from $t = 170$ and onwards. From Figure 21a we see that the amplitude grows. For higher resolutions, such as $n = 200$ in Figure 21b, $n = 400$ in Figure 23a and $n = 800$ in Figure 23b, the data shows an oscillatory behaviour which grows at first but then is dampened, akin to quasi-normal mode signals. However, after $t = 260$ the data with resolution $n = 200$ stops being dampened and continues to oscillate with an approximately constant amplitude. This is similar to the data with resolution $n = 400$ after $t = 260$. However, in the case of resolution $n = 800$ the data seems to be dampened until $t = 260$, after which the amplitude starts to slowly increase again.

Figure 23: Plots showing the data for Φ from equation (87) at $r_* = 124$ as a function of t on the domain $[0, 300]$.

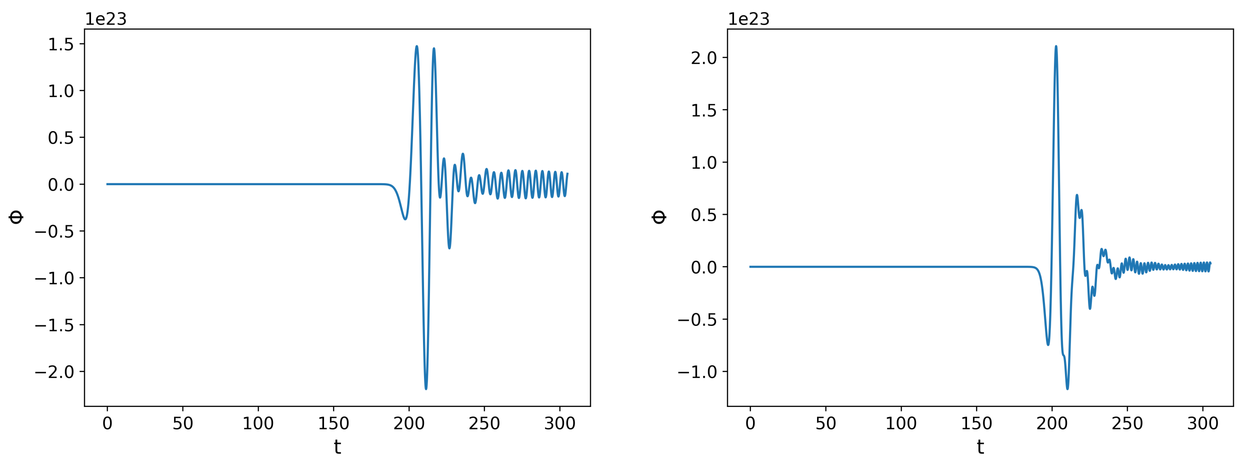

(a) Plot showing the data for Φ with resolution $n = 400$. (b) Plot showing the data for Φ with resolution $n = 800$.

It is clear that characteristics of the signal at late times, such as the period, the amplitude, the extent of damping, etc. are highly dependent on the resolution. The frequency of the oscillatory behaviour increases as the resolution increases. At higher resolutions, the data is also more irregular. This can be seen from the $n = 800$ case in Figure 23b, in which there are two local minima reached just after $t = 200$. This behaviour is not observed when $n = 200$. The difference can plausibly be attributed to the fact that the initial data for the incoming wave depends on the resolution taken, which influences the interaction between the incoming data and the potential. Given that the form of this data at late times is highly dependent on the resolution, it is unclear whether this behaviour is characteristic to the data or is coming from boundary effects of the data that are dependent on the resolution.
At the beginning of the time domain, $[0, 10]$ to be exact, Figure 24 shows that the value of Φ linearly decreases. This holds true for any resolution. This behaviour can be explained by the fact that on this time domain, the value of Ψ is 0, while Π is a constant negative value. When the domain is extended to $[0, 50]$, the data shows the exact same behaviour. This behaviour can not be detected by looking at the overall form, since

the decrease is constant and the coefficient is $\Pi = -1$, making the decrease of orders 10^0 to 10^2, which are much smaller than 10^{23}. This behaviour is unexpected, as the data is expected to be 0 far away at early times, since the signal should not have reached the point yet. This suggests that there is an error in the initial data at large spatial coordinates.

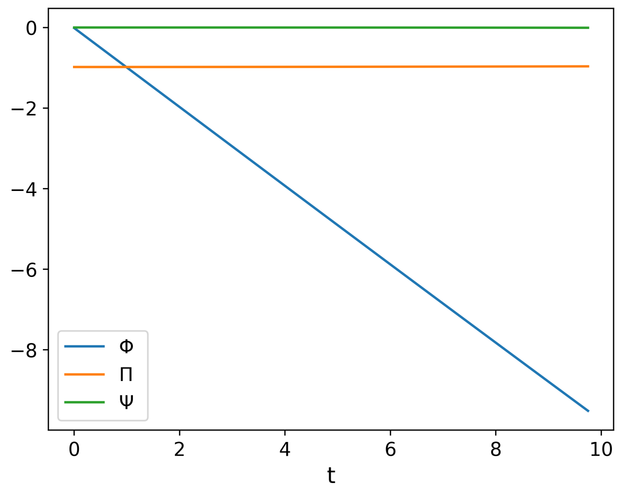

Figure 24: Plot showing the data for Φ from equation (87), Π from equation (89) and Ψ from equation (130) as a function of t on the domain $[0, 10]$. The different datasets are colour coded and marked in the legend. The resolution is $n = 200$.

8.3 Tests of the data

As demonstrated in the previous section, the results depend on the resolution of the data, which suggests that there is no numerical convergence. In this section, we will go into more detail about the lack of convergence and stability by discussing the total energy of the system and some of the convergence checks that have been performed. Further tests can be found in the Jupyter Notebook file in `https://github.com/PiortKosret/MasterThesisFinal.git`.[16]

8.3.1 Energy

Analysing the total energy of the system is commonly used as a robust way to check the numerical stability of a method. We expect the total energy of the system to be conserved or to monotonically decrease when the pulse starts to leave the spatial domain.

As illustrated in Figures 25a and 25b, the total energy increases monotonically until $t = 150$, regardless of resolution. This is expected when looking at the numerical solution, since the data of Φ keeps decreasing in the beginning of the spatial domain until $t = 150$, which happens for each resolution. There is a slight bump at $t = 70$, which is when the potential starts interacting with the data. From Figure 25a and 25b we can see that the energy of the system at late times is more stable and approximately constant, although the value for the total energy of the system is different for each resolution. This is expected, given that at late times the values for the energy are dominated by Φ, which has different values across different resolutions. In the case of $n = 100$, the solution seems to be non-constant, even after $t = 170$.

[16]The tests for the case where adds the potential instead of subtracting it are less excessive but cover most of the same grounds.

Figure 25: Plots showing the total energy of the system from equation (151) as function of t on the domain $[0, 300]$.

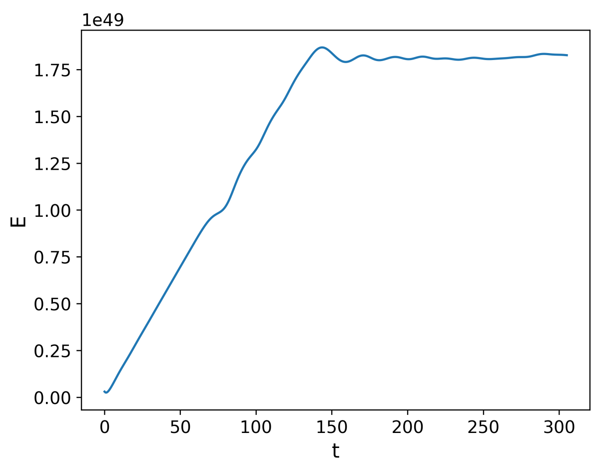

(a) Plot showing the total energy with resolution $n = 100$.

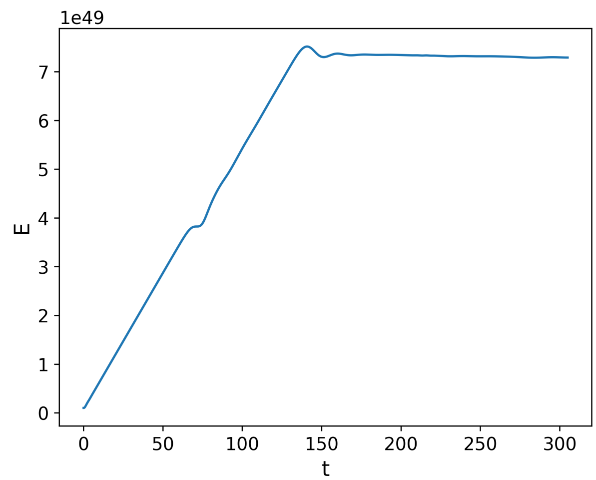

(b) Plot showing the total energy with resolution $n = 400$.

Figure 26: Plots showing the total energy of the system from equation (151) for data as function of t in the domain $[150, 305]$.

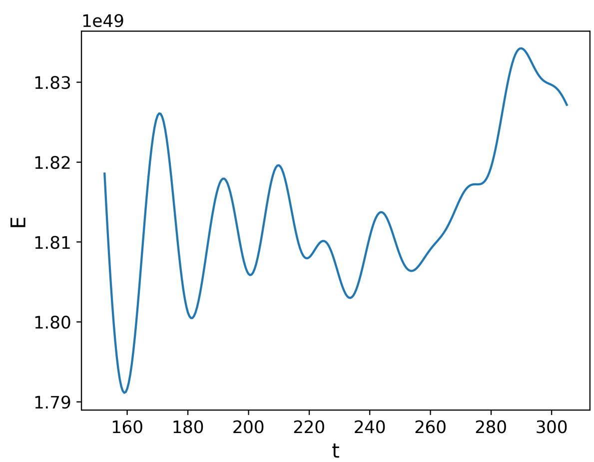

(a) Plot showing the total energy with resolution $n = 100$.

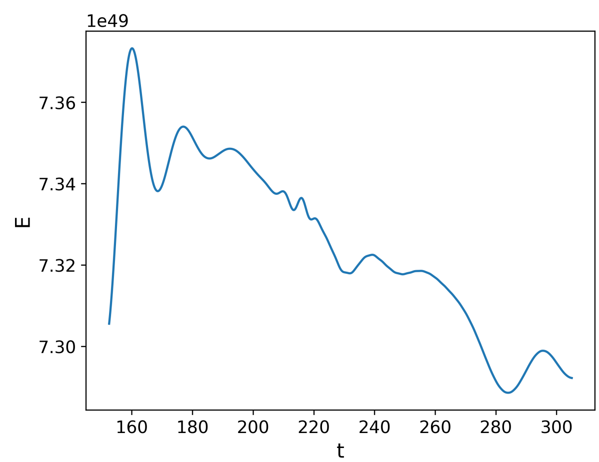

(b) Plot showing the total energy with resolution $n = 400$.

Looking at the total energy of the system on the time domain $[150, 305]$, illustrated in Figures 26a and 26b, we see that, at late times the total energy overall both increases and decreases depending on the resolution. The total energy occasionaly shows oscillatory behaviour, while at other times it suddenly drops and rises. There seems to be no overall pattern when the resolution is increased. The numerical solution therefore acts wildly different depending on the resolution, which suggests that the signal at the end of the time domain is heavily influenced by the errors from the boundaries.

8.3.2 Plotting of errors

Let us now examine the error functions from Section 7.1.1 to analyse the numerical convergence and potential origins of the problems from the previous section. Given our implementation of the RK4 method and the finite difference approximation, we expect that the code has convergence of order $p = 2$ at the interior and $p = 1$ at the boundaries.
In the code we compare the data for Φ, Π and Ψ for resolution $n = 200$,$n = 400$ and $n = 800$. For the first error function we take the difference between the values for the data with $n = 200$ and $n = 400$. For the second error function, we consider the difference between the values for the data with $n = 400$ and $n = 800$. From the theory behind the errors scaling check, one would expect the blue curve from Figures 27a and 27b to be a factor $2^p = 4$ larger than then the orange curve. Even though the blue and orange curves have similar shapes, the orange curve is already larger than the blue curve if we take $p = 1$. If we consider $p = 2$, the discrepancy would be even larger. The case where $p = 2$ is not shown in the plots, as the resulting rescaling would obscure the similarities between the curves.

Figure 27: Plots showing the L_2-norm of the errors from equations (153) for Φ with $p = 1$ for each time slice t in the domain $[0, 300]$.

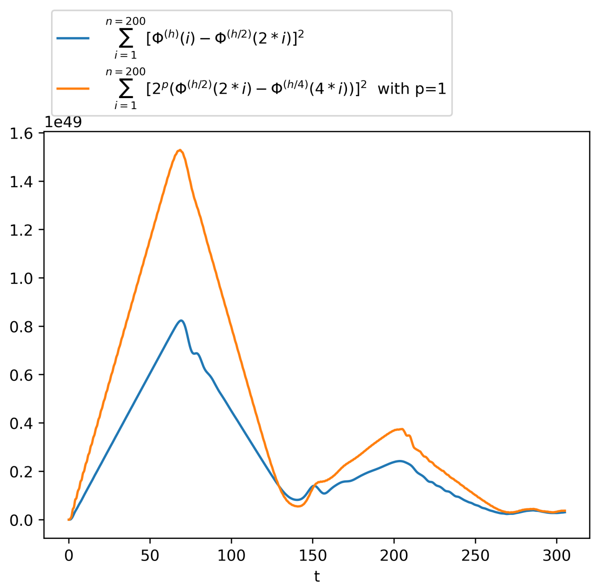

(a) Plots showing the norm for each time slice t in the domain $[0, 300]$.

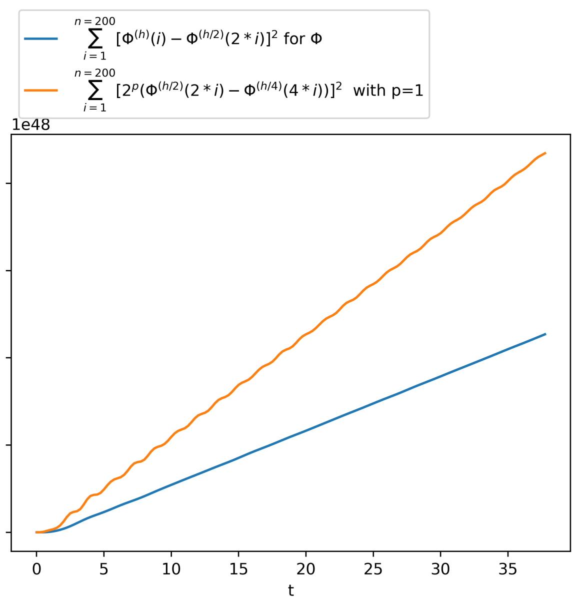

(b) Similar plot to Figure 27a, but now only for the domain $t = [0, 40]$.

Figure 28: Similar plots to Figure 27, but now considering Π and Ψ.

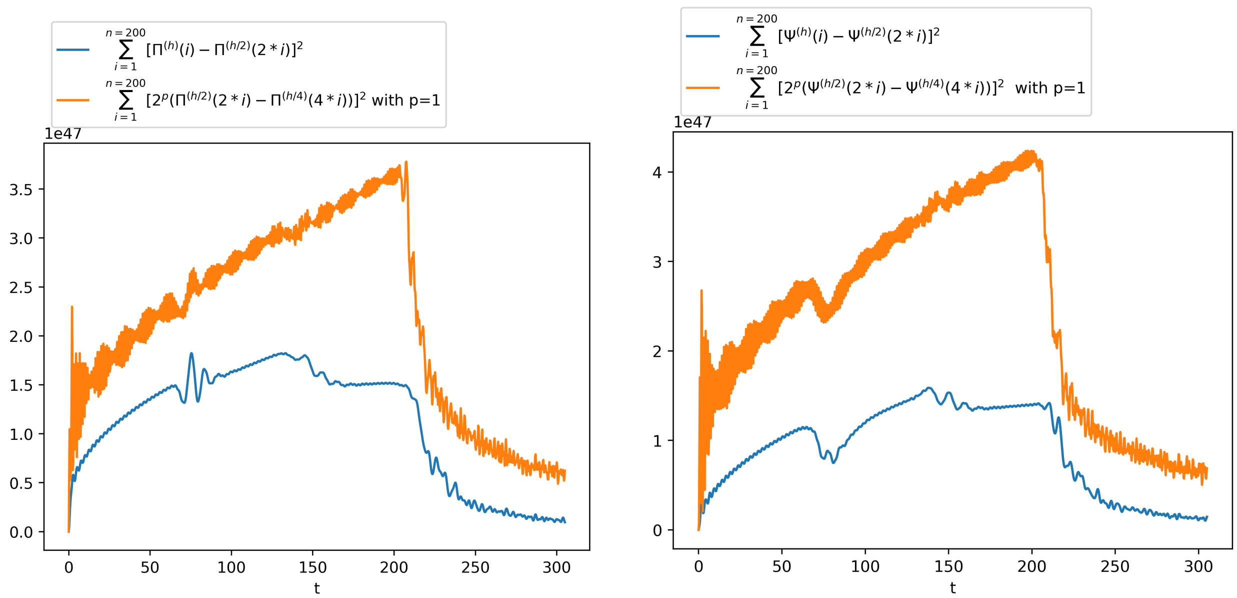

(a) Similar plot to Figure 27a, but now considering Π.

(b) Similar plot to Figure 27a, but now considering Ψ.

From Figure 28a and 28b, we see that the problem with the rescaling also happens for Π and Ψ. The norm of the second error is larger than the norm of the first error, even when $p = 1$. The norm of the error functions for Ψ and Π behave more erratically than the error functions for Φ. This behaviour suggests that the issue with convergence could be caused by the behaviour of Π and Ψ.
We have also checked to see if any of the curves from Figures 27 and 28 overlap if $p = 2, p = 0, p = -1$ and $p = -2$. However, they do not line up for any of these values of p. This suggests that the right fit for p would be a faction, which is unexpected, since this would suggest that the convergence order would not be a natural number.
It is also informative to consider the error functions pointwise, as it allows us to see at which spatial points the convergence problems start. Looking at the plots for the error functions at early times ($t = 0.25$) in Figure 29a, we see that errors originate from the left side of the spatial domain. When looking at a later time ($t = 22.25$), the error propagates further inward in the spatial domain, as we see in Figure 29b. This suggests that the problem with the convergence comes from the initial data on the left spatial boundary point. As shown in Figures 30a and 30b, the pointwise errors at late times do not resemble each other, regardless of rescaling. Figure 30a also shows that the error on the left boundary point keeps dominating at each time slice. The issues with the numerical solution therefore originates from the left side of the spatial domain and is due to the initial values, since this behaviour does not occur for different initial values (see Section 7).

Figure 29: Plots showing the pointwise errors from equation (153) for Φ with $p = 1$ as function of r_* on the domain $[-75, 125]$. The different error functions are colour coded and marked in the legend.

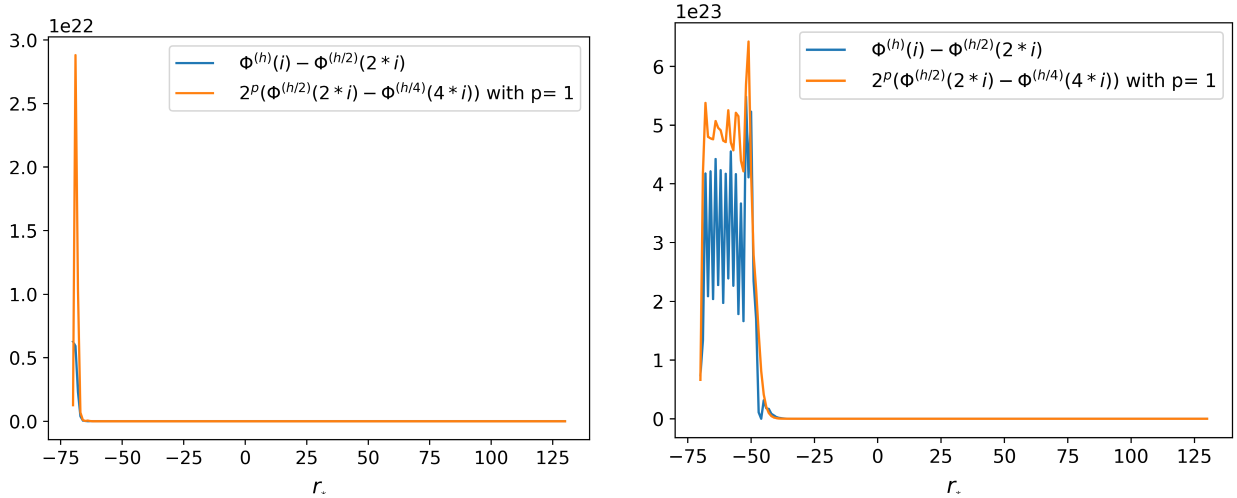

(a) Plot showing the pointwise errors for Φ at $t = 0.25$.

(b) Similar plot to Figure 29a, but now at $t = 22.25$.

Figure 30: Similar plots to Figure 29, but now at different times.

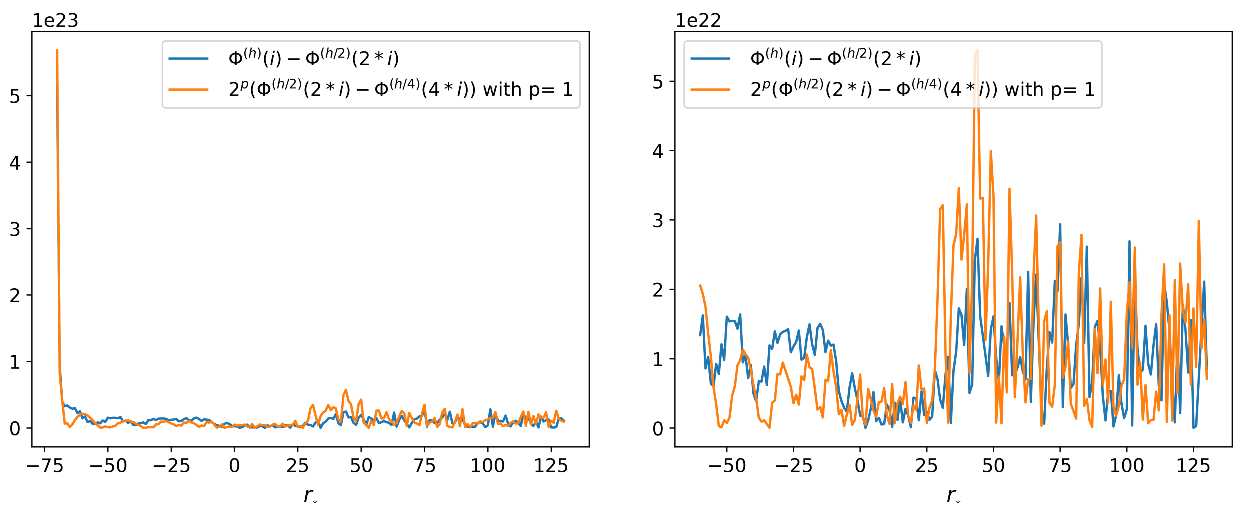

(a) Similar plot to Figure 29a, but now at $t = 304.75$.

(b) Similar plot to Figure 29a, but now at $t = 349.75$.

9 Conclusion and discussion

In this thesis, we used the Close Limit Approximation to get the initial data for the three dimensional space metric γ_{ab} and extrinsic curvature K_{ab} at $t = 0$. Consequently, this initial data was cast into the Regge-Wheeler formalism to get initial data for the gauge-invariant Zerilli function ψ, its time-derivative $\partial_t\psi$ and its spatial derivative $\partial_{r_*}\psi$. We got approximately the same result for the coefficients up to first order as in [57], except for some minus signs. Evolving the initial data using a solver was unsuccessful, since there is a lack of numerical convergence. Results far away and near the horizon are heavily dependent on the resolution, which is most likely caused by an instability near the horizon. There are some other peculiarities, such as the time-derivative being non-zero far away at early times, which suggests there is a more general problem with the initial data.

In this section, we will firstly discuss ways to resolve the dependency of the data on the resolution. Subsequently, we will discuss ways for further research using first order perturbation theory and the Close Limit Approximation. Afterwards, we discuss second order perturbation theory. Lastly, we discuss potential comparisons with numerical data.

9.1 Solving the code

As Section 8.2 shows, the problem is likely to be an instability in the initial data near the horizon. In this section we will discuss methods for further investigation or alternatives to solve the issue.

9.1.1 Checking initial data

Since our test on simpler toy models show that the code has second order convergence, a reasonable start would be to check the initial data.

One way to check the initial data is by presuming a specific time-dependence of the Zerilli function and seeing if it solves the Zerilli equation we have set up. This is done by using separation of variables and assuming that the time-dependence is of the form $e^{i\omega t}$, where $\omega \in \mathbb{C}$. The theoretical foundations and calculations can be found in Appendix E. However, due to time-constraints, we were unable to implement the test.

From this test, it is possible to assess whether the initial data at $t = 0$ solves the Zerilli Equation. If it does not solve the equation, there must be an error in the initial data.

9.1.2 Different Zerilli function

As stated in Appendix C, there are different forms of the Zerilli equation. One way to solve the problem with the initial data is picking one of the other formulations, leading to a different Zerilli function and therefore different initial data.

We opted for the gauge invariant form, because there were initially questions about the gauge choices made in the paper by Nicasio et al. [57].[17] As Tom van der Steen has shown in great detail [65], the gauge choices are correct, meaning we could consider the formalism used by Nicasio et al. [57].

No matter which formalism is picked, it would be easy to create the initial data for Φ, Π and Ψ in the code. One of the tests for the code was to try to get the same data as different papers. The different potentials and initial data for Φ, Π and Ψ can therefore already be found in the *InitialData.jl* file. Since the metric coefficients and gauge conditions have already been calculated, changes in the code would be minor.

Note however, that in this thesis, we have used the gauge invariant formalism of the Zerilli function. As

[17] The gauge choices in the paper are such that specific conditions are upheld for the second order perturbations. There was some conceptual ambiguity about some of the statements and about which choices needed to be made in what order. Due to time constraints, we opted for using the gauge invariant form of the Zerilli function.

a consequence, it is possible to obtain the initial data for Zerilli function ψ and its time-derivative by calculating the perturbation coefficient in any gauge. However, if a different formalism is chosen, the gauge-choices become more important. From Appendix A, we know that the relation between the time-derivative of the metric and the extrinsic curvature is dependent on the shift and lapse. These shift and lapse are dependent on which coordinates you ascribe to the points on a time-slice. Employing a gauge transformation on the coordinate system would therefore change the shift and lapse. The most useful gauge would be the Regge-Wheeler gauge, which simplifies the calculation of the time-derivative of the Zerilli function by making the perturbative and shift to be zero. Other non gauge invariant formalisms can therefore also be considered using these transformations.

9.2 Further research into first order perturbation theory

So far, we have extended the classic stationary black hole merger by analytically and numerically analysing the context of boosted black holes at first order. This is a good first step towards describing more complex black hole mergers. In this section, we will highlight which simplification could be lifted and what that would mean for applying the Close Limit Approximation.

9.2.1 Unequal mass and momentum

In this thesis, we have used that the two black holes have the same mass m and reverse momenta $\vec{P}_1 = -\vec{P}_2$. It is possible to consider the context where the black holes have unequal masses and/or different momenta, expanding on [53, 87] .

If the black holes have different masses and/or momenta, the calculation for the extrinsic curvature becomes much more involved. As seen in the calculations from Section 2.1, some of the terms would not cancel anymore and coefficients for odd l Legendre polynomials would become non-zero. The consequence would be that the coefficients of the extrinsic curvature would be different, which would impact the initial data at $t = 0$ for the time derivative of the Zerilli function. From equation (30), it is clear that also the regularising term of the conformal factor changes, which means that the metric coefficients would also change. However, the rest of the scheme is unchanged.

So far, we have assumed the momentum is head on and is of the same order as the length. However, most black hole collisions happen at ultra relativistic speeds and are not head-on collisions. Applying the Close Limit Approximation for ultra relativistic speeds would mean we only expand in L and the momentum P can become a parameter of the code that is independent of the parameter L. Relaxing the condition of head-on collisions would also be more realistic, as current studies suggest that most of Black Hole mergers will have quasi-circular inspirals [88, 89]. Generalising the system to have a quasi-circular inspiral would impact the form of the extrinsic curvature K_{ab}, but we could still use the Bowen-York initial data [90].

9.2.2 Black holes with spin

So far, we have been working with two boosted black holes that have no charge and are non-rotating. Consequently, the resulting black hole is also non-rotating. Relaxing these conditions would create a more realistic model of black hole mergers.

So far, the Close Limit Approximation has not been applied to the case of Kerr black holes. Introducing spin for the resulting black hole would significantly change the methods we have used. The background metric would change, like the metric perturbations. The Teukolsky equation would need to be used instead of the Zerilli equation, since the Zerilli equation is specific to the Schwarzschild case (see Appendix C). It would also not be possible to use the Bowen-York initial data [91, 92]. Adapting the description based on coordinates might prove too difficult or extensive, so adapting ,for example, the Newman-Penrose formalism might be more useful. Such a tetrad formalismuses spin-weighted harmonics as a basis instead of the tensorial harmonics we have used so far [34, 93]. The resulting QNM's can be compared to numerical models [94, 95] and semi-analytical methods [96, 97].

9.2.3 Black holes with charge

Charged black holes are physicially unlikely due to charge neutralization from surrounding matter. However, they are not ruled out by observations: current numerical models for non-spinning electrically charged black holes show that systems with small charge-mass ration up to 0.3 are consistent with gravitational waves observations of LIGO/Virgo[98, 99]. This opens ups a new wat to expand our current methods by considering charged black hole spacetimes.

To incorporate charge, it is natural to start with the Reissner-Nordström metric which describes non-spinning electrically charged black holes [35, 100]. In this background, linearized perturbations satisfy the Einstein-Maxwell equation. The gravitational perturbation can be decomposed into tensor spherical harmonics, while the electromagnetic perturbation can be expanded in vector harmonics. These coupled systems reduce to two Schrödinger-like equations which determine the gravitational field and electromagnetic field [101]. Applying perturbation theory would require us to consider different Zerilli functions and completely reevaluate how to calculate the initial data [102, 103].

The final data can be compared to fully nonlineear numerical simulations. While these models are less abundant than numerical models for uncharged spinning black holes, several studies have modeled non-spinning electrically charged black holes [104, 105]. Most models consider an electric charge, but models for magnetically or general $U(1)$ charges also exist. These charged spacetimes can be used to nalyse modified theories of gravity which contain additional gauge or scalar fields [106, 107].

The most general explicit solution for a black holes describes black holes with both spin and electric charge. According to the no-hair theorem, this is the most general stationary solution for black holes [108, 109]. The background of the spacetime would the Kerr-Newman metric. Applying perturbation to this metric is much more complicated than the Schwarzschild or Reissner–Nordström metrics. Current perturbation theories focus on the slow-rotation limit [110, 111]. However, the presence of spin and charge leads to coupling of spin-1 (Maxwell) fields and spin-2 (gravitational) fields. The resulting system of equations can be cast into a set of five real second order ODEs, two of which are Teukolsky type equations, two of which are generalized Regge-Wheeler equations and one of which is a first order algebraic relation [34]. Encorporating both spin and charge to the Close Limit Approximation would therefore require large changes of the numerical solver, since five coupled equations need to be solved. Similarly to the Reissner-Nordström case, how to calculate the initial data would need to be reevaluated.

9.3 Metric perturbation up to second order

So far, we have considered first order metric perturbations ${}^{(1)}g_{\mu\nu}$. It is possible to include second order perturbations of the metric ${}^{(2)}g_{\mu\nu}$, which would lead to a more precise description of the system[50, 112, 113].

In this section, we will discuss how it would be possible to apply the framework given in this thesis to second order. Since the original goal of this paper was to analyse the Zerilli function at second order, the calculations for the coefficients have already been performed and can be found in Appendix B.

9.3.1 Second order Zerilli equation and function

When applying second order perturbation theory, there are two different Zerilli equations that need to be solved. The first order Zerilli equation would not change and the second order Zerilli equation has a source

term.
At second order, a new Zerilli-type equation follows from the Einstein equations analogously to the first-order case (see Appendix C). This equation is satisfied by a second-order Zerilli function $\chi(r,t)$.[18] It includes a new source term and takes the form

$$\frac{\partial^2 \chi}{\partial t^2} + \frac{\partial^2 \chi}{\partial r_*^2} + V(r)\chi = S, \tag{163}$$

where $V(r)$ is the same potential term as in the first-order equation, r_* the tortoise coordinate, and S the second-order source term. This new source term will be dependent on the mass of the black holes m, the order of expansion in Legendre Polynomial l, radial coordinate r, and the first order Zerilli function $\psi(t,r)$ and various of its derivatives with respect to r, t. This source term can be extremely long, as shown in [57], being half a page long. The source term can also be divergent, depending on the gauge choices made [57, 65]. This can be solved by considering a different gauge at first order or by redefining the wave function to have a quadratic term in first order perturbations [114].
Besides calculating the initial data for $\chi(r,t)$ and the new source term S, the Julia code would also need to be changed to to solve equation (163). Introducing the source term for solcing Φ in the $rhs!$ function adds non-linearities for which the solver needs to be adapted. Solving the first order Zerilli equation at each t and afterwards solving the second order derivative is relatively easy to code. However, note that the source term S could have third order derivatives of ψ, which will need to be approximated. At the boundaries, there will be a larger error than at first order.

9.3.2 Gauge conditions

Currently, we have used the Gauge-invariant Moncrief-Zerilli function, which means we did not have to deal with gauge transformations. There is a gauge invariant and covariant (i.e. independent on the background coordinates) formalism that could be used for second order perturbations on a Schwarzschild background [115].
Using a different Zerilli formalism which is not gauge-invariant would require gauge transformations to simplify calculations. Fulfilling these gauge conditions in second order theories is more complex than satisfying gauge conditions at first order in perturbation theories. This is not only because second order terms and equations are more expansive, but also because first order gauge transformations create second order terms. This requires you to fulfil gauge conditions order by order, while bookkeeping how previous order gauge transformations change your second order quantities. Extensive calculations of these gauge conditions can be found in [65].

9.4 Comparing data to numerical data

Numerical models for General Relativity are seen as the benchmark for solutions of the Einstein Equations [116]. They are able to solve the full nonlinear Einstein Equations and use fewer assumptions to describe the initial data, creating more accurate prescriptions of gravitational waves [37]. It would therefore be interesting to compare the data we get at the horizon and null infinity with numerical results.
Comparing data at the horizon is challenging, since numerical methods use Marginally Outer Trapped Surfaces (MOTS), which differ from the event horizon used by the Close Limit Approximation. Marginally outer trapped surfaces are used to characterize the black holes quasi-locally for each time slice during the simulation [38, 117]. A marginal surface is a two dimensional surface with the topology of a sphere, such that normal outward going light rays going have vanishing expansion. The outermost of such surface is called the apparent horizon [118]. If the apparent horizon differs from the event horizon, the apparent horizon is located

[18] Here we follow the same notation as in [57].

within the event horizon [117]. Even though the Close Limit Approximation has been used to characterize the merger phase, the comparisons with numerical data should therefore be with late-time data, when the black hole has stabilized.
Comparing the numerical data can be based the waveform shape, energy output and QNM content [57, 119]. There exist semi-analytical research that combines the Close Limit Approximation with post Newtonian initial conditions [120]. In this method the numerical simulations cover the essential non-linear interaction of the merger, until the close limit approximation can be used [121]. Numerical models for a low-velocity head-on collision for boosted non-spinning black holes already existed in 1975 [122, 123]. However, there are also more recent studies that analyse such collisions with higher resolutions [52, 124].

Appendix

A ADM formalism

To understand this thesis, one needs to have an understanding of the Arnowitt-Deser-Misner (ADM) formalism of General Relativity. This formalism is also called the $3+1$ decomposition and makes use of a foliation of a space-time M.

A.1 Canonical form

The canonical formulation of General Relativity was introduced to determine the number of independent dynamical modes of the gravitational waves. This was done by casting General Relativity into a Hamiltonian formalism. This was necessary, because the gauge-freedom inherent to General Relativity lead to conceptual difficulties [125].
General Relativity describes gravity as a curvature of space-time, where the space-time is described by pseudo-Riemannian manifolds. These manifolds have a metric which carries information about the curvature of the manifold, and have an atlas containing chart which carry information about the coordinates used to describe the manifold. This can lead to conceptual difficulties, namely the interpretation of the coordinates. There is no preference for any set of coordinates and some coordinate systems have the same geometric characteristics, e.g. curvature, and satisfy the same Einstein Equations. This is because the Einstein Equations and geometry don't constrain the system enough to have one unique solution. One therefore has gauge-freedoms for the coordinate systems [125].
To recast the system in ADM form, one analyses the gravitational field using a Lagrangian formulation and uses two axioms. The first axiom is that the field equations have only of first order time derivatives. The second axiom is that the space-time can be described in a $(3+1)$ form. The latter axiom is needed because a Hamiltonian describes the physical state at a certain time. This can be seen from the fact that to be able to define a momentum p, one needs to take the time of its configuration variable q, i.e., $p = \frac{\partial \mathcal{L}}{\partial \partial_t q}$. Therefore, one needs a distinguished time, which leads to the foliation [126].
Note that the second axiom restricts the topology, but the theory is still covariant. That is to say, the system is invariant under an arbitrary change of coordinates. This follows from the fact that the topology of the manifold is independent of the coordinate system one uses.

A.2 Embeddings of hypersurfaces

Let us consider a four dimensional Lorentzian manifold of the form $(M, g_{\mu\nu})$. Instead of using a general topology, the ADM formalism uses the $3+1$ split, such that $M \cong \mathbb{R} \times \ ^{(3)}\Sigma$. The $3+1$ split restricts the topology of the space-times we consider, but leads to an easier formulation of the space-time. In this section, we will lay out the topological foundation of the $3+1$ split, specifically the definition and topology of hypersurfaces.
A set $\Sigma \subset M$ is called an n-dimensional **hypersurface** if it is an image of an embedding $\Phi : \hat{\Sigma} \to \Sigma \subset M$, where $\hat{\Sigma}$ is itself an n-dimensional manifold. The fact that Φ is an embedding means that $\Phi\big|_{\hat{\Sigma}}$ is homeomorphic. Equivalently, it means that Φ is a continuous bijective mapping whose inverse is continuous. Since the mapping is bijective, it is not possible for the hypersurface to intersect itself [127].
Let us consider a point $p \in \hat{\Sigma}$. The embedding Φ induces a **push-forward**

$$\begin{aligned} \Phi_{p*} = d\Phi_p : T_p\left(\hat{\Sigma}\right) &\to T_{\Phi(p)}(M) \\ v_p &\mapsto d\Phi_p(v). \end{aligned} \tag{164}$$

We use the same conventions and definitions as in the books by Lee [127, 128]. This means that for $f \in C^\infty(M)$, we use the notation $d\Phi_p(v)(f) = v_p(f \circ \Phi)$.
We can use the push-forward $d\Phi_p$ to introduce a **pull-back**

$$\begin{aligned} \Phi_p^* = d\Phi_p^* : T^*_{\Phi(p)}(M) &\to T_p^*(\hat{\Sigma}) \\ \omega_{\Phi(p)} &\mapsto d\Phi_p^*(\omega). \end{aligned} \tag{165}$$

Here $T_p^*(M)$ are the linear forms of $T_p(M)$, e.g.

$$\begin{aligned} \omega_p : T_p(M) &\to \mathbb{R} \\ v_p &\mapsto \omega_p(v_p) = \langle \omega, v \rangle_p. \end{aligned} \tag{166}$$

In the context of a pull-back, we therefore have

$$\begin{aligned} d\Phi_p^*(\omega) : T_p(\hat{\Sigma}) &\to \mathbb{R} \\ v_p &\mapsto \langle \omega_p, d\Phi_p(v) \rangle. \end{aligned} \tag{167}$$

To illustrate the above definitions, one can find a schematic of the mappings in Figure 31.
Consider now again a Lorentzian manifold (M, g). Note that the metric g is a bilinear form on M, which implies that we can use the embedding to create an induced metric $\hat{g}$ on $\hat{\Sigma}$. This is done by defining

$$\begin{aligned} \hat{g}_{\mu\nu} = \Phi^* g_{\mu\nu} : T_p(\hat{\Sigma}) \times T_p(\hat{\Sigma}) &\to \mathbb{R} \\ (v_p, w_p) &\mapsto \hat{g}(v_p, w_p) = g\left(d\Phi_p(v), d\Phi_p(w)\right). \end{aligned} \tag{168}$$

We call an n-dimensional hypersurface an n-dimensional **spatial hypersurface** if the embedding of the n-dimensional manifold $\hat{\Sigma}$ on the manifold (M, g), has an induced metric which has Riemannian (or positive) signature [128].

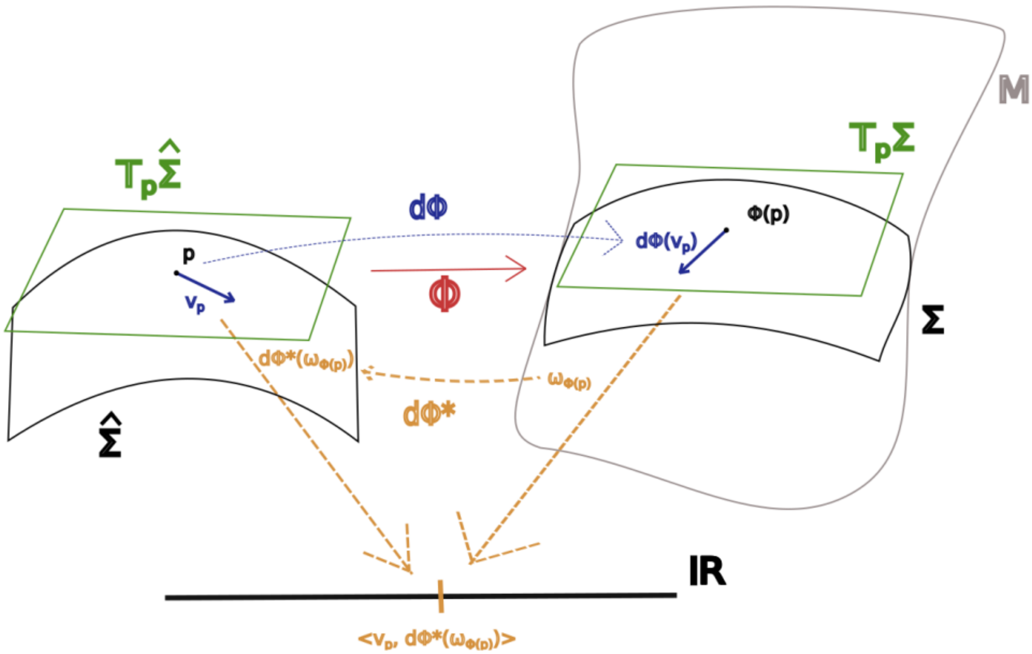

Figure 31: A figure showing an embedding of a surface $\hat{\Sigma}$ into a Manifold M via an embedding map Φ (shown in red). It shows the relations between the tangent spaces $T_p(\hat{\Sigma})$ and $T_{\Phi(p)}(\Sigma)$ via the push-forward $d\Phi$ (shown in blue). It also shows the relation between the linear forms $T^*_p(\hat{\Sigma})$ and $T^*_{\Phi(p)}(\hat{\Sigma})$ via the pull-back $d\Phi^*$ (shown in orange).

A.3 Definition of foliation

Since we have defined the topology of the manifold and hypersurfaces, we can give a definition of a foliation. From this definition, we can analyse the geometric interpretation and introduce a coordinate representation that we will use to explain the time-evolution of the hypersurfaces.
Let us consider a Lorentzian manifold (M, g). We say that the manifold can be **foliated** by a family of space-like hypersurfaces $(\Sigma_t)_{t\in\mathbb{R}}$ if there is a smooth scalar field $\hat{t}$ on M which is regular[19], such that each level surface of the scalar field is one of the space-like hypersurface. This means that $(\Sigma_t)_{t\in\mathbb{R}} = \{p \in M \big| \hat{t}(p) = t\}$ and $M = \bigcup_{t\in\mathbb{R}} \Sigma_t$. Since the gradient of the scalar field $\hat{t}$ is non-zero everywhere, the different hypersurfaces don't intersect each other [129]. Since we are working with a four dimensional manifold, the spatial hypersurfaces are three-dimensional, which is why we introduce the notation ${}^{(3)}\Sigma_t$ for spatial hypersurfaces. For a visualisation of a foliation, see Figure 32.

[19]The definition of regular in this context is that the gradient of the scalar field is non-zero everywhere.

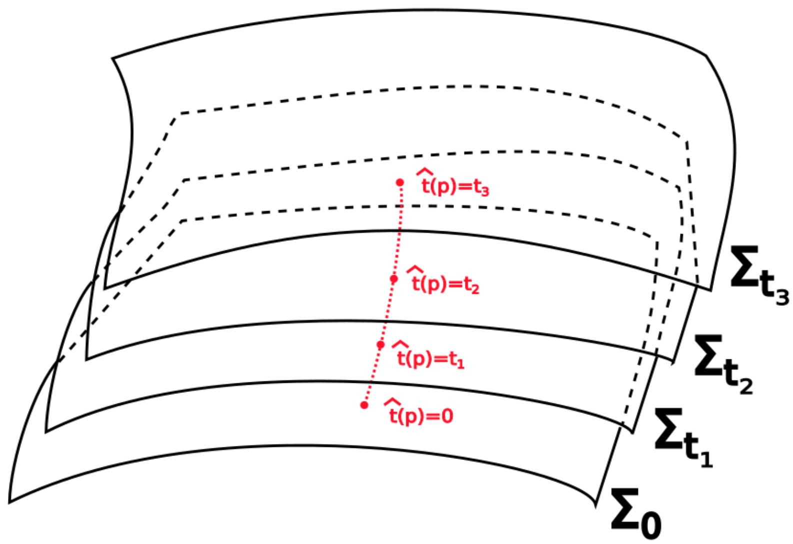

Figure 32: A picture showing a foliation $(\Sigma_t)_{t\in\mathbb{R}}$, where the spatial hypersufaces Σ_t are two-dimensional. The space between the hypersurfaces is exaggerated to visualise the stacking. In red, one can see part of the scalar field $\hat{t}$.

A.4 Metric decomposition

It is possible to relate the four dimensional spacetime metric g_{ab} to the three dimensional spatial metric γ_{ab} and K_{ab}. In this section, we will give a short recap on coordinates within differential geometry. Afterwards we introduce the lapse function N and shift vector $\mathbf{N}$ which allows us to relate two different spatial hypersurfaces ${}^{(3)}\Sigma_t$ and ${}^{(3)}\Sigma_{t'}$ to eachother. We conclude this section with the relation between the four dimensional spacetime metric g_{ab} and the three dimensional spatial metric γ_{ab}, the lapse function N and shift vector $\mathbf{N}$.

A.4.1 Recap on coordinates

We will start by recapping the definition of coordinates in the context of manifolds, to create clarity about the notation and definitions used. We use the convention used in the books by Lee [127, 128].

Consider a chart (U, ϕ) on an n-dimensional manifold M. The map $\phi : U \to \mathbb{R}^n$ is a diffeomorphism, meaning it is a bijective smooth map whose inverse is also smooth. In $\phi(U) \subset \mathbb{R}^n$, we can express points and vectors using the basis $(x_1, ..., x_n)$. This means that we can define **coordinate vectors** $(\partial_1, ..., \partial_n)$ in $T_p(M)$ via $\partial_a f\big|_p = \frac{\partial}{\partial x^a}\big|_p f = \frac{\partial}{\partial x^a}\big|_{\phi(p)} \left(f \circ \phi^{-1}\right)$ for $f \in C^\infty(M)$. This forms a well-defined basis for $T_p(M)$, as the inverse of ϕ is also a bijective smooth map. Using the coordinate vectors, one is able to define a **coordinate vector field** $X^i : \hat{\Sigma} \to T_p\left(\hat{\Sigma}\right)$, which sends $p \mapsto \partial_a\big|_p$ [127].

Let us now consider coordinates in the contexts of spatial hypersurfaces. Consider a chart (U, ϕ) on a hypersurface ${}^{(3)}\Sigma_t$ with coordinate vectors $(\partial_1, \partial_2, \partial_3)$. The embedding Φ induces a push-forward from $T_p\left({}^{(3)}\Sigma_t\right)$ to $T_{\Phi(p)}(M)$, which means that we can relate the coordinate vectors ∂_a to coordinate vectors $\partial_a^{'}$.

A.4.2 Lapse function

Let us consider a spatial hypersurface ${}^{(3)}\Sigma_t$. Before we can analyse the relation between two hypersurfaces, we need to introduce the normal of the spatial hypersurface. It is clear that this normal is related to the scalar field $\hat{t} = t$ via its gradient. The unit normal vector is then given by

$$\mathbf{n} = -N\nabla t = -\left(\langle dt, \nabla t\rangle\right)^{-1/2} \nabla t, \tag{169}$$

such that $\mathbf{n} \cdot \mathbf{n} = -1$. Here $N > 0$ is the **lapse function** [126].
As will be clear later, it is useful to define a **normal evolution vector m**, which is defined as

$$\mathbf{m} = N\mathbf{n}, \tag{170}$$

which is adapted to the scalar field t. This means that $\langle dt, \mathbf{m}\rangle = 1 = m^\mu \nabla_\mu t$ [129].
Consider now two hypersurfaces ${}^{(3)}\Sigma_t$ and ${}^{(3)}\Sigma_{t'}$ that are close to each other in the sense that $t' = t + \delta t$, where δt is a small number. Let us take a point $p \in^{(3)} \Sigma_t$ and consider $p' = p + \delta t\mathbf{m}$, we have

$$\hat{t}(p') = \hat{t}(p + \delta t\mathbf{m}) = \hat{t}(p) + \delta t \left\langle \hat{t}, \mathbf{m}\right\rangle = \hat{t}(p) + \delta t. \tag{171}$$

From this we conclude that $p' \in^{(3)} \Sigma_{t'}$ and from the definition of $\hat{t}$ it is clear that the mapping is bijective. Therefore, we can reach each point p' on the hypersurface ${}^{(3)}\Sigma_{t'}$ by taking the small displacement $\delta t\mathbf{m}$ on the hypersurface ${}^{(3)}\Sigma_t$. Alternatively, one can say that ${}^{(3)}\Sigma_t$ is **Lie dragged** to ${}^{(3)}\Sigma_{t'}$ via **m**.
Similarly, we can relate the two tangent spaces $T\left({}^{(3)}\Sigma_t\right)$ and $T\left({}^{(3)}\Sigma_{t'}\right)$ to each other. In this context, we have that

$$v \in T\left({}^{(3)}\Sigma_t\right) \iff \mathcal{L}_{\mathbf{m}} v \in T\left({}^{(3)}\Sigma_{t'}\right), \tag{172}$$

which means that we can now characterize how points and vectors change over time [130]. The mapping of vectors and points between two close hypersurfaces can be found in Figure 33.

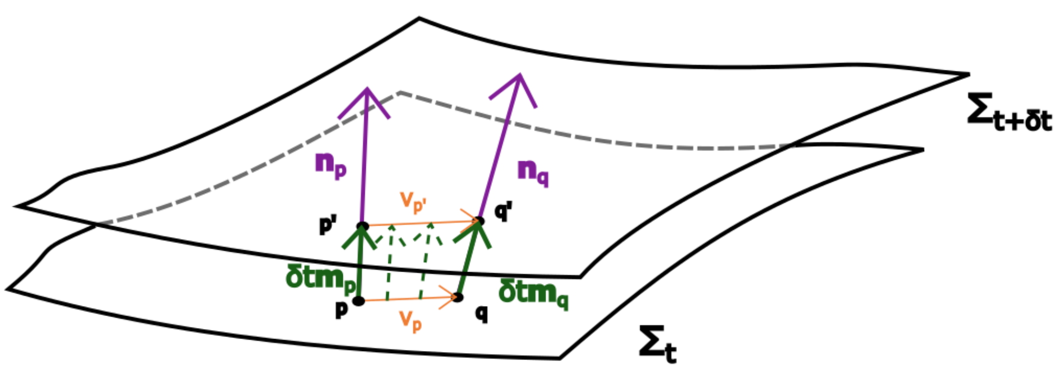

Figure 33: Figure showing two close hypersurfaces Σ_t and $\Sigma_{t+\delta t}$. The points p and p' are related to each other via $\delta t\mathbf{m}_p$, shown in green with solid lines, which is a rescaled version of the normal n_p(shown in purple). A vector $v_p \in T\left({}^{(3)}\Sigma_t\right)$, shown in orange, is tangent to the spatial hypersurface Σ_t and can be seen as a displacement between p and q. This vector v_p gets Lie dragged to $T\left({}^{(3)}\Sigma_{t+\delta t}\right)$ via the vector field $\mathbf{m}$, part of which is depicted in green with striped lines. The vector v_p therefore becomes $v_{p'} \in T\left({}^{(3)}\Sigma_{t+\delta t}\right)$, which is tangent to the spatial hypersurface $\Sigma_{t+\delta t}$. Therefore, the vector $v_{p'}$ can be seen as the displacement between p' and q', where q' is related to q via $\delta t\mathbf{m}_q$ shown in green with solid lines.

A.4.3 The shift vector

Let us consider two hypersurfaces ${}^{(3)}\Sigma_t$ and ${}^{(3)}\Sigma_{t'}$ that are infinitesimally close to each other, i.e. $t' = t + \delta t$, where δt is a small number. Using coordinates, we will introduce $\partial_t \in T_p(M)$, which relates two points on two infinitesimally close hypersurfaces, by having the same "spatial coordinates". The $\partial_t \in T_p(M)$ will be used to introduce the shift vector $\mathbf{N}$.
Let us consider a point p on the hypersurface ${}^{(3)}\Sigma_t$. Since ${}^{(3)}\Sigma_t$ is a hypersurface, the neighbourhood of p has a coordinate system $x^a = (x^1, x^2, x^3)$, which we call the **spatial coordinates**. This allows us to introduce the coordinate system $x^\mu = (t, x^1, x^2, x^3)$, which is defined on M.
The coordinates x^a allow us to define a basis for the tangent space of the hypersurface $T_p\left({}^{(3)}\Sigma_t\right)$, which we denote by ∂_a. Via the embedding Φ, we get three basis vectors for $T_p(M)$. To complete the basis, we will take a basis that spans the orthogonal complement to $T_{\Phi(p)}\left(\Phi\left({}^{(3)}\Sigma_t\right)\right) \subset T_{\Phi(p)}M$. This basis we call the **time vector** ∂_t, which we define such that $\langle \partial_t, dt\rangle = 1$. [20]
Consider now a point q on the hypersurface ${}^{(3)}\Sigma_{t'}$. Since ${}^{(3)}\Sigma_{t'}$ is a submanifold, there is a chart (U', ϕ') , such that $\phi'(q) = (t', x^{1'}, x^{2'}, x^{3'})$. Note that for each slice, we have the freedom to once change the maps in the charts belonging to the atlas of the spatial slice, such that $\phi'(q) = (t', x^1, x^2, x^3)$. Via the compatibility of the charts, this uniquely fixes the point on ${}^{(3)}\Sigma_{t'}$ that we associate with (t', x^1, x^2, x^3). This means that $\partial_t \in T_p(M)$ is pointing from p to q, since there is no change in spatial coordinates. In essence, this is the definition of ∂_t: it is the vector tangent to curves with constant spatial coordinates.
Consider p and q as described above. There is a difference between ∂_t and $\mathbf{m}$, as q does not necessarily need to lie orthogonal to the surface. Therefore, one can decompose

$$\partial_t = \mathbf{m} + \mathbf{N}, \tag{173}$$

where $\mathbf{N}$ is the shift vector. The shift vector is therefore implicitly defined by choosing which point on ${}^{(3)}\Sigma_{t'}$ you identify with the same spatial coordinates as p. We have that $\langle dt, \mathbf{N}\rangle = \langle dt, \partial_t\rangle - \langle dt, \mathbf{m}\rangle = 0$, which implies that the shift vector $\mathbf{N}$ is tangent to the hypersurface ${}^{(3)}\Sigma_t$ [129]. For a visualisation of these vectors, see Figure 34.

[20] See Section A.6 for a more in-depth explanation of causality and the parameter t.

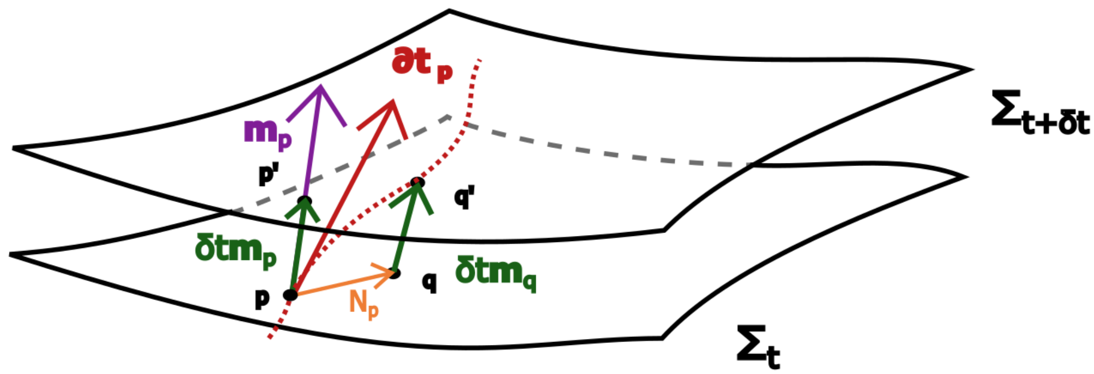

Figure 34: A picture showing the different vectors defined for a point $p \in^{(3)} \Sigma_t$. The normal evolution vector $\mathbf{m}_p$, shown in purple, is normal to the surface and a rescaled version of it, $\delta t \mathbf{m}_p$, points to a point $p' \in^{(3)} \Sigma_{t'}$. The point p' has different spatial coordinates than p. The striped red line shows the curve that denotes all the points which have the same spatial coordinates. The time vector ∂_p, shown with solid red lines, is tangent to the red striped line. The point $q' \in^{(3)} \Sigma_{t'}$ has the same spatial coordinates as p and therefore lies on the red striped line. The shift vector $\mathbf{N}_p$, shown in orange, is a vector in $T_p\left({}^{(3)}\Sigma_t\right)$, which points to $q \in^{(3)} \Sigma_t$. The point q is defined in such a way that the vector $\delta t \mathbf{m}_q$, shown in green, points to q'. The shift vector is therefore the projection of the time vector ∂_t unto the spatial hypersurface ${}^{(3)}\Sigma_t$.

A.4.4 Decomposing the space-time metric

In this subsection, we will relate the space-time metric $g_{\mu\nu}$ to the spatial metric $\gamma_{\mu\nu}$, the lapse function N and the shift N^μ. We will do this by analysing two hypersurfaces ${}^{(3)}\Sigma_t$ and ${}^{(3)}\Sigma_{t'}$ that are infinitesimally close to each other.
Using the notation from Section A.4.3, we can express the normal vector $\mathbf{n}$,

$$\mathbf{n} = n^\mu \partial_\mu = \frac{1}{N}\partial_t - \frac{N^a}{N}\partial_a, \tag{174}$$

where N is the lapse function and $\mathbf{N} = N^a \partial_a$ is the shift vector. Note that from the definition of $\mathbf{n}$, given in equation 169, we know that

$$\underline{\mathbf{n}} = -N dt. \tag{175}$$

Consider the spatial metric $\gamma = \gamma_{ab} dx^a \otimes dx^b$ and the space-time metric $g = g_{\mu\nu} dx^\mu \otimes dx^\nu$, we have

$$g_{tt} = g(\partial_t, \partial_t) = \langle \mathbf{m}+\mathbf{N}, \mathbf{m}+\mathbf{N} \rangle = -N^2 + N^a N_a \tag{176a}$$

$$g_{ta} = g(\partial_t, \partial_a) = \langle \mathbf{m}+\mathbf{N}, \partial_a \rangle = 0 + N_a = N_a \tag{176b}$$

$$g_{ab} = g(\partial_a, \partial_b) = \langle \partial_a, \partial_b \rangle = \gamma_{ab}. \tag{176c}$$

Alternatively, one can find an expression for the space-time metric $g_{\mu\nu}$, by calculating the distance between $p \in^{(3)} \Sigma_t$ and $q \in^{(3)} \Sigma_{t'}$. Using the Lorentzian form of the Pythagorean Theorem, one gets

$$\begin{aligned} ds^2 &= -(Ndt)^2 + \gamma_{ij}(dx^a + N^a dt)(dx^b + N^b dt) \\ &= \left(N^a N_a - N^2\right) dt^2 + 2N_a dx^a dt + \gamma_{ab} dx^a dx^b. \end{aligned} \tag{177}$$

Using equation (177) we can see that the space-time metric for the 3-1 decomposition is

$$g_{\mu\nu} = \begin{pmatrix} g_{0,0} & g_{0,a} \\ g_{b,0} & g_{ab} \end{pmatrix} = \begin{pmatrix} N^a N_a - N^2 & N_a \\ N_b & \gamma_{ab} \end{pmatrix} \tag{178}$$

One can also calculate the inverse of the metric, which is

$$g^{\mu\nu} = \begin{pmatrix} -\frac{1}{N^2} & \frac{N^a}{N^2} \\ \frac{N^b}{N^2} & \gamma^{ab} - \frac{N^a N^b}{N^2} \end{pmatrix}, \tag{179}$$

which shows that $g^{ab} \neq \gamma^{ab}$.

A.5 Extrinsic curvature

An important way to characterise the foliation is the extrinsic curvature K_{ab} of a hypersurface ${}^{(3)}\Sigma_t$. It denotes how the hypersurfaces are "folded" on each other and therefore tells us something about the time-evolution of the hypersurfaces.
Consider two points p and q on ${}^{(3)}\Sigma_t$ and their respective normal vectors $n^\mu\big|_p$ and $n^\mu\big|_q$. Let $n^{\mu\prime}\big|_q$ be the normal $n^\mu\big|_p$ parallel transported to q. The difference between the two vectors is a measure of the curvature of ${}^{(3)}\Sigma_t$, see Figure 35. This leads to the definition

$$K_{\mu\nu} = \gamma_\mu{}^\rho \nabla_\rho n_\nu, \tag{180}$$

where γ is the induced three-dimensional spatial metric on ${}^{(3)}\Sigma_t$ [21] and ∇ is the connection with respect to the space-time metric $g_{\mu\nu}$. As one can see, we have $K_{\mu\nu} n^\mu = K_{\mu\nu} n^\nu = 0$, which shows that this tensor field is purely spatial. We therefore will use the notation K_{ab}.
Alternatively, one can use the Lie derivative to write down the extrinsic curvature, which will be more useful when making gauge choices. One gets

$$\begin{aligned} K_{ab} &= \frac{1}{2}\mathcal{L}_{\mathbf{n}}\gamma_{ab} \\ &= \frac{1}{2N}\left(\partial_t \gamma_{ab} - D_a N_b - D_b N_a\right) \end{aligned} \tag{181}$$

where $\mathbf{n}$ is the unit normal vector field, γ_{ab} is the spatial metric on ${}^{(3)}\Sigma_t$, N is the lapse function, N_a are components of the shift vector and D the covariant derivative defined on ${}^{(3)}\Sigma_t$. As a consequence of equation (181), one can call the extrinsic curvature the "velocity" of the spatial metric γ_{ab}.

[21] This metric is induced by the embedding, see Section A.2.

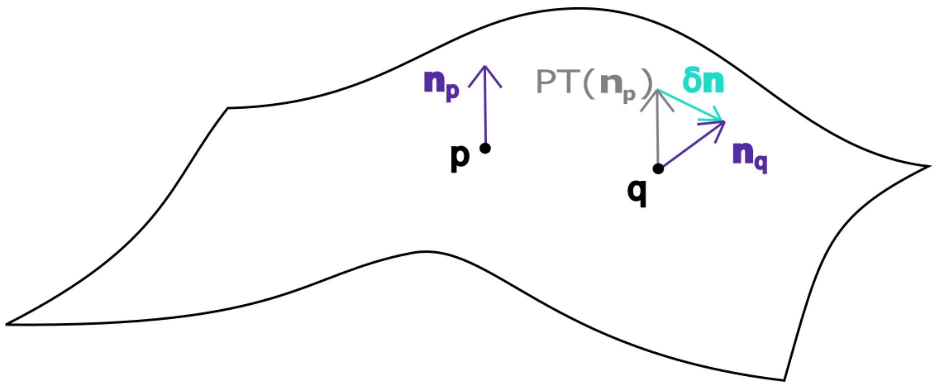

Figure 35: A picture showing a spatial hypersurface ${}^{(3)}\Sigma_t$. We mark a point $p \in^{(3)} \Sigma_t$, with its normal vector $\mathbf{n}_p$ shown in purple. If we consider another point $q \in^{(3)} \Sigma_t$, we can consider the normal vector $\mathbf{n}_q$ on that point, shown also in purple. One can parallel transport the normal vector $\mathbf{n}_p$ to q, which we denote as $\mathrm{PT}(\mathbf{n}_p)$ and is shown in grey. The difference between these two vectors, we call δn and is shown in light blue. This difference between these vectors is proportional to the extrinsic curvature at point q, e.g. $K_{ab} \propto \delta n$.

A.6 Causality

So far, we have only discussed the topology, geometry and coordinate systems within the ADM-formalism. However, we have not yet discussed the causal structure of the space-time. In this section, we will set up the groundwork to discuss the causal structure, by defining causality and light cones within Lorentzian manifolds. Afterwards, we can define the concepts of global hyperbolicity and Cauchy surfaces, which we can relate to the ADM formalism. We will use the definitions and conventions in the book Foundations of General Relativity by Klaas Landsman [131].

A Lorentzian manifold (M, g) is called a **space-time** if it is connected and has a **time orientation**, which implies that there is a global time-like vector field $T \in X(M)$ such that $g_p(T,T) < 0$ at each point $p \in M$.[22] This allows us to define non-zero vectors X_p that are **causal** ($g_p(X_p, X_p) \leq 0$) and **future-directed** ($g_p(T_p, X_p) < 0$) [23].

Since we have defined causal future directed vectors, we can define curves analogously. Consider a curve $c(t) : \mathbb{R} \to M$. We call it causal and future directed on $[0, T_{\text{end}}]$, if its derivative $\dot{c}(t)$ is causal and future directed on the whole domain. Consider two points $p, q \in M$, such that there is a causal future-directed curve from p to q. We denote this relationship via $p \leq q$. Using this definition, one can define future and past causal cones: $J^+(x) = \{y \in M | x \leq y\}$ and $J^-(x) = \{y \in M | y \leq x\}$.

Lastly, we will introduce the concept of a space-time being non-imprisoning. A space-time (M, g) is non-imprisoning if no inextendible future directed causal curve c is contained in a compact subset of M. This means that if one maximally extends a causal curve, it will "wonder off to infinity".

Using the above definitions, we can define what a Cauchy surface is. A **Cauchy surface** Σ is a subset

[22]Technically, in the Section about the geometry of the $3+1$ split, one normally already considers (M, g) to be a space-time. Note that ∂_t does not need to be this time-like vector, as it can be space-like or lightlike too (see [129] for a further explanation). The $\mathbb{R} \times^{(3)} \Sigma$ topology of the embedding is indepent of (M, g) being a space-time.

[23]The normal $\mathbf{n}$ of a spatial hypersurface is actually a future-directed vector.

such that each inextendible time-like curve intersects Σ in exactly one point. Equivalently, one can say that Σ is a Cauchy surface if and only if the domain of dependence is the whole space-time M. Using this definition, one can show that a Cauchy surface Σ needs to be a closed connected three-dimensional topological manifold of M and must be **achronal**. The latter meaning that no two points $p, q \in \Sigma$ can be connected by a timelike curve. If a space-time (M, g) has a Cauchy surface, then every other Cauchy surface Σ' is homeomorphic to Σ and that M is homeomorphic to $\mathbb{R} \times \Sigma$.[24]

With the previous definitions, we can now also define global hyperbolic space-times. We call a space-time **globally hyperbolic** is it is non-imprisoning and each double cone $J(p, q) = J^+(p) \cap J^-(q)$ is compact for each $p, q \in M$.[25] From this definition, one can get space-times with reasonable characteristic, such that it can describe the universe. For example, the space time being non-imprisoning implies that the space-time is **causal**, meaning that there are no closed causal curves. It also means that any point y in the future causal cone $J^+(x)$ can be connected via a future directed causal geodesic of finite maximal length.

Let's now consider all these characteristics of causality and space-times in the context of the ADM formalism. Sometimes, one assumes that the space-time one works with is globally hyperbolic. In this context, the foliation, as defined in Section A.3, is actually a consequence of global hyperbolicity, not the definition. Another important thing to note is that a space-time is globally hyperbolic if and only if it has a Cauchy surface Σ. This means that the spatial hypersurfaces ${}^{(3)}\Sigma_t$ are actually Cauchy surfaces, which means that there is more (causal) structure between hypersurfaces than one may presume from looking at the definition of a foliation. Another consequence is that some space-times are not suitable for the ADM-formalism, such as the Anti de Sitter space-times. This means that we restrict the space-times we can consider in the ADM-formalism, but it is a sacrifice worth making, since the causal structure give us reasonable characteristics [131].

A.7 The Einstein-Hilbert action

So far we, we have discussed the space-time and how it can be foliated with Cauchy surfaces ${}^{(3)}\Sigma_t$. As explained in Section A.6, there is a causal structure within the space-time related to points and causal cones. However, we have not yet considered the causal relationship between the surfaces themselves. This is what we will do in this section, by considering the Einstein Field Equations and the Einstein-Hilbert action.[26]

A.7.1 The Einstein field equation

Let us consider the Einstein-Hilbert action, which is given by

$$S_{\mathrm{EH}} = \frac{c^4}{16\pi G} \int_M d^4x \sqrt{-g}(R - 2\Lambda) - \int_{\partial M} d^4x \sqrt{\gamma} K = \frac{1}{2} \int_M d^4x \sqrt{-g} R. \tag{182}$$

In equation (182), the terms behind the first equal-sign denote the full action. We consider the term behind the second equal-sign for simplicity reasons. We therefore use natural constants, assume that the cosmological constant Λ is zero and ignore the boundary terms [131].

The Einstein Field Equations are given by extremizing the Einstein Hilbert action, with respect to the metric

[24]Note that this the relationship between Σ being a Cauchy surface and these characteristics is not an "if and only if", meaning that the above are not equivalent.

[25]It is important to note that there are multiple equivalent definitions of global hyperbolic space-times and that some definitions have changed over time. For example, sometimes people use strongly causal over non-impressoning.

[26]The Hamiltonian formalism of General Relativity, as discussed in Section A.1, was developed before the ADM-formalism. The equations one gets from the Hamiltonian formalism are equivalent to the equations we get below. We therefore forego an in-depth analysis of this formalism and refer to [129] and [126] instead.

$g_{\mu\nu}$ [132]. This give us

$$G_{\mu\nu} = R_{\mu\nu} - \frac{1}{2} g_{\mu\nu} R = 8\pi T_{\mu\nu} = 0, \tag{183}$$

where the last equal sign comes from the fact that we are considering the vacuum equations.
The Einstein Field Equations (183) are *underdetermined*. It is underdetermined in the sense that for any solution $g_{\mu\nu}$ to the set of equations (183), $\forall \psi \in \mathrm{Diff}(M) : \psi * g_{\mu\nu}$ is also a solution. This means that the solution to the Einstein Equations is independent of the coordinate system one uses. This characteristic is also called general covariance or invariance of the theory.

A.7.2 The 3+1 decomposition of the Einstein Field Equations

Since we have decomposed the space-time into slices of spatial hypersurfaces, it will be useful to decompose the Einstein Field Equations, such that they only contain three-dimensional variables. The decomposition will give us conditions on the three-dimensional variables, which, if satisfied, means that our system is consistent with General Relativity.
The Einstein Field Equation (182) can be rewritten to only contain the following three-dimensional variables: the spatial metric γ_{ab}, the extrinsic curvature K_{ab}, the shift vector $\mathbf{N}$ and the lapse function N. For this substitution, one uses general equations which relate the four dimensional curvature tensors to three-dimensional ones, such as the Codazzi equation. This derivation is outside the scope of this thesis, but can be found in [129] and [131], which results in

$$(\partial_t - \mathcal{L}_{\mathbf{N}})\, \gamma_{ab} = -2NK_{ab} \tag{184}$$

$$(\partial_t - \mathcal{L}_{\mathbf{N}})\, \gamma_{ab} = -D_a D_b N + N \left({}^{(3)}R_{ab} + KK_{ab} + 2K_{ai}K^i{}_b \right) \tag{185}$$

$$R + K^2 - K_{ab}K^{ab} = 0 \tag{186}$$

$$D_b K^b{}_a - D_a K = 0, \tag{187}$$

where D_a is the covariant derivative as defined on ${}^{(3)}\Sigma_t$. [27] Equations (184) and (185) are called the *dynamical Einstein Equations*, which give use information about how initial data evolves.[28] Equation (186) is called the *Hamiltonian constraint* and equation (187) is called the *momentum constraint*. [29] These constraint equations give conditions on γ_{ab}, K_{ab} for each spatial hypersurfaces, which need to be satisfied to be consistent with General Relativity.
Note that the system of equations (184) - (187) contains no time derivatives of the lapse function or shift vector. This implies that they are Lagrange multipliers, which means that they are not determined by these equations. The general covariance, as discussed in Section A.7.1, has been traded off for being able to arbitrarily choose the lapse and shift. Looking at Section A.4.3, this is not surprising, as the shift is a consequence of arbitrarily changing coordinates.

A.7.3 Dynamical Einstein equations and Cauchy solutions

Let us now consider the dynamical Einstein equations (184) - (185), which will tell us something about the development of Cauchy surfaces [129].
Note that the constraint equations (186) - (187) need to hold at every hypersurface ${}^{(3)}\Sigma_t$, but this does

[27] In these equations, we have assumed that there is a vacuum. However, it is possible to consider the non-vacuum case, since one can decompose the stress-energy tensor $T_{\mu\nu}$ [129].
[28] These dynamical equations for γ_{ab} and $\partial_t \gamma_{ab}$ are equivalent to dynamical equations of $g_{\mu\nu}$ given by $G_{ab} = 0$.
[29] The constraint equations for K are equivalent to the constraint equations of $g_{\mu\nu}$ given by $G_{0\mu} = 0$.

not mean that one needs to check at every hypersurface if it is satisfied. If the constraints are satisfied for ${}^{(3)}\Sigma_{t=0}$ and the dynamical Einstein Equations are satisfied creating "later" spatial hypersurfaces ${}^{(3)}\Sigma_t$, then the Bianchi identities ensure that the constraints are also satisfied at other hypersurfaces ${}^{(3)}\Sigma_t$.
A stronger variation of the previous question is called the Cauchy problem. Assuming that we have smooth initial data γ_{ab}, K_{ab} on a hypersurface ${}^{(3)}\Sigma_0$ that satisfy the constraint equations (186) - (187), is there a space-time (M, g) that satisfy the Einstein equations and embeds ${}^{(3)}\Sigma_0$ as hypersurface of M with induced metric γ_{ab} and extrinsic curvature K_{ab}. As Choquet-Bruhat and Geroch have shown, the answer is yes [133].
Before we can explain the Choquet-Bruhat and Geroch result, we will introduce some notation. Assume $({}^{(3)}\Sigma, \gamma_{ab}, K_{ab})$ satisfy the constraint equations (186) - (187). The triplet (M, g, i) is called a **Cauchy development**, when (M, g) is space-time that solves the Einstein equation and $i :^{(3)} \Sigma \to M$ is an embedding, such that $i({}^{(3)}\Sigma)$ is a Cauchy surface in M. This means that (M, g) is globally hyperbolic and allows us to foliate the space-time. We call such a Cauchy development **maximal** if for any other Cauchy development (M', g', i') of the initial data $({}^{(3)}\Sigma, \gamma_{ab}, K_{ab})$ there exists an embedding $\psi : M' \to M$, such that it preserves time orientation, the metric g (i.e. $\psi * g = g'$) and the Cauchy surface ${}^{(3)}\Sigma$ (i.e. $\psi \circ i' = i$). Maximal in this context does not mean that it Cauchy development is maximal as a solution to the Einstein equations, nor that there are any globally hyperbolic extensions of the space-time (M, g). It means that if there is an isometric embedding $\psi : M \to M''$ into a space-time (M'', g''), the embedding of ${}^{(3)}\Sigma$ in M'' is no longer a Cauchy surface in M''.
The theorem by Choquet-Bruhat and Geroch tells us that for each smooth initial data γ_{ab}, K_{ab} on a hypersurface ${}^{(3)}\Sigma_0$ that satisfy the constraint equations (186) - (187), there exists a maximal Cauchy development (M, g, i) which is unique up to time-orientation, metric and Cauchy preserving isometries [133].

This concludes the Appendix Section on the ADM formalism, since we have explained how and why we can create a four dimensional space-time (M, g) that satisfies the Einstein Equations from analysing γ_{ab}, K_{ab} on the initial time-slice ${}^{(3)}\Sigma_t$. We explained the relation between $\gamma_{ab}, K_{ab}, \mathbf{N}, N$ and $g_{\mu\nu}$ and showed that the lapse function and shift vector can be chosen arbitrarily. Lastly, we also showed what constraints the initial data γ_{ab}, K_{ab} should satisfy and their origin.[30]

[30] There is a larger context related to Quantum Gravity, which we have not fully touched on. The original goal was to create a Hamiltonian formalism of the Einstein-Hilbert action (182), for which one needed to define general velocities, which required a time coordinate [126]. This formalism was chronologically prior to the 3+1 formalism as we have discussed it, and some of the results derived from this Hamiltonian formalism translate to the formalism we use. For further reading, see [131] and [129].

B Second order calculations

In this section, one can find the second order calculations for the perturbation coefficients for the metric and extrinsic curvature. At second order, we take into account terms of the term L^4, L^3P, L^2P^2, LP^3 or P^4.

B.1 Conformal factor

Before we can calculate the second order metric perturbations, we need to calculate the conformal factor up to second order. Consider equation (55) for the conformal factor ϕ from Section 3.1.1. Note that we are only doing calculations up to L^4, P^4 or P^2L^2 and we are expanding the metric in Legendre Polynomials, which means that the terms that matter are (recall the metric has a term ϕ^4 appearing)

$$\begin{aligned}
&4\left(1+\frac{M}{2R}\right)^3\left(P^2L^{2\,(2)}\phi+\frac{ML^2}{8R^3}P_2\left[\cos(\theta)\right]+\frac{ML^4}{32R^5}P_4\left[\cos(\theta)\right]\right)\\
&+6\left(1+\frac{M}{2R}\right)^2\left(\frac{ML^2}{8R^3}P_2\left[\cos(\theta)\right]\right)^2+\left(1+\frac{M}{2R}\right)^4.
\end{aligned} \tag{188}$$

The extra coefficients in front of the terms are due to multiple crossterms contributing to the same term.

B.2 Metric coefficients

The goal is to express equation (188) in Legendre Polynomials. Specifically, we are considering $l = 2$, which means we can ignore the $P_4[\cos(\theta)]$ term as the Legendre polynomials form an orthogonal basis. The calculation will be done by using the previously given approximation, filling in ${}^{(2)}\phi$ from equation (45b) and consequently filling in R from equation (51). Using the approximation $\frac{R}{r} \approx \left(1+\frac{M}{2R}\right)^{-2}$, equation (188) becomes

$$\begin{aligned}
\left(\phi^4\frac{R^2}{r^2}\right)^{(l=2)} \approx& \left[4\left(1+\frac{M}{2R}\right)^{-1}\left(P^2L^{2\,(2)}\phi+\frac{ML^2}{8R^3}P_2\left[\cos(\theta)\right]+\frac{ML^4}{32R^5}P_4\left[\cos(\theta)\right]\right)\right.\\
&\left.+6\left(1+\frac{M}{2R}\right)^{-2}\left(\frac{ML^2}{8R^3}P_2\left[\cos(\theta)\right]\right)^2+1\right]^{(l=2)}\\
\approx& 4\frac{\sqrt{R}}{\sqrt{r}}\left(-\frac{8P^2L^2}{35}\frac{(M^4+10M^3R+40M^2R^2+80MR^3+80R^4)}{(2R+M)^5R^3} + \frac{q_2P^2L^2}{R^3}+\frac{ML^2}{8R^3}\right)\\
&+6\frac{R}{r}\frac{M^2L^4}{64R^6}\left(P_2\left[\cos(\theta)\right]^2\right)^{(l=2)}
\end{aligned}$$

$$
\begin{aligned}
&= -\frac{32P^2L^22^5}{35}\frac{(M^4+10M^3\left(\frac{(\sqrt{r}+\sqrt{r-2M})^2}{4}\right)+40M^2\left(\frac{(\sqrt{r}+\sqrt{r-2M})^2}{4}\right)^2)}{\sqrt{r}(\left(\frac{(\sqrt{r}+\sqrt{r-2M})^2}{2}\right)+M)^5(\sqrt{r}+\sqrt{r-2M})^5} \\
&- \frac{32P^2L^22^5}{35}\frac{(80M\left(\frac{(\sqrt{r}+\sqrt{r-2M})^2}{4}\right)^3+80\left(\frac{(\sqrt{r}+\sqrt{r-2M})^2}{4}\right)^4)}{\sqrt{r}(\left(\frac{(\sqrt{r}+\sqrt{r-2M})^2}{2}\right)+M)^5(\sqrt{r}+\sqrt{r-2M})^5} \\
&+ \frac{4q_2P^2L^22^5}{\sqrt{r}(\sqrt{r}+\sqrt{r-2M})^5}+\frac{ML^22^5}{2\sqrt{r}(\sqrt{r}+\sqrt{r-2M})^5}+\frac{3M^2L^42^{10}}{32r(\sqrt{r}+\sqrt{r-2M})^{10}}\frac{4}{35}\frac{5}{2} \qquad (189)\\
&= -\frac{32768P^2L^2}{35}\frac{\left[M^4+\frac{5}{2}M^3\left(\sqrt{r}+\sqrt{r-2M}\right)^2+\frac{5}{2}M^2\left(\sqrt{r}+\sqrt{r-2M}\right)^4\right]}{\sqrt{r}[(\sqrt{r}+\sqrt{r-2M})^2+2M]^5(\sqrt{r}+\sqrt{r-2M})^5} \\
&- \frac{32768P^2L^2}{35}\frac{\left[\frac{5}{4}M\left(\sqrt{r}+\sqrt{r-2M}\right)^6+\frac{5}{16}\left(\sqrt{r}+\sqrt{r-2M}\right)^8\right]}{\sqrt{r}[(\sqrt{r}+\sqrt{r-2M})^2+2M]^5(\sqrt{r}+\sqrt{r-2M})^5} \\
&+ \frac{128q_2P^2L^2}{\sqrt{r}(\sqrt{r}+\sqrt{r-2M})^5}+\frac{16ML^2}{\sqrt{r}(\sqrt{r}+\sqrt{r-2M})^5}+\frac{192M^2L^4}{7r(\sqrt{r}+\sqrt{r-2M})^{10}}
\end{aligned}
$$

B.2.1 Conclusion

We therefore conclude that

$$
\begin{aligned}
H_2^{(l=2)} = K^{(l=2)} &= -\frac{32768P^2L^2}{35}\frac{\left[M^4+\frac{5}{2}M^3\left(\sqrt{r}+\sqrt{r-2M}\right)^2\right]}{\sqrt{r}[(\sqrt{r}+\sqrt{r-2M})^2+2M]^5(\sqrt{r}+\sqrt{r-2M})^5} \\
&- \frac{32768P^2L^2}{35}\frac{\left[\frac{5}{2}M^2\left(\sqrt{r}+\sqrt{r-2M}\right)^4+\frac{5}{4}M\left(\sqrt{r}+\sqrt{r-2M}\right)^6+\frac{5}{16}\left(\sqrt{r}+\sqrt{r-2M}\right)^8\right]}{\sqrt{r}[(\sqrt{r}+\sqrt{r-2M})^2+2M]^5(\sqrt{r}+\sqrt{r-2M})^5} \qquad (190)\\
&+ \frac{128q_2P^2L^2}{\sqrt{r}(\sqrt{r}+\sqrt{r-2M})^5}+\frac{16ML^2}{\sqrt{r}(\sqrt{r}+\sqrt{r-2M})^5}+\frac{192M^2L^4}{7r(\sqrt{r}+\sqrt{r-2M})^{10}}.
\end{aligned}
$$

Note that the result in (190) differs from the exact form given in [57]. This is most likely due to coefficients being calculated there using a computer programme instead of by hand. Numerically checking the results shows that they give the same values for the coefficients.

B.3 Extrinsic curvature

As we have shown in Section 2.1.2, the extrinsic curvature in flat space time is

$$
\hat{K}_{ab}^{\text{tot}} = \frac{3PL}{2R^3}\begin{pmatrix} -4\cos(\theta)^2 & 0 & 0 \\ 0 & R^2\left[\cos(\theta)^2+1\right] & 0 \\ 0 & 0 & R^2\sin(\theta)^2[3\cos(\theta)^2-1] \end{pmatrix} + \frac{3PL^3}{16R^5}
\begin{pmatrix} -2\left[1-18\cos(\theta)^2+25\cos(\theta)^4\right] & -4R\sin(\theta)\cos(\theta)\left[-1+5\cos(\theta)^2\right] & 0 \\ \text{Sym} & R^2\left[-1-6\cos(\theta)^2+15\cos(\theta)^4\right] & 0 \\ 0 & 0 & R^2\left[3-33\cos(\theta)^2+65\cos(\theta)^4-35\cos(\theta)^6\right] \end{pmatrix}. \qquad (191)
$$

Let us consider only the second order part of the extrinsic curvature. Following the same procedure as in Section 3.2.1, we get

$$
\begin{aligned}
K_{ab}^{\text{tot}} &= -\frac{3PL^3}{16R^4 r} \\
&\begin{pmatrix} 2\left(\frac{dR}{dr}\right)^2[1-18\cos(\theta)^2+25\cos(\theta)^4] & 4R\frac{dR}{dr}\sin(\theta)\cos(\theta)[-1+5\cos(\theta)^2] & 0 \\ \text{Sym} & R^2[1+6\cos(\theta)^2-15\cos(\theta)^4] & 0 \\ 0 & 0 & R^2[-1+33\cos(\theta)^2-65\cos(\theta)^4+35\cos(\theta)^6] \end{pmatrix} \\
&= -\frac{3PL^3}{\left(\sqrt{r-2M}+\sqrt{r}\right)^4 r} \\
&\begin{pmatrix} \frac{2\left(25\cos(\theta)^4-18\cos(\theta)^2+1\right)}{r^2\left(1-\frac{2M}{r}\right)} & \frac{4\sin(\theta)\cos(\theta)\left(5\cos(\theta)^2-1\right)}{\sqrt{1-\frac{2M}{r}}\,r} & 0 \\ \frac{4\sin(\theta)\cos(\theta)\left(5\cos(\theta)^2-1\right)}{\sqrt{1-\frac{2M}{r}}\,r} & \left(-15\cos(\theta)^4+6\cos(\theta)^2+1\right) & 0 \\ 0 & 0 & \left(35\cos^6(\theta)-65\cos(\theta)^4+33\cos(\theta)^2-3\right) \end{pmatrix}
\end{aligned} \tag{192}
$$

B.3.1 Expanding the second order term of extrinsic curvature

So far, we have been able to find the coefficients for the perturbations by analysing linear sets of equations. However, for the terms of order PL^3 in equation (192) it is more efficient to use the (semi-) orthonormality of the set of Legendre Polynomials (see Appendix D)

$$\int_0^\pi f(\theta)P_n[\cos(\theta)]\sin(\theta)d\theta = c_n\frac{2}{2n+1}. \tag{193}$$

Now consider the $K_{r\theta}$ term. Note that in equation (60b) we have a derivative with respect to the angle θ, so we integrate the angle dependent part of $K_{r\theta}$

$$\int_0^\theta 4\sin(\theta)\cos(\theta)[-1+5\cos(\theta)^2]d\theta = -\frac{[-1+5\cos(\theta)^2]^2}{5}. \tag{194}$$

For $l=0$ we get

$$
\begin{aligned}
c_0 2 &= -\int_0^\pi \frac{3PL^3}{\left(\sqrt{r-2M}+\sqrt{r}\right)^4 r^{3/2}\sqrt{r-2M}}\frac{[-1+5\cos(\theta)^2]^2}{5}\sin(\theta)d\theta \\
&= -\frac{16L^3P}{5r^{\frac{3}{2}}\sqrt{r-2M}\left(\sqrt{r-2M}+\sqrt{r}\right)^4},
\end{aligned} \tag{195}
$$

which implies that

$$Kh_1^{(l=0)} = -\frac{8L^3P}{5r^{\frac{3}{2}}\sqrt{r-2M}\left(\sqrt{r-2M}+\sqrt{r}\right)^4}. \tag{196}$$

For $l = 2$, we have

$$\begin{aligned} c_2\frac{2}{5} &= -\int_0^{\pi} \frac{3PL^3}{\left(\sqrt{r-2M}+\sqrt{r}\right)^4 r^{3/2}\sqrt{r-2M}} \frac{[-1+5\cos(\theta)^2]^2}{5}\frac{1}{2}\left[3\cos^2(\theta)-1\right]\sin(\theta)d\theta \\ &= \frac{-3PL^3}{\left(\sqrt{r-2M}+\sqrt{r}\right)^4 r^{3/2}\sqrt{r-2M}}\frac{64}{105}. \end{aligned} \tag{197}$$

We therefore conclude

$$Kh_1^{(l=2)} = \frac{-PL^3}{\left(\sqrt{r-2M}+\sqrt{r}\right)^4 r^{3/2}\sqrt{r-2M}}\frac{32}{7}. \tag{198}$$

Now consider K_{rr}. Removing the $(1-2M/r)^{-1}$ factor from equation (63), because of the prefactor in equation (48e), we get for $l = 0$

$$c_0 2 = -\int_0^{\pi} \frac{3PL^3\left[2\left(25\cos(\theta)^4-18\cos(\theta)^2+1\right)\right]}{\left(\sqrt{r-2M}+\sqrt{r}\right)^4 r^3}\sin(\theta)d\theta = 0. \tag{199}$$

Equation (199) implies

$$KH_2^{(l=0)} = 0. \tag{200}$$

In the case that $l = 2$, we have

$$\begin{aligned} c_2\frac{2}{5} &= -\int_0^{\pi} \frac{3PL^3\left[2\left(25\cos(\theta)^4-18\cos(\theta)^2+1\right)\right]}{\left(\sqrt{r-2M}+\sqrt{r}\right)^4 r^3}\frac{1}{2}\left[3\cos^2(\theta)-1\right]\sin(\theta)d\theta \\ &= \frac{-3PL^3}{\left(\sqrt{r-2M}+\sqrt{r}\right)^4 r^3}\frac{64}{35}. \end{aligned} \tag{201}$$

We therefore conclude

$$KH_2^{(l=2)} = c_2\frac{5}{2} = \frac{-PL^3}{\left(\sqrt{r-2M}+\sqrt{r}\right)^4 r^3}\frac{96}{7}, \tag{202}$$

Now consider $KK_2^{(2)}(r,t)$, we have for $l = 0$

$$c_0 2 = -\int_0^{\pi} \frac{3PL^3\left[-15\cos(\theta)^4+6\cos(\theta)^2+1\right]}{\left(\sqrt{r-2M}+\sqrt{r}\right)^4 r^3}\sin(\theta)d\theta = 0, \tag{203}$$

implying

$$KK_2^{(l=0)} = 0, \tag{204}$$

In the case of $l = 2$, we have

$$\begin{aligned} c_2\frac{2}{5} &= -\int_0^{\pi} \frac{3PL^3\left[-15\cos(\theta)^4+6\cos(\theta)^2+1\right]}{\left(\sqrt{r-2M}+\sqrt{r}\right)^4 r^3}\frac{1}{2}\left[3\cos^2(\theta)-1\right]\sin(\theta)d\theta \\ &= \frac{3PL^3}{\left(\sqrt{r-2M}+\sqrt{r}\right)^4 r^3}\frac{64}{35}. \end{aligned} \tag{205}$$

This implies that

$$KK_2^{(l=2)} = c_2\frac{5}{2} = \frac{-PL^3}{\left(\sqrt{r-2M}+\sqrt{r}\right)^4 r^3}\frac{96}{7}. \tag{206}$$

Now consider $KG_2^{(l=2)}(r,t)$

$$\int_0^{\theta}\int_0^{\theta'}\left(-15\cos(\theta)^4+6\cos(\theta)^2+1\right)d\theta d\theta' = -\frac{9}{4}-\frac{(13\theta^2}{16}+\frac{21\cos(\theta)^2}{16}+\frac{15\cos(\theta)^4}{16}. \tag{207}$$

We get for $l=0$

$$\begin{aligned}c_0 2 &= -\int_0^{\pi}\frac{3PL^3}{\left(\sqrt{r-2M}+\sqrt{r}\right)^4 r^3}\left[-\frac{9}{4}-\frac{13\theta^2}{16}+\frac{21\cos(\theta)^2}{16}+\frac{15\cos(\theta)^4}{16}\right]\sin(\theta)d\theta \\ &= -\frac{39\pi^2L^3P}{16r^3\left(\sqrt{r-2M}+\sqrt{r}\right)^4},\end{aligned} \tag{208}$$

which implies that

$$KG_2^{(l=2)} = -\frac{39\pi^2L^3P}{32r^3\left(\sqrt{r-2M}+\sqrt{r}\right)^4}. \tag{209}$$

For $l=2$, we have

$$\begin{aligned}c_2\frac{2}{5} &= -\int_0^{\pi}\frac{3PL^3}{\left(\sqrt{r-2M}+\sqrt{r}\right)^4 r^3}\left[-\frac{9}{4}-\frac{(13\theta^2}{16}+\frac{21\cos(\theta)^2}{16}+\frac{15\cos(\theta)^4}{16}\right] \\ &\frac{1}{2}\left[3\cos^2(\theta)-1\right]\sin(\theta)d\theta \\ &= \frac{3PL^3}{\left(\sqrt{r-2M}+\sqrt{r}\right)^4 r^3}\frac{64}{315}.\end{aligned} \tag{210}$$

We then see

$$KG_2^{(l=2)} = c_2\frac{5}{2} = \frac{-PL^3}{\left(\sqrt{r-2M}+\sqrt{r}\right)^4 r^3}\frac{32}{21}, \tag{211}$$

B.3.2 Conclusion

We therefore conclude that

$$KH_2^{(l=0)}(r,t) = \frac{-2PL}{r^3} \tag{212a}$$

$$KH_2^{(l=2)}(r,t) = \frac{-4PL}{r^3}+\frac{-PL^3}{\left(\sqrt{r-2M}+\sqrt{r}\right)^4 r^3}\frac{96}{7} \tag{212b}$$

$$KG^{(l=0)}(r,t) = -\frac{39\pi^2L^3P}{32r^3\left(\sqrt{r-2M}+\sqrt{r}\right)^4} \tag{212c}$$

$$KG^{(l=2)}(r,t) = \frac{PL}{r^3} + \frac{-PL^3}{\left(\sqrt{r-2M}+\sqrt{r}\right)^4 r^3}\frac{32}{21} \tag{212d}$$

$$KK^{(l=0)}(r,t) = \frac{PL}{r^3} \tag{212e}$$

$$KK^{(l=2)}(r,t) = \frac{5PL}{r^3} + \frac{-PL^3}{\left(\sqrt{r-2M}+\sqrt{r}\right)^4 r^3}\frac{96}{7} \tag{212f}$$

$$Kh_1^{(l=0)} = -\frac{8L^3P}{5r^{\frac{3}{2}}\sqrt{r-2M}\left(\sqrt{r-2M}+\sqrt{r}\right)^4}. \tag{212g}$$

$$Kh_1^{(l=2)} = \frac{-PL^3}{\left(\sqrt{r-2M}+\sqrt{r}\right)^4 r^{3/2}\sqrt{r-2M}}\frac{32}{7} \tag{212h}$$

The results in (212) also differ from the exact form given in [57]. Numerically checking the results shows that both solutions give the same values for the coefficients. The difference is again most likely due to coefficients being calculated in [57] using a computer programme instead of by hand.

C Schwarzschild perturbations

There are two ways one can analyse black hole perturbations, either via the Newman Penrose formalism or via parameterizing the perturbations as variations of the metric and combining them with the (vacuum) Einstein Field Equations. Both methods lead to the same two sets of equations: the Regge-Wheeler equation and the Zerilli equation [34]. In this appendix, we will highlight the second method, since this form can be more easily combined with the ADM-formalism, as it uses coordinates.

C.1 Perturbation of the Schwarzschild metric

Let us consider a non-rotating zero charge black hole in a vacuum context where the cosmological constant is zero. The metric is given by Schwarzschild's solution to the Einstein Field Equations. The perturbations of the metric can be categorized into two kinds of perturbations: **axial** and **polar** perturbations.
The Schwarzschild solution can be written as a special form of a spherically symmetric time-independent metric that obeys the Einstein Field equations. Let us consider such a metric expressed in radial coordinate basis (t, r, θ, ϕ)

$$ds^2 = e^{2\nu}dt^2 - e^{2\mu_2}dr^2 - e^{2\mu_3}d\theta^2 - e^{2\psi}\left(-\omega dt - q_2 dr - q_3 d\theta + d\phi\right)^2. \tag{213}$$

When we consider the unperturbed Schwarzschild metric, we have

$$e^{2\nu} = e^{-2\mu_2} = 1 - \frac{2M}{r} \tag{214}$$

$$e^{\mu_3} = r \tag{215}$$

$$e^{\psi} = r\sin(\theta) \tag{216}$$

$$\omega = q_2 = q_3 = 0. \tag{217}$$

We introduce a new symbol to make our calculations more compact

$$\Delta := r^2 - 2Mr. \tag{218}$$

The perturbation of the metric leads to ω, q_2 and q_3 to take on small non-zero values, while the functions ν, μ_2, μ_3 and ψ get small increments. These can consequently be subdivided into **axial** (ω, q_2, q_3) and **polar** $(\delta\nu, \delta\mu_2, \delta\mu_3, \delta\psi)$ perturbations. The axial perturbations induce a "dragging" of the inertial frame. The polar perturbations don't create such a rotation. The axial perturbation will lead to the Regge-Wheeler equation, while the polar perturbations will lead to the Zerilli equation.
The Regge-Wheeler and Zerilli equations follow from the Einstein Equations, which are linearized about the unperturbed Schwarzschild space-time. The axial perturbations follow from

$$\delta R_{12} = 0 = \delta R_{13} \tag{219}$$

and the polar perturbations by

$$\delta R_{02} = 0 = \delta R_{03} = \delta R_{23} = \delta R_{11} = \delta G_{22}, \tag{220}$$

where $R_{\mu\nu}$ is the Ricci curvature tensor and $G_{\mu\nu}$ is the Einstein tensor. From the definition of these tensors and the metric given by equation (213) one gets equations given in ω, q_2 and q_3, and $\delta\nu, \delta\mu_2, \delta\mu_3$ and $\delta\psi$.

C.1.1 Polar perturbations

Let us consider polar perturbations, since these lead to the Zerilli equation. The full derivation can be found in the book by Chandrasekhar [34], in this part we will briefly highlight the steps made in between. Firstly, one assumes that the time-dependence of the perturbation is of the form $e^{i\sigma t}$, where $\sigma \in \mathbb{C}$. Then one assumes that there is a separation of variables between r and θ, such that the perturbations take the form

$$\delta\nu = N(r)P_l\left[\cos(\theta)\right]e^{i\sigma t} \tag{221}$$

$$\delta\mu_2 = L(r)P_l\left[\cos(\theta)\right]e^{i\sigma t} \tag{222}$$

$$\delta\mu_3 = \left(T(r)P_l\left[\cos(\theta)\right] + V(r)\partial_\theta^2 P_l\left[\cos(\theta)\right]\right)e^{i\sigma t} \tag{223}$$

$$\delta\psi = \left(T(r)P_l\left[\cos(\theta)\right] + V(r)\partial_\theta P_l\left[\cot(\theta)\right]\right)e^{i\sigma t}, \tag{224}$$

where $N(r), L(r), T(r)$ and $V(r)$ are functions of r and P_l is a Legendre polynomial of mode l. The similarity between equations (224) and (223) follows from equations (220) and the assumption of separation of variables. It is not an a priori assumption on the specific perturbations of the functions ψ and μ_3.
When filling in the equations (221) - (224) into equations (220), one is able to express the derivatives of the functions $N(r), L(r)$ and $V(r)$ as linear combinations of $N(r), L(r)$ and $V(r)$. As a consequence, one is able to reduce the equations to a one-dimensional wave equation which is satisfied by a wave equation of the form

$$Z^{(+)} = \frac{r^2}{\frac{1}{2}(l+2)(l-1)r + 3M}\left(\frac{3M}{r}V(r) - L(r)\right). \tag{225}$$

To express the wave equation, we need to introduce the **tortoise coordinate** r_*, which is defined by

$$r_* := r + 2M\log\left[\frac{r}{2M} - 1\right]. \tag{226}$$

Taking the time derivate of the perturbations is trivial due to the assumption that it of the form $e^{i\sigma t}$, which means that we can define an operator

$$\begin{aligned}\Lambda_\pm &:= \frac{d}{dr_*} \pm i\sigma \\ \Lambda^2 &= \Lambda_+\Lambda_- = \frac{d^2}{dr_*^2} + \sigma^2,\end{aligned} \tag{227}$$

such that equations (220) are reduced to

$$\Lambda^2 Z^+(r,t) = V^+(r)Z^+(r,t). \tag{228}$$

In equation (228), the V^+ is a potential, which is of the form

$$V^+(r) = \frac{2(r^2 - 2Mr)}{r^5(nr + 3M)^2}\left[n^2(n+1)r^3 + 3Mn^2r^2 + 9M^2nr + 9M^3\right], \tag{229}$$

where

$$n := \frac{1}{2}(l-1)(l+2). \tag{230}$$

Given l and M, one is able to express the solutions for $L(r), V(r)$ and $N(r)$ as a function of Z^+. For the functions $L(r)$ and $V(r)$, one gets a relatively simple form, namely

$$L(r) = \frac{-n}{r}Z^+ + \frac{3M}{r^2}\Xi \tag{231}$$

$$V(r) = \frac{1}{r}\left(Z^+ + \Xi\right) \tag{232}$$

where

$$\Xi := ne^{\nu}\int \frac{e^{\nu}Z^+}{nr+3M}dr. \tag{233}$$

The introduction of Ξ in equations (231) and (232) should not be surprising, since equations (220) are of third order, which were reduced to a second order problem for Z^+. For the function $N(r)$, one gets a significantly more difficult expression, namely

$$N(r) = \frac{-nr}{nr+3M}\partial_{r_*}Z^+ - \frac{nZ^+}{(nr+3M)^2}\left[\frac{6M^2}{r} + 3Mn + n(n+1)r\right] + \left[M - \frac{M^2+\sigma^2 r^4}{r-2M}\right]\frac{\Xi}{r^2}. \tag{234}$$

Let us reflect on the results so far. Note that in equation (234), we have a dependence on σ, which means that our assumption on the time-dependence has a direct effect on the form of the $r-$dependence of the perturbations. From the solutions for the functions $L(r), V(r)$ and $N(r)$, we conclude that perturbations are only well-defined if the Zerilli function Z^+ is smooth and the integral from equation (233) is well-defined. It is evident that this formulation is not gauge-invariant, since performing a gauge-transformation would change the coordinate system and therefore the way that the perturbations are defined and therefore the form of Z^+. This explains why there are multiple forms of the Zerilli equation (228), since the potential would also change.

C.1.2 Relations between polar and axial perturbations

Before concluding, , we will discuss the structural similarity between the polar and axial perturbations by considering their wave equations.
The polar and axial perturbations are separate perturbations, which are independent in the sense that the Einstein equations give two independent sets of equations that define the perturbations. Despite this independence, there is an underlying relation between the axial and polar perturbations, which will become important in the context of reflection and transmission of waves.
In Section C.1.1, we have denoted functions with a superscript +. In the case of axial perturbations, one is similarly able to define a function Z^-. The function Z^- also satisfies a wave equation, but with a potential of the form

$$V^- = \frac{2\Delta}{r^5}\left[(n+1)r - 6M\right]. \tag{235}$$

This implies that both equations can be written down as a one dimensional Schrödinger equation

$$\Lambda^2 Z^{\pm} = V^{\pm}Z^{\pm}, \tag{236}$$

where the + case denotes the Zerilli Equation and the − case denotes the Regge-Wheeler Equation.
Let us consider the potentials in equation (236). There is a relation between the two potential terms,[31] given by

$$V^{\pm} = \pm\beta\frac{df}{dr_*} + \beta^2 f^2 + \kappa f, \tag{237}$$

[31] This relation comes to light when one uses the Newman-Penrose formalism to discuss the perturbations. Since it is out of the scope of this thesis to discuss this formalism, one can find a derivation in the book by Chandrasekhar [34].

where

$$\beta = 6M \tag{238}$$
$$\kappa = 4n(n+1) \tag{239}$$
$$f = \frac{\Delta}{r^3(2nr + 6M)}. \tag{240}$$

Given l and M, we define the functions $p(r_*)$ and $q(r_*)$ such that

$$Z^+(r_*) = p(r_*)Z^-(r_*) + q(r_*)\partial_{r_*} Z^-(r_*). \tag{241}$$

Using the fact that $\partial^2_{r_*} Z^- = (V^- - \sigma^2)Z^-$, one can take the double derivative of Z^+ in equation (241) and compare it to equation (236) for the + case. One can then show that $p(r) = \kappa + 2\beta^2 f(r)$ and $q = 2\beta$, such that the relation between the $Z^\pm$ terms is given by

$$[4n(n+1) \pm 12i\sigma M]\, Z^\pm = \left[4n(n+1) + \frac{72M^2(r^2 - 2Mr)}{r^3(2nr + 6M)}\right] Z^\mp \pm 12M \frac{dZ^\mp}{dr_*}. \tag{242}$$

The consequence of this relation between Z^+ and Z^- is that one is able to construct an expression consisting of polar perturbations that satisfy the wave equation related to the axial perturbations.
Let us consider $Z^\pm$ in the context of reflection and transmission. For $f(r)$ in equation (237) we have $f(r_*) \to 0$ as $r_* \to \pm\infty$.[32] The potential $V^\pm$ therefore goes to zero for $r_* \to \pm\infty$ and falls of as

$$V^\pm \propto \begin{cases} r_*^{-2} & \text{when } r_* \to \infty \\ e^{r_*} & \text{when } r_* \to -\infty \end{cases} \tag{243}$$

The solution $Z^+(r_*)$ of equation (236) therefore has asymptotic behaviour

$$Z^- \propto \begin{cases} e^{i\sigma r_*} & \text{when } r_* \to \infty \\ e^{-i\sigma r_*} & \text{when } r_* \to -\infty. \end{cases} \tag{244}$$

Using equation (241), we conclude that

$$Z^+ \propto \begin{cases} e^{i\sigma r_*} & \text{when } r_* \to \infty \\ \dfrac{\kappa - 2i\sigma\beta}{\kappa + 2i\sigma\beta} e^{-i\sigma r_*} & \text{when } r_* \to -\infty. \end{cases} \tag{245}$$

This implies the amplitude of the transmitted waves are identically the same for when one considers $V^\pm$, while the reflected amplitudes differ by a phase.

C.2 quasi-normal modes

Quasi-Normal Modes (QNMs) are characteristic solutions to the linearized Einstein equations which decay over time due to the emission of gravitational waves. It describes the exponential decrease of asymmetry of the final black hole as it starts to resemble a perfect spherical shape. They are used to analyse the merging of the black hole by analysing the signal.
Consider a perturbation of a black hole. This can be due to an object falling into the black hole, a merger, etc. Any perturbation will decay in the final stages in a way that is characteristic to the black hole, but independent of the original cause of the perturbation. The gravitational waves from the last stages will therefore have frequencies and rates of damping, which we can use to characterise the black hole.

[32] The condition $r_* \to -\infty$ is equivalent to $r \to 2M$ and $r_* \to +\infty$ is equivalent to $r \to +\infty$

C.2.1 Mathematical description

In general, quasi-normal modes (QNMs) are a solution to a linearized differential equation with a complex eigenvalue. This means that they are the modes of energy dissipation of a perturbed object. The quasi-normal modes are also called the "pure tones" of a black hole.
Let us consider the wave functions $Z^{\pm}$ from Section C.1. Quasi-normal modes satisfy purely outgoing waves at infinity and purely ingoing waves at the horizon, meaning

$$Z^{\pm} \to \begin{cases} A^{\pm} e^{-i\sigma r} & \text{for } r_* \to \infty \\ e^{-i\sigma r} & \text{for } r_* \to -\infty, \end{cases} \tag{246}$$

where $\sigma \in \mathbb{C}$ is the same σ from the time-dependence, i.e. $e^{i\sigma t}$. Since $\sigma \in \mathbb{C}$, it is clear that $\mathrm{Re}[\sigma]$ denotes the temporal oscillation, while $\mathrm{Im}[\sigma]$ denotes whether the signal dampens or grows over time. In this context, we only have damped stable QNMs, which correspond to $\mathrm{Im}[\sigma] < 0$. The QNM with the largest imaginary part is called the **fundamental mode**. This is the **pure note**, as this mode has the smallest damping, which means that it is the only mode that is visible after a while.
From Section C.1.2, we saw that the transmitted amplitudes for the $+$ and $-$ case are the same, while the reflected amplitudes have only a phase-difference. It is therefore sufficient to analyse the Z^+ case (the Zerilli case), since

$$A^- = A^+ \frac{n(n+1) + 3\sigma M i}{n(n+1) - 3\sigma M i}. \tag{247}$$

In this thesis, we analyse the Zerilli equation, since the close limit approximation gives us initial data about the even parity sector. This means that the initial data is more easily related to the Zerilli function. We will therefore only discuss the Zerilli equation in the next sections.

C.2.2 Calculating the quasi-normal modes

There are multiple ways to calculate quasi-normal modes; the Mashoon method which approximates the Zerilli equation with the Pöschl-Teller equation; the WKB method which uses asymptotic WKB solutions at $r_* \to \pm\infty$ with a Taylor expansion near the top of the potential barrier through two turning points, and many more [134]. In this section, we will shortly discuss the Chandrasekhar-Detweiler and shooting methods.
Consider Z^+ from Section C.1.1, in this case we write

$$Z^+(r_*) = e^{i\int^{r_*} \xi(r')dr'}. \tag{248}$$

Filling in equation (248) into (228), we see that we get a non-linear eigenvalue problem for $\xi(r_*)$ of the form

$$\frac{d\xi(r_*)}{dr_*} + \sigma^2 - \xi(r_*)^2 - V^+(r_*) = 0, \tag{249}$$

which is called the Ricatti equation. From equation (246), we see that the boundary conditions for $\phi(r_*)$ are given by

$$\xi(r_*) = -\sigma \qquad \text{for } r_* \to \infty \tag{250}$$

$$\xi(r_*) = -\sigma \qquad \text{for } r_* \to -\infty \tag{251}$$

Solutions for ξ only exist when σ takes values from a discrete set of values. One would normally integrate the Riccati equation numerically.
One such way is called the shooting method. Take a $\sigma \in \mathbb{C}$, such that $Z^+ \propto e^{i\sigma r_*}$ for $r_* \to \pm\infty$. One would

integrate Z^+ from infinity to an intermediate value r_*^{fixed}, and integrate Z^+ from the horizon to r_*^{fixed}. The Wronskian of the two solutions vanishes, which gives one an equation for quasi-normal modes. Note however that at second order, the solution gets contaminated at the horizon and far away, making it only useful for lower modes.

In this thesis, we do not explicitly calculate the initial data, but fit our data to already calculated quasi-normal modes. We start with the data of the wave function at $t = 0$ for each r_*, which includes the horizon and some point far away. Using the Zerilli function and a solver, we evolve the initial data. Next, we extract the data for the wave function at the horizon and far away as a function of time. We then fit the data using Mathematica code to $A^+_{lm}e^{i\sigma_{lm}t}$, where the quasi-normal modes σ_{lm} are given by the theory (such as the shooting method described above). The values for σ_{lm} gets imported via the QNM package for Mathematica. We fit the coefficients for the different QNMs and sees if there is a redshift between the QNMs at the horizon and far away. The idea is to specifically look at the pure note and the fundamental mode.

D Legendre polynomials

In this thesis, we use Legendre Polynomials to expand our initial data into the Regge-Wheeler formalism, which can consequently be used to define the Zerilli function. In this appendix, we will shortly introduce the concept behind the Legendre Polynomials and show some useful relations.
The definitions of the Legendre Polynomials is given by

$$\frac{1}{\sqrt{1-2xt+u^2}} = \sum_{n=0}^{\infty} P_n[x]u^n. \tag{252}$$

For this thesis, we only need to consider the Legendre Polynomials with $x = \cos(\theta)$ up to $l = 4$, which are

$$\begin{aligned}
P_0[\cos(\theta)] &= 1 \\
P_2[\cos(\theta)] &= \frac{1}{2}\left[3\cos^2(\theta) - 1\right] \\
P_4[\cos(\theta)] &= \frac{1}{8}\left[35\cos^4(\theta) - 30\cos^2(\theta) + 3\right]
\end{aligned}$$

As a consequence, we find

$$\cos^2\theta = \frac{1}{3}P_0(\cos\theta) + \frac{2}{3}P_2(\cos\theta) \tag{253}$$

$$\cos^4\theta = \frac{1}{5}P_0(\cos\theta) + \frac{4}{7}P_2(\cos\theta) + \frac{8}{35}P_4(\cos\theta), \tag{254}$$

which we use in Section 3.
The set of Legendre Polynomials has a (semi-) orthonormality condition, given by

$$\int_{-1}^{1} P_m(x)P_n(x)\,dx = \frac{2}{2n+1}\delta_{mn}. \tag{255}$$

This implies that if we expand a function in Legendre polynomials, we get

$$\begin{aligned}
\int_{-1}^{1} f(x)P_n[x]dx &= \int_{-1}^{1} \sum_m c_m P_m\left[\cos(\theta)\right] P_n[\cos(\theta)] d\cos(\theta) \\
&= \sum_m \int_0^{\pi} c_m P_m\left[\cos(\theta)\right] P_n[\cos(\theta)] \sin(\theta) d\theta = c_n \frac{2}{2n+1}.
\end{aligned} \tag{256}$$

We use this relation to calculate the metric perturbation coefficients at second order and to verify the results at first order.

E Checking initial data

One potential way to deal with the divergence in our solution is by creating a check for the constructed initial data. In this Appendix, we will lay the groundwork for such a check. Due to time constraints, this has not been implemented yet.
We assume that the original function at $t = 0$ satisfies the separation of variables $\psi(r,t) = \psi_1(r)\psi_2(t)$. The Zerilli equation than becomes

$$\begin{aligned} &- \psi_1(r)\frac{\partial^2\psi_2(t)}{\partial t^2} + \psi_2(t)\frac{\partial^2\psi_1(r)}{\partial r_*^2} - V(r)\psi_1(r)\psi_2(t) = 0 \\ &= -\frac{1}{\psi_2(t)}\frac{\partial^2\psi_2(t)}{\partial t^2} + \frac{1}{\psi_1(r)}\frac{\partial^2\psi_1(r)}{\partial r_*^2} - V(r). \end{aligned} \tag{257}$$

Assume that the time component takes the form

$$\psi_2(t) = e^{-i\omega t}, \tag{258}$$

where $\omega \in \mathbb{C}$. Equation (257) therefore becomes

$$\begin{aligned} &- (-i\omega)^2 e^{i\omega t}e^{-i\omega t} + \frac{1}{\psi_1(r)}\frac{\partial^2\psi_1(r)}{\partial r_*^2} - V(r) = 0. \\ &\frac{1}{\psi_1(r)}\frac{\partial^2\psi_1(r)}{\partial r_*^2} = V(r) - \omega^2 \end{aligned} \tag{259}$$

As we have already shown in Section 4, we have

$$\tilde{H}_2 = \frac{16L^2M}{\sqrt{r}\left(\sqrt{r-2M}+\sqrt{r}\right)^5} \tag{260}$$

$$\tilde{K} = \frac{16L^2M}{\sqrt{r}\left(\sqrt{r-2M}+\sqrt{r}\right)^5}, \tag{261}$$

which implies that

$$\partial_r\tilde{K} = -\frac{16L^2M\left(\sqrt{r-2M}+5\sqrt{r}\right)}{2r^{3/2}\sqrt{r-2M}\left(\sqrt{r-2M}+\sqrt{r}\right)^5}. \tag{262}$$

The Gauge invariant Zerilli function (87) is then given by

$$\begin{aligned} \psi &= \frac{r}{3}\left\{\frac{16L^2M}{\sqrt{r}\left(\sqrt{r-2M}+\sqrt{r}\right)^5} + \frac{2}{\Lambda}\left[\left(1-\frac{2M}{r}\right)^2\frac{16L^2M}{\sqrt{r}\left(\sqrt{r-2M}+\sqrt{r}\right)^5} - r\left(1-\frac{2M}{r}\right)\partial_r\frac{16L^2M}{\sqrt{r}\left(\sqrt{r-2M}+\sqrt{r}\right)^5}\right]\right\} \\ &= \frac{r}{3}\left\{\frac{16L^2M}{\sqrt{r}\left(\sqrt{r-2M}+\sqrt{r}\right)^5} + \frac{1}{2+\frac{3M}{r}}\left[\frac{16L^2M\left(1-\frac{2M}{r}\right)^2}{\sqrt{r}\left(\sqrt{r-2M}+\sqrt{r}\right)^5} + \frac{16L^2M\sqrt{r-2M}\left(\sqrt{r-2M}+5\sqrt{r}\right)}{2r^{3/2}\left(\sqrt{r-2M}+\sqrt{r}\right)^5}\right]\right\}, \end{aligned} \tag{263}$$

with $\Lambda = (l-1)(l+2) + \frac{6M}{r} = 4 + \frac{6M}{r}$
Changing the coordinate system back to (t, r, θ, ϕ), substituting equation (83) into equation (259) we get

$$\begin{aligned} V(r) - \omega^2 &= \frac{1}{\psi_1(r)}\left(1 - \frac{2M}{r}\right)^2 \frac{\partial^2 \psi_1(r)}{\partial r^2} - \frac{1}{\psi_1(r)}\left(1 - \frac{2M}{r}\right)\frac{2M}{r^2}\frac{\partial \psi_1(r)}{\partial r} \\ &= \frac{\left(1 - \frac{2M}{r}\right)}{\left(4 + \frac{6M}{r}\right)^2}\left\{16\left[\frac{6}{r^2} + \frac{6M}{r^3}\right] + \frac{36M^2}{r^4}\left[4 + \frac{2M}{r}\right]\right\} - \omega^2 \end{aligned} \tag{264}$$

The $r-$derivatives of the Zerilli function are given by

$$\begin{aligned} \partial_r \psi = & \frac{16L^2M\left(\sqrt{r-2M} - 5\sqrt{r}\right)}{2\sqrt{r}\sqrt{r-2M}\left(\sqrt{r-2M}+\sqrt{r}\right)^5} - \frac{8L^2M\sqrt{r-2M}\left(10r^{\frac{7}{2}} + \sqrt{r-2M}\left(2r^3 - 23Mr^2 - 18M^2r\right) - 5Mr^{\frac{5}{2}} - 30M^2r^{\frac{3}{2}}\right)}{r^{\frac{7}{2}}\left(2r+3M\right)^2\left(\sqrt{r-2M}+\sqrt{r}\right)^5} \\ & - 4L^2M\left[\frac{-10r^{\frac{7}{2}} + \sqrt{r-2M}\left(46r^3 + 69Mr^2\right) - 15Mr^{\frac{5}{2}} + (r-2M)^{\frac{3}{2}}\left(6r^2 + 3Mr\right)}{r^{\frac{5}{2}}\sqrt{r-2M}\left(2r+3M\right)^2\left(\sqrt{r-2M}+\sqrt{r}\right)^5}\right. \\ & \left. + \frac{r\left(60M^2\sqrt{r} - 15Mr^{\frac{3}{2}}\right) + r^2\left(30r^{\frac{3}{2}} - 30M\sqrt{r}\right) - 90M^2r^{\frac{3}{2}}}{r^{\frac{5}{2}}\sqrt{r-2M}\left(2r+3M\right)^2\left(\sqrt{r-2M}+\sqrt{r}\right)^5}\right] \end{aligned} \tag{265}$$

and

$$\begin{aligned} \partial_r^2 \psi = & -\frac{4L^2M\left((r-2M)^{\frac{3}{2}} - 25r\sqrt{r-2M} - 10M\sqrt{r}\right)}{r^{\frac{3}{2}}(r-2M)^{\frac{3}{2}}\left(\sqrt{r-2M}+\sqrt{r}\right)^5} + 4L^2M\left[\frac{\sqrt{r-2M}\left(92r^5 + 180Mr^4 - 165M^2r^3 - 342M^3r^2\right)}{r^{\frac{9}{2}}\sqrt{r-2M}\left(2r+3M\right)^3\left(\sqrt{r-2M}+\sqrt{r}\right)^5}\right. \\ & + \frac{r\left(80r^{\frac{9}{2}} - 230Mr^{\frac{7}{2}} - 695M^2r^{\frac{5}{2}} + 120M^3r^{\frac{3}{2}} + 540M^4\sqrt{r}\right) - 230Mr^{\frac{9}{2}}}{r^{\frac{9}{2}}\sqrt{r-2M}\left(2r+3M\right)^3\left(\sqrt{r-2M}+\sqrt{r}\right)^5} \\ & + \frac{(r-2M)^{\frac{3}{2}}\left(20r^4 - 316Mr^3 - 531M^2r^2 - 270M^3r\right) + 495M^2r^{\frac{7}{2}}}{r^{\frac{9}{2}}\sqrt{r-2M}\left(2r+3M\right)^3\left(\sqrt{r-2M}+\sqrt{r}\right)^5} \\ & \left. + \frac{r^2\left(-20Mr^{\frac{5}{2}} - 240M^2r^{\frac{3}{2}} - 270M^3\sqrt{r}\right) + 1680M^3r^{\frac{5}{2}} + 720M^4r^{\frac{3}{2}}}{r^{\frac{9}{2}}\sqrt{r-2M}\left(2r+3M\right)^3\left(\sqrt{r-2M}+\sqrt{r}\right)^5}\right] \\ & - \frac{2L^2\left((r-2M)^{\frac{5}{2}} + 21r(r-2M)^{\frac{3}{2}} - 120r^{\frac{5}{2}} + 240Mr^{\frac{3}{2}} + 50r\sqrt{r-2M}\,(r-M) + 20M^2\sqrt{r}\right)}{9r^{\frac{3}{2}}(r-2M)^{\frac{3}{2}}\left(\sqrt{r-2M}+\sqrt{r}\right)^5}. \end{aligned} \tag{266}$$

Equations (265) and (266) can be substituted into (264) to check if they solve the equation for different values of r (akin to what was done for the Pöschl-Teller equation). This can be done by calculating the $r-$derivatives numerically in the code or using the explicit formulations in equations (265) and (266).

Acknowledgements

This thesis would not have been possible without the help of my supervisors Béatrice Bonga and Badri Krishnan and I would like to thank them for their support and explanations. I would also like to thank Tom van der Steen, for our many discussions, sanity checks and coffee breaks. Lastly, this thesis would not have been possible without the many meetings and discussions with PhD candidates Stamatis Vretinaris and Ariadna Ribes. Thank you all for the support.

References

[1] C. W. Misner, K. S. Thorne, and J. A. Wheeler, *Gravitation* (W. H. Freeman, San Francisco, 1973), 1279 pp.

[2] A. Einstein, "Die Grundlage der allgemeinen Relativitätstheorie", Annalen der Physik **354**, 769–822 (1916).

[3] R. S. Park, W. M. Folkner, A. S. Konopliv, et al., "Precession of mercury's perihelion from ranging to the messenger spacecraft", The Astronomical Journal **153**, 121 (2017).

[4] F. W. Dyson, A. S. Eddington, and C. Davidson, "A determination of the deflection of light by the sun's gravitational field, from observations made at the total eclipse of may 29, 1919", Philosophical Transactions of the Royal Society of London. Series A, Containing Papers of a Mathematical or Physical Character **220**, 291–333 (1920).

[5] D. M. Popper, "Red shift in the spectrum of 40 eridani b.", The Astrophysical Journal **120**, 316 (1954).

[6] M. Kramer and M. M. 9. Jodrell Bank Centre for Astrophysics University of Manchester, "Tests of general relativity", AIP Conference Proceedings **1381**, `10.1063/1.3635826` (2011).

[7] R. H. Dicke, "New research on old gravitation", Science **129**, 621–624 (1959).

[8] L. I. Schiff, "On experimental tests of the general theory of relativity", American Journal of Physics **28**, 340–343 (1960).

[9] W. Kündig, "Measurement of the transverse doppler effect in an accelerated system", Physical Review **129**, 2371–2375 (1963).

[10] I. Ciufolini, A. Paolozzi, E. C. Pavlis, et al., "A test of general relativity using the lares and lageos satellites and a grace earth gravity model", The European Physical Journal. C, Particles and Fields **76** (2016).

[11] J.-P. Uzan, "The fundamental constants and their variation: observational and theoretical status", Reviews of Modern Physics **75**, 403–455 (2003), arXiv:`hep-ph/0205340 [hep-ph]`.

[12] Event Horizon Telescope Collaboration, K. Akiyama, A. Alberdi, et al., "First M87 Event Horizon Telescope Results. I. The Shadow of the Supermassive Black Hole", The Astrophysical Journal Letters **875**, L1, L1 (2019), arXiv:`1906.11238 [astro-ph.GA]`.

[13] B. P. Abbott, R. Abbott, T. D. Abbott, et al. (The LIGO Scientific Collaboration and the Virgo Collaboration), "Tests of general relativity with the binary black hole signals from the ligo-virgo catalog gwtc-1", Phys. Rev. D **100**, 104036 (2019).

[14] R. A. Hulse and J. H. Taylor, "A high-sensitivity pulsar survey", The Astrophysical Journal **191** (1974).

[15] J. H. Taylor and J. M. Weisberg, "A new test of general relativity - gravitational radiation and the binary pulsar psr 1913 16", The Astrophysical Journal Letters **253**, 908–920 (1982).

[16]A. Kembhavi and P. Khare, "Evidence for the existence of gravitational waves: the binary pulsar", in *Gravitational waves: a new window to the universe* (Springer Singapore, Singapore, 2020), pp. 83–91.

[17]B. P. Abbott, R. Abbott, T. D. Abbott, et al. (LIGO Scientific Collaboration and Virgo Collaboration), "Observation of gravitational waves from a binary black hole merger", Phys. Rev. Lett. **116**, 061102 (2016).

[18]M. Branchesi, M. Maggiore, D. Alonso, et al., "Science with the einstein telescope: a comparison of different designs", Journal of Cosmology and Astroparticle Physics **2023** (2023).

[19]L. C. W. W. Group, N. Afshordi, S. Akccay, et al., "Waveform modelling for the laser interferometer space antenna", in (2023).

[20]M. Bailes, B. K. Berger, P. R. Brady, et al., "Gravitational-wave physics and astronomy in the 2020s and 2030s", Nature Reviews Physics **3**, Publisher: Nature Publishing Group, 344–366 (2021).

[21]C. Misner, K. Thorne, J. Wheeler, et al., *Gravitation* (Princeton University Press, 2017).

[22]R. M. Wald, *General relativity* (University of Chicago Press, Chicago, 1984), 491 pp.

[23]L. S. Finn and K. S. Thorne, "Gravitational waves from a compact star in a circular, inspiral orbit, in the equatorial plane of a massive, spinning black hole, as observed by lisa", Physical Review D **62**, `10.1103/physrevd.62.124021` (2000).

[24]P. Schmidt, "Gravitational waves from binary black hole mergers: modeling and observations", Frontiers in Astronomy and Space Sciences **7**, `10.3389/fspas.2020.00028` (2020).

[25]E. Abdikamalov, G. Pagliaroli, and D. Radice, "Gravitational waves from core-collapse supernovae", in *Handbook of gravitational wave astronomy* (Springer Singapore, 2021), pp. 1–37.

[26]C. Caprini and D. G. Figueroa, "Cosmological backgrounds of gravitational waves", Classical and Quantum Gravity **35**, 163001 (2018).

[27]A. Hanslmeier, *The sun and space weather*, Astrophysics and Space Science Library (Springer Netherlands, 2007).

[28]Q. Remy, I. A. Grenier, D. J. Marshall, et al., "Cosmic rays, gas and dust in nearby anticentre clouds. i. co-to-h$_2 conversion factors and dust opacities$", Astronomy and Astrophysics **601**, A78, A78 (2017), arXiv:`1703.05237 [astro-ph.HE]`.

[29]M. C. Miller and N. Yunes, *Gravitational waves in physics and astrophysics*, 2514-3433 (IOP Publishing, 2021).

[30]F. Pretorius, *Binary black hole coalescence*, 2007, arXiv:`0710.1338 [gr-qc]`.

[31]S. R. Olsen, "Discovering and characterizing binary black hole merger signals with new methods in gravitational wave data analysis", English, Copyright - Database copyright ProQuest LLC; ProQuest does not claim copyright in the individual underlying works; Last updated - 2023-03-10, PhD thesis (Princeton University, 2023), p. 278.

[32]C. D. Capano, M. Cabero, J. Westerweck, et al., "Multimode Quasinormal Spectrum from a Perturbed Black Hole", Physical Review Letter **131**, 221402, 221402 (2023), arXiv:`2105.05238 [gr-qc]`.

[33]K. D. Kokkotas and B. Schmidt, "Quasi-normal modes of stars and black holes", Living Reviews in Relativity **2** (1999).

[34]S. Chandrasekhar, *The mathematical theory of black holes* (Clarendon Press, 1983).

[35]J. B. Hartle, *Gravity: an introduction to einstein's general relativity* (Cambridge University Press, 2021).

[36]J. Blackman, "Surrogate models of gravitational waves from numerical relativity simulations of binary black hole mergers", English, ProQuest Dissertations and Theses, Copyright - Database copyright ProQuest LLC; ProQuest does not claim copyright in the individual underlying works; Last updated - 2024-09-23, 235 (2017).

[37]E. Gourgoulhon, "Numerical relativity: solving einstein's equations on the computer", Classical and Quantum Gravity **28**, 229002 (2011).

[38]C. Palenzuela, "Introduction to numerical relativity", Frontiers in Astronomy and Space Sciences **7**, `10.3389/fspas.2020.00058` (2020).

[39]Z. Wang, J. Zhao, and Z. Cao, *Accuracy of numerical relativity waveforms with respect to space-based gravitational wave detectors*, 2024, arXiv:`2401.15331 [gr-qc]`.

[40]V. Kreinovich, "Astronomical tests of relativity: beyond parameterized post-newtonian formalism (ppn), to testing fundamental principles", Proceedings of the International Astronomical Union **5**, 56–61 (2009).

[41]L. Blanchet, *Post-newtonian theory for gravitational waves*, Feb. 7, 2024, arXiv:`1310.1528[gr-qc]`.

[42]T. Damour, "Gravitational scattering, post-minkowskian approximation, and effective-one-body theory", Phys. Rev. D **94**, 104015 (2016).

[43]G. U. Jakobsen, G. Mogull, J. Plefka, et al., "Conservative scattering of spinning black holes at fourth post-minkowskian order.", Physical review letters **131 15**, 151401 (2023).

[44]Y.-B. Bae, Y.-H. Hyun, and G. Kang, *Ringdown gravitational waves from close scattering of two black holes*, 2023, arXiv:`2310.18686 [gr-qc]`.

[45]M. A. Scheel, M. Boyle, T. Chu, et al., "High-accuracy waveforms for binary black hole inspiral, merger, and ringdown", Physical Review D **79**, Publisher: American Physical Society, 024003 (2009).

[46]T. Damour, "The general relativistic two body problem and the effective one body formalism", in *General relativity, cosmology and astrophysics* (Springer International Publishing, 2014), pp. 111–145.

[47]L. Pompili, A. Buonanno, and M. Pürrer, *Accounting for numerical-relativity calibration uncertainty in gravitational-wave modeling and inference*, 2024, arXiv:`2410.16859 [gr-qc]`.

[48]C. M. Will, "On the unreasonable effectiveness of the post-newtonian approximation in gravitational physics", Proceedings of the National Academy of Sciences **108**, Publisher: Proceedings of the National Academy of Sciences, 5938–5945 (2011).

[49]S. Bhagwat, M. Okounkova, S. W. Ballmer, et al., "On choosing the start time of binary black hole ringdowns", Physical Review D **97**, Publisher: American Physical Society, 104065 (2018).

[50]Gleiser, Nicasio, Price, et al., "Colliding black holes: how far can the close approximation go?", Physical review letters **77 22**, 4483–4486 (1996).

[51]R. H. Price and J. Pullin, "Colliding black holes: the close limit", Physical Review Letters **72**, 3297–3300 (1994).

[52]J. Baker, A. Abrahams, P. Anninos, et al., "Collision of boosted black holes", Physical Review D **55**, 829–834 (1997).

[53]Z. Andrade and R. H. Price, "Head-on collisions of unequal mass black holes: close-limit predictions", Physical Review D **56**, 6336–6350 (1997).

[54]A. M. Abrahams and R. H. Price, "Black-hole collisions from brill-lindquist initial data: predictions of perturbation theory", Physical Review D **53**, 1972–1976 (1996).

[55]R. Gleiser, C. Nicasio, R. Price, et al., “Gravitational radiation from schwarzschild black holes: the second order perturbation formalism”, Physics Reports **325**, 41–81 (2000), arXiv:`gr-qc/9807077`.

[56]R. J. Gleiser, O. Nicasio, R. H. Price, et al., “Collision of boosted black holes: second order close limit calculations”, Physical Review D **59**, 044024 (1998).

[57]C. O. Nicasio, R. J. Gleiser, R. H. Price, et al., “Collision of boosted black holes: second order close limit calculations”, Physical Review D **59**, `10.1103/physrevd.59.044024` (1999).

[58]C. O. Nicasio, R. Gleiser, and J. Pullin, “Second order perturbations of a schwarzschild black hole: inclusion of odd parity perturbations”, General Relativity and Gravitation **32**, 2021–2042 (2000).

[59]K. Ioka and H. Nakano, “Second- and higher-order quasinormal modes in binary black-hole mergers”, Physical Review D **76**, 061503 (2007).

[60]L. Annulli, “Close limit approximation for modified gravity: scalar instabilities in binary black hole spacetimes”, Physical Review D **104**, 124028 (2021).

[61]L. Annulli, V. Cardoso, and L. Gualtieri, “Applications of the close-limit approximation: horizonless compact objects and scalar fields”, Classical and Quantum Gravity **39**, 105005 (2022), arXiv:`2104.11236[astro-ph,physics:gr-qc,physics:hep-th]`.

[62]P. Mourier, X. Jiménez Forteza, D. Pook-Kolb, et al., “Quasinormal modes and their overtones at the common horizon in a binary black hole merger”, Physical Review D **103**, `10.1103/physrevd.103.044054` (2021).

[63]K. A. Dennison, T. W. Baumgarte, and H. P. Pfeiffer, “Approximate initial data for binary black holes”, Physical Review D **74**, `10.1103/physrevd.74.064016` (2006).

[64]J. M. Bowen and J. W. York, “Time-asymmetric initial data for black holes and black-hole collisions”, Physical Review D **21**, Publisher: American Physical Society, 2047–2056 (1980).

[65]T. van de Steen, “The second order close limit approximation, towards exploring nonlinear behaviour at the horizon”, PhD thesis (Radboud University, 2023).

[66]D. R. Brill and R. W. Lindquist, “Interaction Energy in Geometrostatics”, Physical Review **131**, Publisher: American Physical Society, 471–476 (1963).

[67]T. Regge and J. A. Wheeler, “Stability of a Schwarzschild Singularity”, Physical Review **108**, Publisher: American Physical Society, 1063–1069 (1957).

[68]J. Baker, A. Abrahams, P. Anninos, et al., “Collision of boosted black holes”, Physical Review D **55**, 829–834 (1997).

[69]K. Martel and E. Poisson, “Gravitational perturbations of the schwarzschild spacetime: a practical covariant and gauge-invariant formalism”, Phys. Rev. D **71**, 104003 (2005).

[70]K. Martel, “Particles and black holes: time-domain integration of the equations of black-hole perturbation theory”, PhD thesis (University of Guelph (Canada), 2004).

[71]F. J. Zerilli, “Effective potential for even parity regge-wheeler gravitational perturbation equations”, Physical Review Letters **24**, 737–738 (1970).

[72]R. J. Gleiser, C. O. Nicasio, R. H. Price, et al., “Gravitational radiation from schwarzschild black holes: the second-order perturbation formalism”, Physics Reports **325**, 41–81 (1998).

[73]G. Dziuk, C. Lubich, and D. Mansour, “Runge–kutta time discretization of parabolic differential equations on evolving surfaces”, Ima Journal of Numerical Analysis **32**, 394–416 (2012).

[74]P. J. Houwen and van der, “The development of runge-kutta methods for partial differential equations”, Applied Numerical Mathematics **20**, 261–272 (1996).

[75]A. Ostermann and M. Roche, “Runge-kutta methods for partial differential equations and fractional orders of convergence”, Mathematics of Computation **59**, 403–420 (1992).

[76]A. Kumar and T. E. Unny, “Application of runge-kutta method for the solution of non-linear partial differential equations”, Applied Mathematical Modelling **1**, 199–204 (1977).

[77]“Steady states and boundary value problems”, in *Finite difference methods for ordinary and partial differential equations* (), pp. 13–58, eprint: `https://epubs.siam.org/doi/pdf/10.1137/1.9780898717839.ch2`.

[78]S. Hamdi, W. E. Schiesser, and G. W. Griffiths, “Method of lines”, Scholarpedia **2**, 2859 (2007).

[79]R. Courant, K. Friedrichs, and H. Lewy, *Über die partiellen differenzengleichungen der mathematischen physik* (Springer Publisher, 1986).

[80]R. Courant, K. O. Friedrichs, and H. Lewy, *On the partial difference equations, of mathematical physics* (IBM, 2015).

[81]A. Melikyan, *Generalized characteristics of first order pdes: applications in optimal control and differential games* (Birkhäuser Boston, 2012).

[82]J. Levandosky, *First-order equations: method of characteristics* (Stanford University, 2002).

[83]J. Andersson, *First order pde: the methods of characteristics* (KTH Royal Institute of Technology, 2015).

[84]Z. Clawson, “Solving (nonlinear) first-order pdes”, PhD thesis (Conrnell University, 2017).

[85]M. W. M. C. Bertens, E. M. T. Vugts, M. J. H. Anthonissen, et al., *Numerical methods for the hyperbolic monge-ampère equation based on the method of characteristics*, 2021, arXiv:`2104.11659 [math.NA]`.

[86]E. Fackerell, “Solutions of zerilli’s equation for even-parity gravitational perturbations”, The Astrophysical Journal **166**, 197 (1971).

[87]C. F. Sopuerta, N. Yunes, and P. Laguna, “Gravitational recoil from binary black hole mergers: the close-limit approximation”, Physical Review D **74**, Publisher: American Physical Society, 124010 (2006).

[88]L. S. Collaboration, K. Collaboration, V. Collaboration, et al., “Population of merging compact binaries inferred using gravitational waves through gwtc-3”, Physical Review X **13**, Publisher: American Physical Society, 011048 (2023).

[89]V. C. Collaboration {and} KAGRA Collaboration LIGO Scientific, R. Abbott, F. Abbott nd Acernese, et al., “GWTC-3: compact binary coalescences observed by LIGO and virgo during the second part of the third observing run”, Physical Review X **13**, Publisher: American Physical Society, 041039 (2023).

[90]S. S. Bavera, T. Fragos, Y. Qin, et al., “The origin of spin in binary black holes”, Astronomy and Astrophysics, `https://doi.org/10.1051/0004-6361/201936204` (2019).

[91]R. J. Gleiser, C. O. Nicasio, R. H. Price, et al., “Evolving the bowen-york initial data for spinning black holes”, Physical Review D **57**, 3401–3407 (1998).

[92]J. M. Bowen and J. W. York, “Time-asymmetric initial data for black holes and black-hole collisions”, Physical Review D **21**, 2047–2056 (1980).

[93]E. Newman and R. Penrose, “An approach to gravitational radiation by a method of spin coefficients”, Journal of Mathematical Physics **3**, 566–578 (1962).

[94]J. L. Ripley, N. Loutrel, E. Giorgi, et al., “Numerical computation of second-order vacuum perturbations of kerr black holes”, Physical Review D **103**, `10.1103/physrevd.103.104018` (2021).

[95]V. Mewes, Y. Zlochower, M. Campanelli, et al., "Numerical relativity in spherical coordinates: a new dynamical spacetime and general relativistic mhd evolution framework for the einstein toolkit", Phys. Rev. D **101**, 104007 (2020).

[96]N. Loutrel, J. L. Ripley, E. Giorgi, et al., "Second-order perturbations of kerr black holes: formalism and reconstruction of the first-order metric", Phys. Rev. D **103**, 104017 (2021).

[97]L. Combi and S. M. Ressler, *A binary black hole metric approximation from inspiral to merger*, 2024, arXiv:`2403.13308 [gr-qc]`.

[98]G. Bozzola and V. Paschalidis, "General relativistic simulations of the quasicircular inspiral and merger of charged black holes: gw150914 and fundamental physics implications", Phys. Rev. Lett. **126**, 041103 (2021).

[99]G. Bozzola and V. Paschalidis, "Numerical-relativity simulations of the quasicircular inspiral and merger of nonspinning, charged black holes: methods and comparison with approximate approaches", Phys. Rev. D **104**, 044004 (2021).

[100]O($\epsilon\cdot$)*Christiansen*, J. B. Jiménez, and D. F. Mota, "Charged black hole mergers: orbit circularisation and chirp mass bias", Classical and Quantum Gravity **38**, 075017 (2021).

[101]F. J. Zerilli, "Perturbation analysis for gravitational and electromagnetic radiation in a reissner-nordström geometry", Phys. Rev. D **9**, 860–868 (1974).

[102]M. Rutkowski, "Nonlinear perturbations of reissner-nordström black holes", Physical Review D **100**, `10.1103/physrevd.100.044017` (2019).

[103]J. Y. J. Burton and T. Osburn, "Reissner-nordström perturbation framework with gravitational wave applications", Physical Review D **102**, `10.1103/physrevd.102.104030` (2020).

[104]G. Bozzola and V. Paschalidis, "Numerical-relativity simulations of the quasicircular inspiral and merger of nonspinning, charged black holes: methods and comparison with approximate approaches", Physical Review D **104**, `10.1103/physrevd.104.044004` (2021).

[105]D. Marìn Pina, M. Orselli, and D. Pica, "Event horizon of a charged black hole binary merger", Phys. Rev. D **106**, 084012 (2022).

[106]V. Cardoso, C. F. B. Macedo, and R. Vicente, "Eccentricity evolution of compact binaries and applications to gravitational-wave physics", Phys. Rev. D **103**, 023015 (2021).

[107]L. Liu and S. P. Kim, "Merger rate of charged black holes from the two-body dynamical capture", Journal of Cosmology and Astroparticle Physics **2022**, 059 (2022).

[108]V. Cardoso, C. F. Macedo, P. Pani, et al., "Black holes and gravitational waves in models of minicharged dark matter", Journal of Cosmology and Astroparticle Physics **2016**, 054 (2016).

[109]S. W. Hawking, "Black holes in general relativity", Communications in Mathematical Physics **25**, 152–166 (1972).

[110]P. Pani, E. Berti, and L. Gualtieri, "Gravitoelectromagnetic perturbations of kerr-newman black holes: stability and isospectrality in the slow-rotation limit", Phys. Rev. Lett. **110**, 241103 (2013).

[111]P. Pani, E. Berti, and L. Gualtieri, "Scalar, electromagnetic, and gravitational perturbations of kerr-newman black holes in the slow-rotation limit", Physical Review D **88**, `10.1103/physrevd.88.064048` (2013).

[112]M. Campanelli and C. O. Lousto, "Second order gauge invariant gravitational perturbations of a kerr black hole", Physical Review D **59**, 124022 (1999).

[113]R. Gleiser, O. Nicasio, R. Price, et al., "Second order perturbations of a Schwarzschild black hole", Classical and Quantum Gravity **13**, arXiv:gr-qc/9510049, L117–L124 (1996).

[114]R. Gleiser, O. Nicasio, R. Price, et al., "Second order perturbations of a schwarzschild black hole", Classical and Quantum Gravity **13**, L117–L124 (1996), arXiv:gr-qc/9510049.

[115]D. Brizuela, J. M. Martín-García, and M. Tiglio, "Complete gauge-invariant formalism for arbitrary second-order perturbations of a schwarzschild black hole", Physical Review D **80**, 10.1103/physrevd.80.024021 (2009).

[116]J. Centrella, J. G. Baker, B. J. Kelly, et al., "Black-hole binaries, gravitational waves, and numerical relativity", Reviews of Modern Physics **82**, 3069–3119 (2010).

[117]D. Pook-Kolb, O. Birnholtz, B. Krishnan, et al., "Existence and stability of marginally trapped surfaces in black-hole spacetimes", Physical Review D **99**, 10.1103/physrevd.99.064005 (2019).

[118]C. Williams, *A black hole with no marginally trapped tube asymptotic to its event horizon*, 2010, arXiv:1005.5401 [gr-qc].

[119]A. M. Abrahams and G. B. Cook, "Collisions of boosted black holes: perturbation theory prediction of gravitational radiation", Physical Review D **50**, R2364–R2367 (1994).

[120]A. Le Tiec and L. Blanchet, "The close-limit approximation for black hole binaries with post-newtonian initial conditions", Classical and Quantum Gravity **27**, 045008 (2010).

[121]J. Baker, M. Campanelli, and C. O. Lousto, "The lazarus project: a pragmatic approach to binary black hole evolutions", Physical Review D **65**, 10.1103/physrevd.65.044001 (2002).

[122]K. R. Eppley, "The numerical evolution of the collision of two black holes", PhD thesis (Princeton University, New Jersey, Jan. 1975).

[123]L. Smarr, A. Čadež, B. Dewitt, et al., "Collision of two black holes: Theoretical framework", **14**, 2443–2452 (1976).

[124]U. Sperhake, B. Kelly, P. Laguna, et al., "Black hole head-on collisions and gravitational waves with fixed mesh-refinement and dynamic singularity excision", Phys. Rev. D **71**, 124042 (2005).

[125]S. Deser, "Arnowitt-Deser-Misner formalism", Scholarpedia **3**, 7533 (2008).

[126]C. Kiefer, *Quantum gravity: third edition*, International Series of Monographs on Physics (OUP Oxford, 2012).

[127]J. M. Lee, *Introduction to smooth manifolds* (Springer Publisher, 2002).

[128]J. M. Lee, *Introduction to riemannian manifolds* (Springer Publisher, 2019).

[129]E. Gourgoulhon, "3 + 1 Formalism and bases of numerical relativity", arXiv: General Relativity and Quantum Cosmology (2007), arXiv:gr-qc/0703035 [gr-qc].

[130]A. Corichi and D. Núñez, *Introduction to the adm formalism*, 2023, arXiv:2210.10103 [gr-qc].

[131]K. Landsman, *Foundations of general relativity: from einstein to black holes* (Radboud University Press, 2021).

[132]Wikisource, *The foundation of the generalised theory of relativity*, [Online; accessed 10-September-2024], 2024.

[133]Y. Choquet-bruhat and R. P. Geroch, "Global aspects of the cauchy problem in general relativity", Communications in Mathematical Physics **14**, 329–335 (1969).

[134]R. A. Konoplya and A. Zhidenko, "Quasinormal modes of black holes: from astrophysics to string theory", Reviews of Modern Physics **83**, 793–836 (2011).